博士論文

Hydrogen quantum diffusion and electronic transport in palladium nanofilms

(パラジウムナノ薄膜における水素の量子拡散と電気伝導特性に関する研究)

小澤 孝拓

Doctoral thesis

Hydrogen quantum diffusion and electronic transport in palladium nanofilms

Takahiro Ozawa

Supervisor
K. Fukutani

Applied physics, the University of Tokyo
Institute of Industrial Science, the University of Tokyo

January 2021

Abstract

Hydrogen, the lightest and smallest element of all atoms, reveals quantum behaviors at low temperature. Quantum tunneling is a typical phenomenon of the nuclear quantum effects, and affected by surroundings of lattice phonons and conduction electrons. On the other hand, hydrogen atoms are readily bonded to various atoms and work as either cation or anion because of its moderate electronegativity. Physical properties of host materials are modulated by hydrogen absorption and adsorption. Furthermore, metastable states and subsurface states potentially have novel electronic and magnetic properties and catalytic reactions. Fundamental understanding of the hydrogen site and interaction with lattice and electrons are essentially important.

This doctoral thesis investigated 1) interaction of hydrogen atoms with palladium (Pd) lattice and electrons in hydrogen quantum diffusion, 2) electronic properties in nm-thick Pd hydrides and 3) structure and dynamics of Pd hydrides.

1) Quantum diffusion of hydrogen in Pd

To detect the hydrogen diffusion, we used electrical resistance measurement. It is a useful way to evaluate the relaxation from metastable to stable states. If the relaxation is caused by hydrogen diffusion, the relaxation time corresponds to the inverse of the hydrogen hopping rate.

Firstly, we focused on the 50 K anomaly, which is a resistance anomaly characteristic of Pd hydrides attributed to ordering of hydrogen atoms in the most stable O sites. We observed the resistance relaxation corresponding to the relaxation from the quenched metastable state and successfully acquired the relaxation time corresponding to the hopping rate of hydrogen between the O sites. The temperature dependence of the hopping rate revealed that hydrogen diffuses by thermal manner above 100 K and by quantum tunneling below 50 K, and at intermediate temperature region between them the hydrogen diffusion is dominated by quantum tunneling from a thermally excited vibrational state in the O site to the metastable T site. This is attributed to the characteristic potential shape of Pd, where the metastable T site exists between the O sites. The effect of energy level matching in quantum tunneling is also discussed.

Secondly, we focused on metastable states of Pd hydrides formed by hydrogen ion implantation. Resistance relaxation corresponding to the hydrogen hopping from T to O sites was observed after the hydrogen implantation. The derived hopping rate obeyed the Arrhenius law at high temperature and was almost independent of temperature with a slight increase with decreasing temperature below 20 K. This increase in the hopping rate at low temperature is due to the non-adiabatic effect of electrons. Particle-electron interaction constant K was derived to be 0.41.

2) Resistance minimum in palladium hydrides

We discovered resistance minimum phenomena at low temperature in Pd films. For a 50-nm-thick film, resistance minimum was observed after the hydrogenation. The temperature and concentra-

tion dependence of the resistance minimum temperature were well approximated by a formula of resistance taking into account the Kondo effect. This result demonstrated the possibility for absorbed hydrogen to induce the Kondo effect in metals. Furthermore, The Anderson localization and the Kondo effect coexisted in ultra-thin films. Thickness dependence indicated that the Kondo effect in PdH_x is enhanced due to the surface effects.

3) Structure and dynamics of Pd hydrides

We developed channeling NRA by combining resonant NRA with $^{1}H(^{15}N, \alpha\gamma)^{12}C$ and ion channeling. This enables us to determine the lattice location of hydrogen in crystals with nm-order depth resolution. We performed the channeling NRA for Pd(100) hydride formed by hydrogen ion implantation at 50 K, and revealed that a part of the implanted hydrogen atoms are located in the T site at 50 K, and they move to the stable O sites after heating up to 80 K.

To investigate the two-dimensional surface effect on vibrational states of hydrogen, we conducted inelastic neutron scattering experiment for 8-nm-thick Pd hydrides. We successfully obtained the vibration spectrum of hydrogen, and revealed that hydrogen is located only in the O site near the two-dimensional surface similarly to that in bulk. However, the shape of the vibration spectrum is similar to that of nanoparticles. The vibrational state of hydrogen near the surface has both characteristics of bulk and nanoparticle.

Contents

Chapter 1

Introduction

There is an increasing demand throughout the world to realize a clean energy society. Hydrogen has come into use as a renewable energy medium in recent years. To realize the clean society with hydrogen, further development of hydrogen production, storage, transport and purification techniques are required. Hydrogen-related materials such as high temperature superconductors have been also studied. Those are all closely related to hydrogen properties such as diffusion, vibration and electronic states. Fundamental comprehension of the properties of hydrogen itself is necessary in pursuit of science and technology.

1.1 Hydrogen diffusion

1.1.1 Thermal diffusion and quantum tunneling

In classical mechanics, the motion of a body with mass m is governed by Newton's Equation of motion and described as

$$m\frac{d^2\boldsymbol{r}}{dt^2} = -\frac{dV}{d\boldsymbol{r}}, \tag{1.1}$$

where t, $\boldsymbol{r}$ and V represent the time, the position of the object and the potential, respectively. The motion is uniquely determined with respect to an initial value according to this formula. It is important that the energy of the body is expressed by a continuous value. Whereas a particle in a potential resides at the position of the minimum potential energy at temperature $T = 0$, the particle undergoes hopping to the neighboring site described by the Arrhenius law, i.e. thermal diffusion, at a finite temperature.

Newton's Equation of motion, however, is no longer valid to describe the motion of light particles such as electrons. In turn, the motion obeys the Schrödinger equation expressed as

$$i\hbar\frac{\partial}{\partial t}\Phi(\boldsymbol{r}, t) = \hat{H}\Phi(\boldsymbol{r}, t), \tag{1.2}$$

where Φ, $\hbar$ and i are a wave function of the particle, the reduced Planck constant and the imaginary unit, respectively. $\hat{H}$ is the Hamiltonian representing the kinetic and potential energies of the system. The particle shows the wave-particle duality and its motion is dealt with quantum mechanically as schematically shown in Figure 1.1. According to the Schrödinger equation, the states with discrete energies are only allowed, and the energy of the ground state is not zero, which is called the

zero-point energy. This represents the zero-point vibration, showing that the motion of the particle is not frozen at even $T = 0$ K. Furthermore, the particle can propagate through a potential barrier even if the barrier has a larger energy than that of the particle. This is a hopping prohibited in the classical mechanics and called the quantum tunneling. These properties in quantum mechanics are called the quantum effects.

The discrete energy levels E_n of the particle in one-dimensional harmonic potential well ($V(x) = \frac{1}{2}kx^2$) are derived as

$$E_n = \left(n + \frac{1}{2}\right)\hbar\omega \tag{1.3}$$

$$\omega = \sqrt{\frac{k}{m}}. \tag{1.4}$$

The zero-point energy ($= \frac{1}{2}\hbar\omega$) and the spacing between the energy levels is inversely dependent on the mass. According to the Wentzel-Kramers-Brillouin (WKB) approximation, the tunneling probability W is given as

$$W = \exp(\frac{-2}{\hbar}\int_{l_1}^{l_2}\sqrt{2m[V(x) - E_n]}dx), \tag{1.5}$$

where $V(x)$ is the potential along the hopping path x, and $x = l_1$ and l_2 are determined by the condition of $V(x) = E_n$ at $x = l_1$ and l_2. This equation shows that the tunneling probability through the barrier strongly depends on the barrier height, the barrier width and also the particle mass. What is important is that these quantum characteristics might be crucial in light particles.

Hydrogen is the lightest and smallest element, and thus it can show the nuclear quantum behaviors explicitly. The hydrogen diffusion and the hydrogen-related reactions are possibly governed by the quantum tunneling.

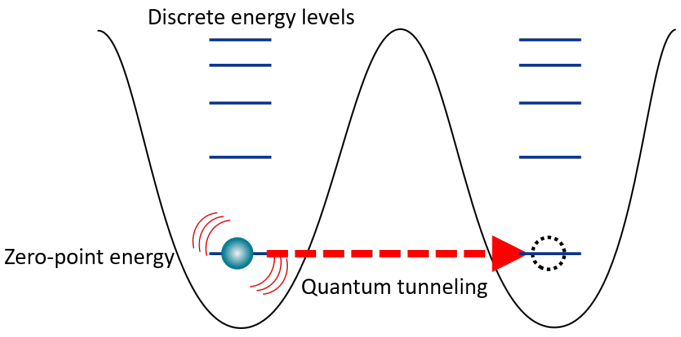

Figure 1.1: Schematic illustration of the quantum effects of the zero-point vibration, the zero-point energy, the discrete energy and the quantum tunneling in a potential well.

1.1.2 Effects of electrons and phonons on quantum tunneling

When a particle diffuses via the quantum tunning at low temperature, the interaction with electrons and phonons of a host material is important. When the particle diffuses by the quantum tunneling in metals and the conduction electrons can not follow its motion, the tunneling probability is affected.

This is called the non-adiabatic effect of electrons and ascribed to the excitation of conduction electrons with infinitesimal energies around the Fermi surface, i.e. the Fermi surface effect [1]. It is theoretically predicted that the non-adiabatic effect enhances the tunneling and makes the tunneling rate slightly depend on temperature as T to a negative power [2, 3], which means that the quantum tunneling gets faster as temperature decreases.

The quantum tunneling is also affected by phonons as temperature increases. The energy dissipation to the phonons possibly assists the quantum tunneling, which is expected to contribute by a T^7-dependence of the tunneling rate of a particle in fcc metals [4]. The tunneling via thermally-excited vibrational states is also important possibly at the crossover region between thermal and quantum regimes, where the potential shape might be crucial. As the temperature becomes higher, the diffusion is governed by a thermal process and depends on temperature exponentially as described by the Arrhenius law. Figure 1.2 illustrates the theoretical prediction of the temperature dependence of the hopping rate of a light particle in metals.

While the thermal diffusion of hydrogen has been studied so far and hopping rates are well known in various metals, experimental and theoretical results of the hydrogen quantum tunneling are still lacking. A general tool to analyze the structure of materials by an electron beam or x-ray can not be used to detect hydrogen atoms due to the small electronic density. Only a few experimental studies reported the quantum tunneling of muon, a light isotope of hydrogen, in metals and hydrogen on metal surfaces [5, 6, 7, 8, 9]. The non-adiabatic effect of electrons and the effects of the phonons on the quantum tunneling are not clarified due to the lack of experimental data. The hydrogen diffusion in materials at low temperature is especially not clear. We successfully observed the quantum diffusion of hydrogen in Pd by electrical resistance measurements and elucidate the effects of electrons and phonons in this thesis.

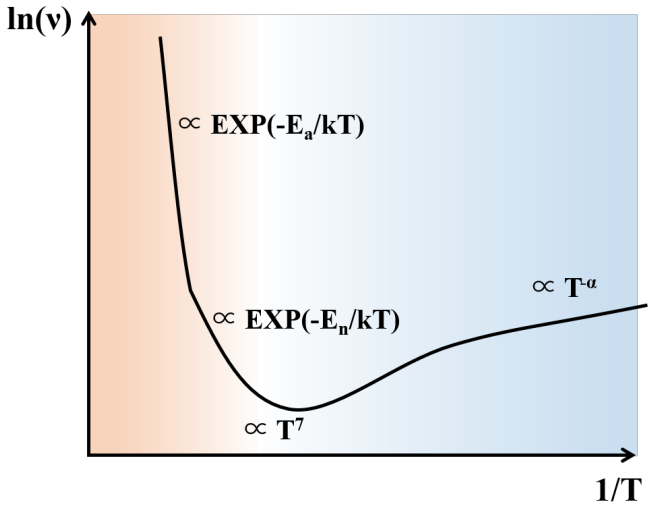

Figure 1.2: Schematic illustration of the temperature dependence of a hopping rate (ν) of a light particle. E_a and E_n represent the activation energy in thermal over-barrier hopping and the vibrational excitation energy, respectively.

1.2 Electronic transport properties modulated by hydrogen

Hydrogen has characteristic electronic properties due to the moderate electronegativity. It can provide or obtain an electron as either cation or anion depending on reaction counterparts and readily bonded to various atoms. This leads to a variety of reactions with different materials. Moreover, it is easy for hydrogen atoms to diffuse into materials thanks to the light mass and the small size. Thus, atomic hydrogen is very reactive.

When hydrogen is adsorbed on and/or absorbed in materials, physical properties of host materials can be modified drastically associated with the electron transfer. Many kinds of changes in electronic and magnetic properties due to hydrogen have been reported such as the surface metalization, the metal-insulator transition, the appearance of superconductivity, the appearance of ferromagnetism and so on [10, 11, 12, 13]. High-temperature superconductors in hydrides under high pressure is also attributed to the hydrogen property of the high phonon frequency due to the light mass. Since these properties are directly and closely related to the hydrogen lattice location, concentration, electronic state and crystal structure, it is extremely important to understand them fundamentally for the control of the physical properties in hydrogen-related materials.

1.3 Surface effects and metastable states

Anomalous states such as surface states and metastable states potentially have novel physical properties and catalytic activities. At a surface, the symmetry breaking gives rise to lattice distortion and unique charge distribution, and new electronic states can be formed, which are called surface states. Surface states have different physical properties from those in bulk [14]. Associated with the surface effects, the absorption energy and the potential shape for hydrogen near the surface can be modified, which results in characteristic hydrogen states about the vibration and the lattice location [15, 16]. Thus, the subsurface region in hydrides might show unusual electronic and magnetic properties reflecting the unique hydrogen states. These hydrogen states near the surface can also contribute to novel reactions on the surface such as hydrogenation catalysts [17]. Furthermore, since subsurface region is inevitable path for hydrogen to be absorbed and desorbed, understanding and controlling the subsurface hydrogen is also important from the viewpoint of the hydrogen storage and transport.

Depending on the way to hydrogenate materials, metastable hydrides can be formed. Non-equilibrium hydrogenation such as hydrogen ion implantation and electrolytic reaction potentially form metastable hydrides with hydrogen atoms in metastable sites and/or super-saturated hydrides [18, 19, 20, 21, 22]. Furthermore, quenching from high temperature possibly freeze a metastable structure [23]. These metastable states also have a possibility of novel physical properties.

1.4 Palladium hydrides

Palladium (Pd) is famous as a hydrogen absorbing metal. Since Pd exothermically absorbs hydrogen and is tolerant toward oxidation, it is used in practical usage as a hydrogen gas purifier and surface coating of Non evaporable getter (NEG) pumping [24]. On the other hand, because Pd is a pure metal which absorbs hydrogen spontaneously, Pd is a good playground to investigate the nature of hydrogen and its interaction with electrons and phonons. Figure 1.3 shows the diffusion coefficients in fcc metals [25]. Experimental data of hydrogen diffusion at low temperature below 100 K are lacking.

Electrical properties of Pd hydrides are also interesting. Phenomena of anomalies in electrical resistance, specific heat and Hall coefficient around 50 K, which is called the 50 K anomaly, were observed as shown in Figure 1.4 [26]. Pd hydrides with high hydrogen concentration show superconductivity with critical temperature below 10 K [12, 27]. Recently, a possibility of high-temperature superconductivity with critical temperature above 50 K was reported in some kind of metastable Pd hydrides formed by quenching after the hydrogenation at high temperature by high pressure H_2 gas dose, though further investigation is needed ro verify the consistency of the report.

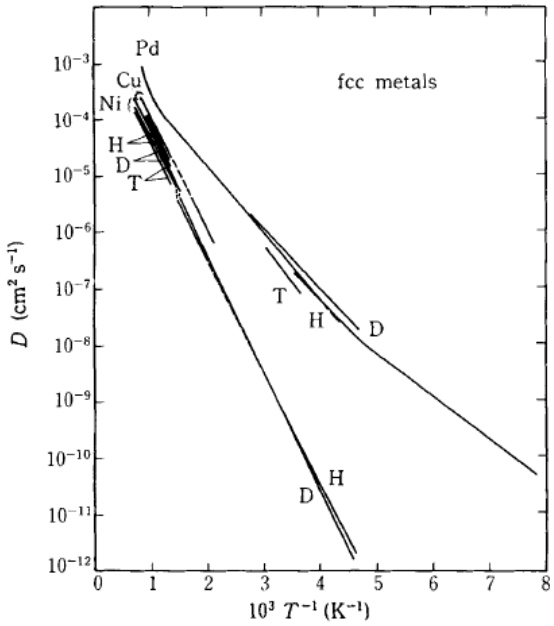

Figure 1.3: Diffusion coefficients of hydrogen in fcc metals [25].

1.5 Purpose of this study

The property of hydrogen is interesting as it possibly shows the quantum nature and modulates the physical properties of materials. The fundamental comprehension of the interaction of hydrogen and metals is important in scientific and technical disciplines. However, the difficulty of the direct observation of hydrogen makes it difficult to elucidate the nature of hydrogen. To overcome the difficulty in the present thesis, we focus on the electrical resistivity, nuclear reaction and neutron scattering to characterize the hydrogen properties. Furthermore, we focus on ultra-thin films to investigate the surface effects on hydrogen states.

This doctoral thesis investigates and clarifies

1. interaction of hydrogen with Pd lattice and electrons in quantum diffusion
2. electronic property and surface effects in nm-thick Pd hydrides
3. lattice location and vibrational states of hydrogen in subsurface region of Pd.

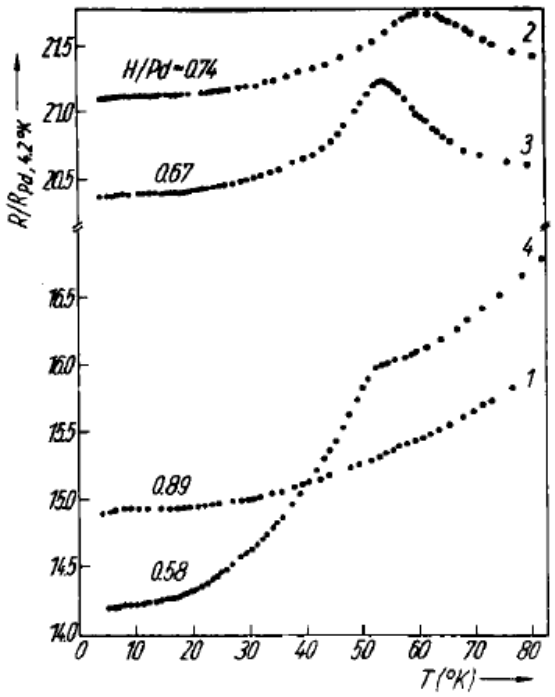

Figure 1.4: Temperature dependence of the resistance of PdH_x [26]. The humps are called the 50 K anomaly.

This thesis consists of 7 chapters. The background and purpose of this thesis are mentioned above in chapter 1. General properties of metal hydrides such as the hydrogen diffusion and the electronic transport are introduced in chapter 2. Experimental principles and apparatus are described in chapter 3. Chapter 4 shows the results of quantum diffusion of hydrogen observed in Pd by electrical resistance measurements. Phenomena of resistance minimum in Pd nanofilms are reported in chapter 5. The structure of metastable Pd hydrides formed by hydrogen ion implantation is analyzed by the channeling NRA, a new method we developed to determine the hydrogen lattice location in crystals, and the hydrogen vibration beneath a two-dimensional surface is investigated by inelastic neutron scattering in chapter 6. Chapter 7 summarizes this thesis.

Chapter 2

Hydrogen and metals

2.1 Metal hydrides

2.1.1 Chemical potential of hydrogen

The chemical potential μ_{id} of an ideal symmetric diatomic molecule with mass m at pressure p is is statistically expressed as

$$\mu_{id} = -k_B T \ln\left[\frac{(4\pi m k_B T)^{\frac{3}{2}}}{h^3}\frac{k_B T}{p} Z_V Z_r\right], \tag{2.1}$$

where k_B, Z_V and Z_r represent the Boltzmann constant, the vibrational partition function and the rotational partition function, respectively. Using the standard pressure p^0 (= 0.1 MPa), the chemical potential for 1 mol of an ideal gas is rewritten as

$$\mu_{id}(T, p) = \mu^0(T) + RT \ln\left(\frac{p}{p^0}\right), \tag{2.2}$$

where $\mu^0(T)$ is the chemical potential at $p = p^0$. In case of a real gas, its chemical potential μ_{re} is expressed by using the fugacity f as

$$\mu_{re}(T, p) = \mu^0(T) + RT \ln\left(\frac{f}{p^0}\right). \tag{2.3}$$

The relationship factor between the fugacity coefficient $\eta(= f/p)$, pressure p and temperature T is derived by the compressibility and given in Figure 2.1. The fugacity increases with increasing pressure, showing that the hydrogen atoms are easy to be absorbed in materials under high pressures.

2.1.2 Formation of metal hydrides

Phase separation

Metal hydrides with nonstoichiometric compositions are formed in various transition metals. In general, the hydrogen atoms absorbed in metals are located in interstitial sites. It is known that two phases with different compositions, different lattice constants and the same structure often coexist

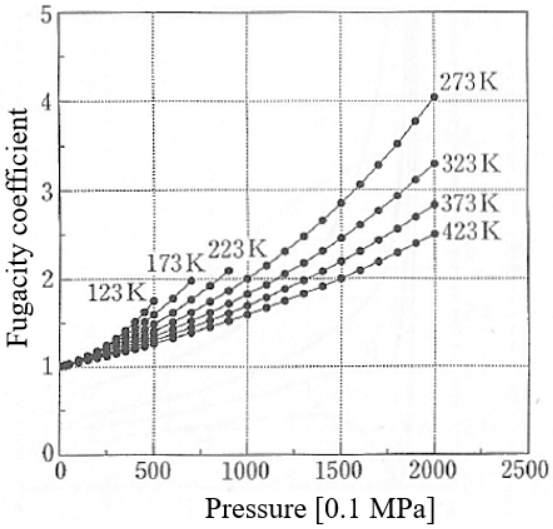

Figure 2.1: Temperature and pressure dependence of the fugacity coefficient η [28].

at low temperature. According to Gibbs' phase rule, which predicts the equilibrium relations of phases, the number of degrees of freedom F of a system is given as

$$F = C - P + 2, \tag{2.4}$$

where C is the number of components and P is the number of phases. Assuming the hydrogen concentration x, the hydrogen gas pressure p and the temperature of a metal T, C is 2 from p and T and P is 3 including the gas phase if the phase separation occurs, which results in $F = 1$. This means that the state of metal hydrides is uniquely determined by any one of x, p and T under the phase separation.

The phase separation is attributed to the term in the chemical potential with $\left(\frac{\partial^2 G}{\partial x^2}\right) < 0$. This term is associated with the elastic interaction related to the hydrogen concentration fluctuation. Figure 2.2 shows the temperature and concentration dependence of the Gibbs free energy, where the elastic interaction term is added as a negative quadratic function with temperature. When the change of the Gibbs free energy ($\Delta G = \Delta H - T\Delta$) is a negative, a reaction goes on spontaneously. When there is a common tangent with point of contact x_α and x_β, the chemical potentials $\left(= \frac{1}{N_0}\frac{\partial G}{\partial x}\right)$ are equal at x_α and x_β. When a metal hydride in a single phase with a concentration x_0 at high temperature is cooled, two phases with concentrations x_α and x_β are formed, where its ratio is $(x_\beta - x_0 : x_0 - x_\alpha)$.

Structure of metal hydrides

When hydrogen is absorbed in metals, the total energy is determined by Coulomb interaction between electrons and nuclei. The s-orbital electron of hydrogen is hybridized with electrons of the host material and the host lattice is distorted. In case of fcc metals, hydrogen atoms tend to be absorbed in an octahedral site (O site) surrounded by the 6 host atoms and/or in a tetrahedral site (T site) surrounded by the 4 host atoms as shown by Figure 2.3. The numbers of sites and the volumes per one unit cell are tabulated in Table 2.1. While the volume is larger for O site, the number of

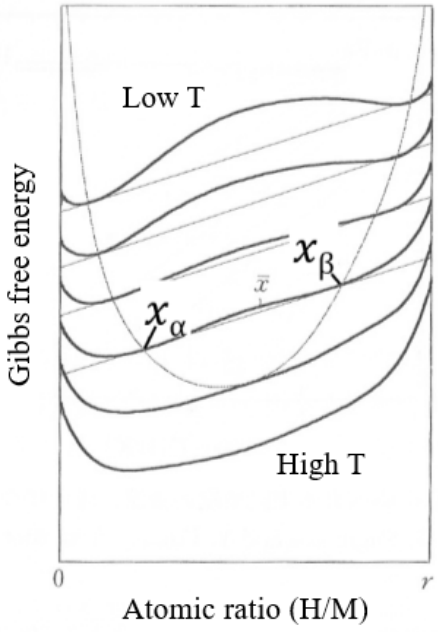

Figure 2.2: Temperature and concentration dependence of the Gibbs free energy [28].

candidates is larger for T site. The potentials at the O and T sites have the cubic symmetry.

Table 2.1: The numbers of sites and the volumes per one unit cell.

	O-site	T-site
The number of sites per a unit cell	4	8
Volume	$\sqrt{2} - 1 = 0.414$	$\frac{\sqrt{6}}{2} - 1 = 0.225$

2.1.3 Hydrogen diffusion in metals

According to the Fick's first law of diffusion, diffusion flux J of particles in a one-dimensional system is described as

$$J = -D\frac{\partial c}{\partial x}, \tag{2.5}$$

where D is called the diffusion coefficient with a unit of m^2s^{-1}. c is the concentration and x is the position. This law relating the diffusion flux to the gradient of the concentration shows that particles go from regions of high concentration to regions of low concentration. D reflects mobility of particles in materials.

Since the amount of inflow and outflow of the particles at a certain region with an area of $L\Delta x$ in Δt is given as $J(x)\Delta tL$ and $J(x + \Delta x)\Delta tL$, respectively, as shown in Figure 2.7, the change of the concentration (Δc) is derived as

$$\Delta c = \frac{J(x)\Delta tL - J(x + \Delta x)\Delta tL}{L\Delta x}. \tag{2.6}$$

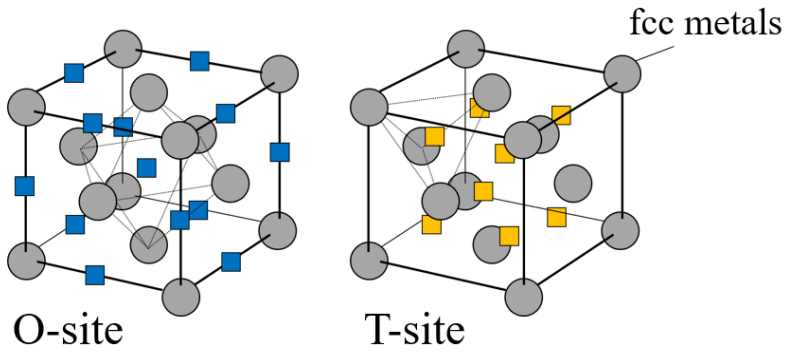

Figure 2.3: Octahedral (O) site and Tetrahedral (T) site in fcc metals.

Thus, the time evolution of the concentration is derived as

$$\frac{\partial c}{\partial t} = -\frac{\partial J}{\partial x} = \frac{\partial}{\partial x}\left(D\frac{\partial c}{\partial x}\right). \tag{2.7}$$

This equation is called the Fick's second law. As long as D is independent of the concentration, the eq. 2.4 is rewritten as

$$\frac{\partial c}{\partial t} = D\frac{\partial^2 c}{\partial x^2}. \tag{2.8}$$

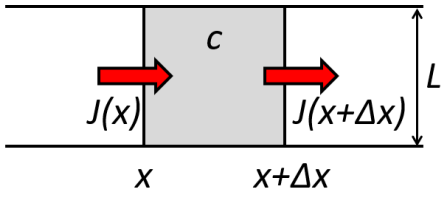

Figure 2.4: Illustration of the flux and concentration in a one-dimensional system.

Assuming that the hopping occurs randomly, as shown in Figure 2.5, the flux J in a small region is written with a hopping rate ν and a hopping distance d as

$$J = \frac{\left(c_1 dL\frac{\nu}{2} - c_2 dL\frac{\nu}{2}\right)}{L} = \frac{(c_1 - c_2)\nu d}{2} \tag{2.9}$$

$$= -\frac{\nu d^2}{2}\frac{\partial c}{\partial x}, \tag{2.10}$$

where the equation of $c_2 = c_1 + \frac{\partial c}{\partial x}d$ is used. Compared with the eq. 2.5, the relation between the diffusion coefficient D and the hopping rate ν in a one-dimensional system is given as

$$D = \frac{d^2}{2}\nu. \tag{2.11}$$

In case of a three-dimensional system, the relation is rewritten as

$$D = \frac{d^2}{6}\nu. \tag{2.12}$$

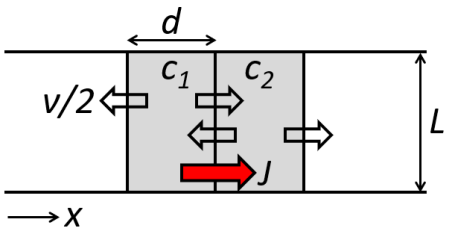

Figure 2.5: Illustration of the flux and random hopping in a one-dimensional system.

Thermal hopping

A thermally activated hopping is schematically shown in Figure 2.6, called the over-barrier hopping (OBH). According to the transition state theory, the reaction rate constant k is given as

$$k = \frac{k_B T}{h}\frac{[T^*]}{[A][B]\cdots}, \tag{2.13}$$

where $A, B\cdots$ and T^* are initial states and a transition state, respectively. [ ] represents the concentration. When $A, B\cdots$ and T^* are in thermal equilibrium, the eq. 2.13 is rewritten as

$$k = \frac{k_B T}{h}\frac{Z_{T^*}}{Z_A Z_B\cdots}, \tag{2.14}$$

where Z represents a partition function ($= \sum_{i=0}^{\infty}\exp(\frac{-E_i}{k_B T})$). In case of diffusion, the hopping rate ν is described as

$$\nu = \frac{k_B T}{h}\frac{Z_T}{Z_A}. \tag{2.15}$$

At high temperature region ($h\nu_i \ll k_B T$), Z_A and Z_T are given as

$$Z_A = \exp(\frac{-E_A}{k_B T})\prod_{i=1}^{3N+3}\frac{k_B T}{h\nu_i} \tag{2.16}$$

$$Z_T = \exp(\frac{-E_T}{k_B T})\prod_{j=2}^{3N+3}\frac{k_B T}{h\nu_j'}. \tag{2.17}$$

Thus, the hopping rate is described as

$$\nu = \frac{k_B T}{h}\frac{Z_T}{Z_A} = \left(\frac{\prod_{i=1}^{3N+3}\nu_i}{\prod_{j=2}^{3N+3}\nu_j'}\right)\exp(-\frac{E_T - E_A}{k_B T}) \tag{2.18}$$

$$= \nu_{OBH}\exp(-\frac{E_a}{k_B T}). \tag{2.19}$$

where E_a is an activation energy. This description corresponds to the Arrhenius law. ν_{OBH} corresponds to the frequency in a reaction coordinate and depends on $\sqrt{\frac{k}{m}}$ in a potential of $\frac{1}{2}kx^2$, where k is a constant. ν_{OBH} is around $10^{12} \sim 10^{13}$ s^{-1}. The diffusion coefficient is expressed as

$$D = D_0 \exp(\frac{-E_a}{k_B T}). \tag{2.20}$$

The temperature-independent term of D_0 is called the diffusion constant.

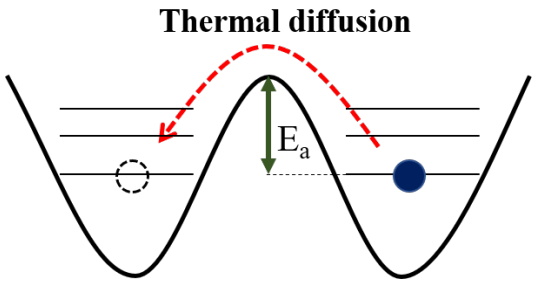

Figure 2.6: Schematic picture of thermal over-barrier hopping (OBH).

Quantum tunneling

As temperature decreases and thermal energy becomes small, the OBH is suppressed. In turn, the quantum tunneling becomes important. The motion of hydrogen is needed to be dealt with quantum-mechanically, where a wave function of proton penetrates into an energy barrier. According to the Wentzel-Kramers-Brillouin (WKB) approximation, the bare tunneling probability W in a one-dimensional system for a particle with mass m and energy E_n is given as

$$W = \exp(\frac{-2}{\hbar} \int_{l_1}^{l_2} \sqrt{2m[V(x) - E_n]}dx), \tag{2.21}$$

where $V(x)$ is the potential along the hopping path x, $\hbar$ is the reduced Planck constant, and $x = l_1$ and l_2 are determined by the condition of $V(x) = E_n$ at $x = l_1$ and l_2. It is meant in tunneling process that the tunneling probability, i.e. the hopping rate, strongly depends on the potential height and length as well as the particle mass. Large kinetic isotope effect in hopping rates is one of the clear evidence for quantum tunneling.

Effect of phonons on tunneling

At temperature around $\sim \Theta_D/5$, where Θ_D is the Debye temperature of a host material, the quantum tunneling via vibrationally excited states of proton (TE) possibly governs the diffusion, as schematically shown in Figure 2.7 [29, 30]. The potential barrier which hydrogen passes through is lower and shorter between excited states in neighboring sites than between ground states. This leads to that the bare tunneling probability W is larger between the excited states. On the other hand, the population in the vibrationally excited states is governed by the Boltzmann factor. The lower the temperature is, the larger the population of lower energy states are, which competes with small tunneling probabilities between lower energy states. Considering multiple excited states, the

total hopping rate of the TE is described by the product of the tunneling and thermal excitation probabilities as

$$\nu = \sum_{n=1}^{N} \nu_n \exp(\frac{-E_n}{k_B T}). \tag{2.22}$$

where E_n (n : the excitation number) is energies of vibrationally excited states and ν_n is a prefactor including the bare tunneling probability. An Arrhenius plot is expected to show upward bends associated with thermal excitation energies to higher vibrational states as temperature increases.

At low temperature around $\sim \Theta_D/5$, the tunneling proceeds from the ground state and the effects of phonons are taken into account as one-phonon, two-phonon processes and so on [31, 32, 33]. In the one-phonon process, proton hopping is forbidden between equivalent sites in ideal lattices such as O sites or T sites in fcc metals unless these sites are energetically disturbed or a proton hops between different type of sites. That originates from the requirement of the energy conservation. If the energy difference ϵ between initial and final sites is enough small compared to $k_B T$, the hopping rate ν approximately depends on temperature as $\nu \propto T$. If ϵ is enough large compared to $k_B T$, there is temperature dependency as $\nu \propto \exp(-\epsilon/k_B T)$ or ν does not depend on T depending on the sign of ϵ. The two-phonon process enables a proton to hop between equivalent sites in an ideal lattice. Whereas the temperature dependence of ν is $\nu \propto T^7$ for jumps between equivalent sites such as O or T sites in fcc metals, ν becomes $\nu \propto T^3$ in bcc metals [4]. The energy coincidence event of a particle by lattice vibrations between distorted sites or inequivalent sites also affects the hopping rate [34, 33, 34, 35], as schematically shown in Figure 2.8. The tunneling probability is increased in the coincidence situation, and the hopping rate is expressed in the form of thermal activation hopping. The derived activation energy corresponds to the energy necessary to cause the energy coincidence. These tunneling affected by phonons is called the phonon-assisted tunneling. The phonon-assisted tunneling in an asymmetric energy system is discussed by Regelman [36].

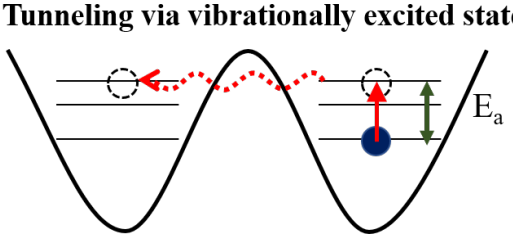

Figure 2.7: Schematic picture of quantum tunneling via vibrationally excited states (TE).

Non-adiabatic effect of electrons on tunneling

We have dealt with hydrogen diffusion as a single particle motion so far. Here, we think of Schrödinger equation for a system with atomic nucleus as well as electrons. The Hamiltonian $\hat{H}$ is given by

$$\hat{H}(r,R) = \hat{T}_{\mathrm{n}}(R) + \hat{T}_{\mathrm{e}}(r) + V(r,R) \tag{2.23}$$

$$= \sum_{i=1}^{L} \frac{\hat{P}_i^{\,2}}{2M} + \sum_{k=1}^{N} \frac{\hat{p}_k^{\,2}}{2m} + V(r,R), \tag{2.24}$$

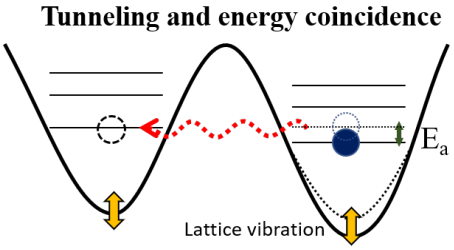

Figure 2.8: Schematic picture of quantum tunneling and the energy coincidence.

where $\hat{T}_{\rm n}(R)$ and $\hat{T}_{\rm e}(r)$ are kinetic energies of nuclei and electrons, R and r indicate position vectors for the total nuclei and electrons, and m and M are mass of electron and nucleus, respectively. L and N are the number of nuclei and electrons, respectively. $V(r,R)$ is a total potential energy for them. The Schrödinger equation is given by using wave function Ψ of the system and energy eigenvalue E as

$$\hat{H}(r,R)\Psi(r,R) = E\Psi(r,R). \tag{2.25}$$

This equation consisting of particles more than two, however, can not be solved exactly and is needed to be solved approximately. Assuming the position of the nucleus is frozen at $R = R_0$, the Schrödinger equation is solved, and electron wave function $\Psi_{\rm e}(r;R_0)$ is derived for a nucleus position vector of R_0. The set of wave functions $\Psi_{en}(r;R)$ forms an orthonormal basis, and the total wave function Ψ can be expressed as

$$\Psi(r,R) = \sum_{n=1}^{\infty} \phi_n(R)\Psi_{en}(r;R). \tag{2.26}$$

Integrating the Schrödinger equation about electrons with r, a diagonal component of matrix is obtained, what is called the adiabatic correction factor, as

$$\frac{1}{2M}\sum_{i=1}^{L}\int \Psi_{em}^{*}\hat{P}_i^{\,2}\Psi_{em}dr. \tag{2.27}$$

Non-diagonal components are given as

$$\frac{1}{2M}\sum_{i=1}^{L}\sum_{n\neq m}^{\infty}\left(\int \Psi_{em}^{*}\hat{P}_i^{\,2}\Psi_{en}dr + 2\int \Psi_{em}^{*}\hat{P}_i\Psi_{en}dr\right). \tag{2.28}$$

In the adiabatic approximation the non-diagonal components are ignored, and the Born-Oppenheimer approximation ignores both diagonal and non-diagonal components. They represent non-adiabatic effects, which are inversely proportional to the nuclear mass M. Qualitatively speaking, electrons can not follow and screen the motion of nucleus perfectly. Hence, the non-adiabatic effects appear more prominently for light nucleus.

At sufficiently low temperature below $\sim \Theta_D/5$, non-adiabatic effects of electrons have to be taken into account, which contributes to the temperature dependence of the hopping rate [2, 37, 1]. The contribution from the phonons to hopping rate is regarded to be constant and does not affect

the temperature dependence of the hopping rate. It is assumed that a proton is moving rapidly in a well in a periodic potential but the electron wave function is fixed at the center of the well instead of following the proton motion [38, 2]. A total wave function Ψ is described as

$$\Psi = \sum_{n=1}^{\infty} \mathrm{e}^{iq\cdot R_n} \phi(R - R_n)\Psi(r; R_n), \tag{2.29}$$

where R_n is a central coordinate of the well. $\Psi(r; R_n)$ means the electron wave function centered at R_n. It is concluded that a matrix element of proton tunneling from R_1 to R_2 is renormalized by the overlap integral of $< \Psi_{R_1} \mid \Psi_{R_2} >$ as

$$< \phi(R - R_1) \mid \hat{H} \mid \phi(R - R_2) > \cdot < \Psi_{R_1} \mid \Psi_{R_2} > . \tag{2.30}$$

The first term is a bare tunneling matrix element when ignoring electrons.

Here, we think about the the overlap integral of the electron wave function $< \Psi_{R_1} \mid \Psi_{R_2} >$. According to Anderson's orthogonality catastrophe [39], when perturbation potential is introduced into a metal with conduction electrons, wave functions in the ground state of a free electron gas before and after the introduction of the perturbation are orthogonal each other. The overlap of the electrons with and without the perturbation potential decays in the thermodynamic limit. This theory gives rise to an extremely serious issue on proton tunneling. If there is a proton in an interstitial site in a metal, it makes a perturbation potential for conduction electrons. When the proton hops to a neighboring site via quantum tunneling, perturbation potential for electrons changes and the overlap $< \Psi_{R_1} \mid \Psi_{R_2} >$ of the ground state of electrons vanishes, resulting in impossibility of proton tunneling. Actually, however, the motion of electrons is not fast enough to follow the motion of proton. Adiabatic theorem is no longer valid, and a lot of excitation to form electron-hole pairs with an infinitely small energy are allowed around the Fermi surface. The overlap $< \Psi_{R_1} \mid \Psi_{R_2} >$ is given as

$$< \Psi_{R_1} \mid \Psi_{R_2} >= \left(\frac{\omega_c}{E_f}\right)^K \simeq \left(\frac{k_B T}{E_f}\right)^K , \tag{2.31}$$

where E_f is a Fermi energy, ω_c is a cut-off energy, which is assumed to be determined by thermal excitation and ω_c is replaced by $k_B T$. Coupling constant K is given as

$$K = 2(\rho V)^2[1 - j_0^2(k_F|R_1 - R_2|)]. \tag{2.32}$$

ρ is an electron density around E_f in the conduction band, and V is a perturbation. j_0 is the spherical Bessel function of zero order expressed as $\frac{\sin x}{x}$. Consequently, the hopping rate of proton is derived as

$$\nu \propto \left(\frac{\pi T}{E_f}\right)^{2K} \cdot \frac{1}{\pi K T} \propto T^{2K-1}. \tag{2.33}$$

The first term corresponds to the overlap integral $< \Psi_{R_1} \mid \Psi_{R_2} >$ of the electron wave functions, and the second term represents energy dissipation associated with energy level mismatching between at R_1 and R_2. This is the transition rate by the renormalized tunneling matrix element by the electron overlapping to a final state with density of state reduced by $(\pi K T)^{-1}$. Yamada proved that the value of K is smaller than 0.5 for the particle with one positive charge [3]. Therefore, tunneling rate of

proton or muon is expected to depend on temperature as T to a negative power. This contribution is called the non-adiabatic effect of conduction electrons, which is attributed to the infinitesimal energies around the Fermi surface of conduction electrons, i.e. the Fermi surface effect [1].

Previous experimental studies

Figures 2.9 and 2.10 show the temperature dependence of the diffusion coefficients D observed for hydrogen in fcc and bcc metals. It is known that the hydrogen hopping rate obeys the Arrhenius law at high temperature. In general, D is larger in bcc metals than in fcc metals since the distance of hydrogen hopping is shorter in bcc metals.

The quantum nature of hydrogen diffusion has been investigated so far. It was revealed that muon, a light isotope of H, diffuses by quantum tunneling in Cu [40, 41, 42] and Al [43, 44]. Figure 2.11 shows the hopping rate of muon in Cu observed by μSR. The increase in the hopping rate with decreasing temperature indicates the non-adiabatic effect of electrons. From the temperature dependence, the coupling constant K in Eq. 2.33 is derived to be 0.22 for Cu and 0.32 in Al [5]. The quantum diffusion of hydrogen was also demonstrated on some metal surfaces [6, 7, 8, 9]. Figures 2.13 and 2.12 show the temperature dependence of the hopping rate of hydrogen on Cu and W, respectively. The increase in the hopping rate at low temperature in Figure 2.13 shows the non-adiabatic effect of electrons and the K is derived to be 0.25. However, experimental data is still lacking to elucidate the non-adiabatic effect of electrons, the effect of phonons, the isotope effect, the concentration dependence and the hopping mechanism at the crossover temperature between thermal and quantum regimes. In particular, diffusion of hydrogen at low temperature in metals has not been clarified due to the difficulty of direct observation of hydrogen atoms in a material [45].

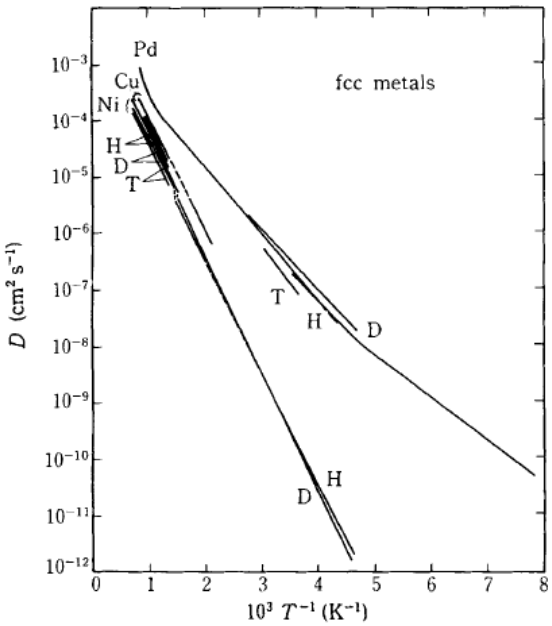

Figure 2.9: Diffusion coefficients of hydrogen isotopes in fcc metals [25].

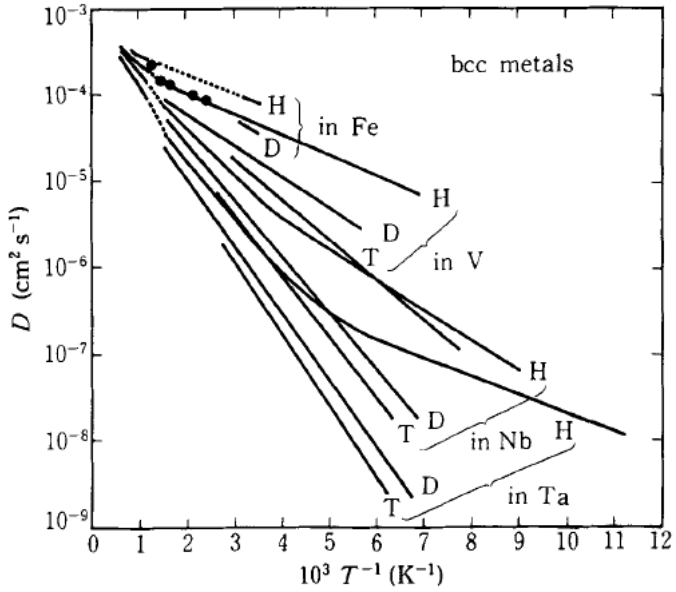

Figure 2.10: Diffusion coefficients of hydrogen isotopes in bcc metals [25].

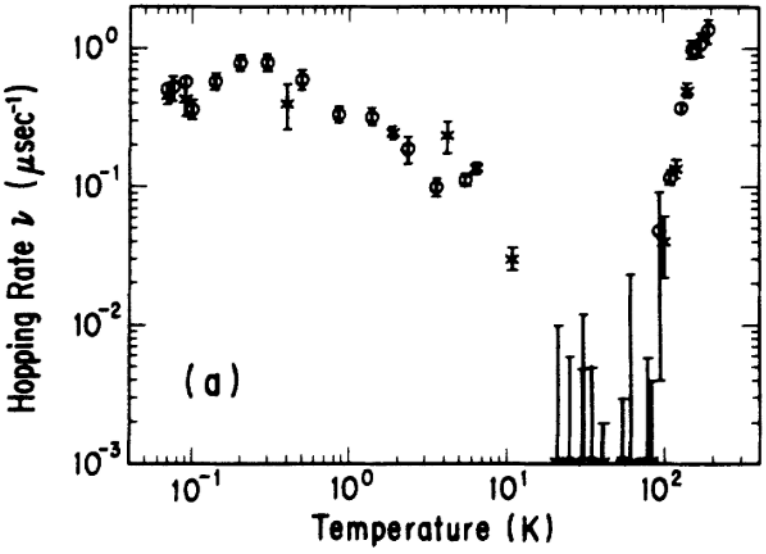

Figure 2.11: Temperature dependence of muon diffusion in Cu [40].

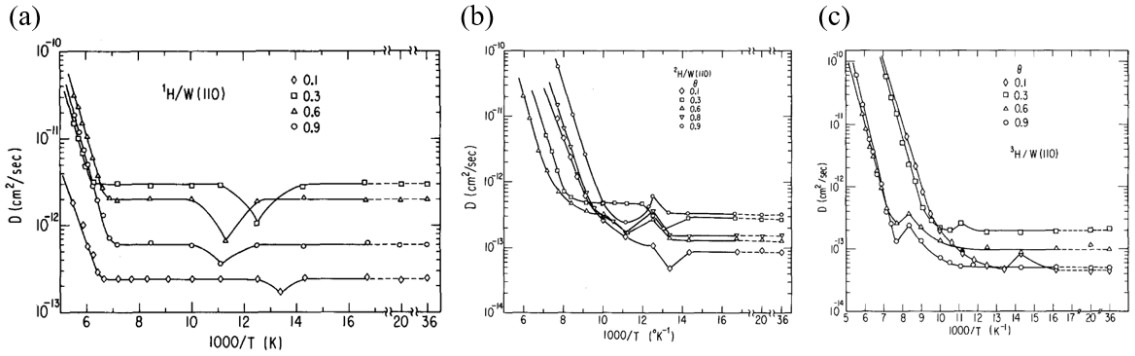

Figure 2.12: Temperature dependence of (a)hydrogen (b) deuterium and (c) tritium diffusion coefficients on W [6].

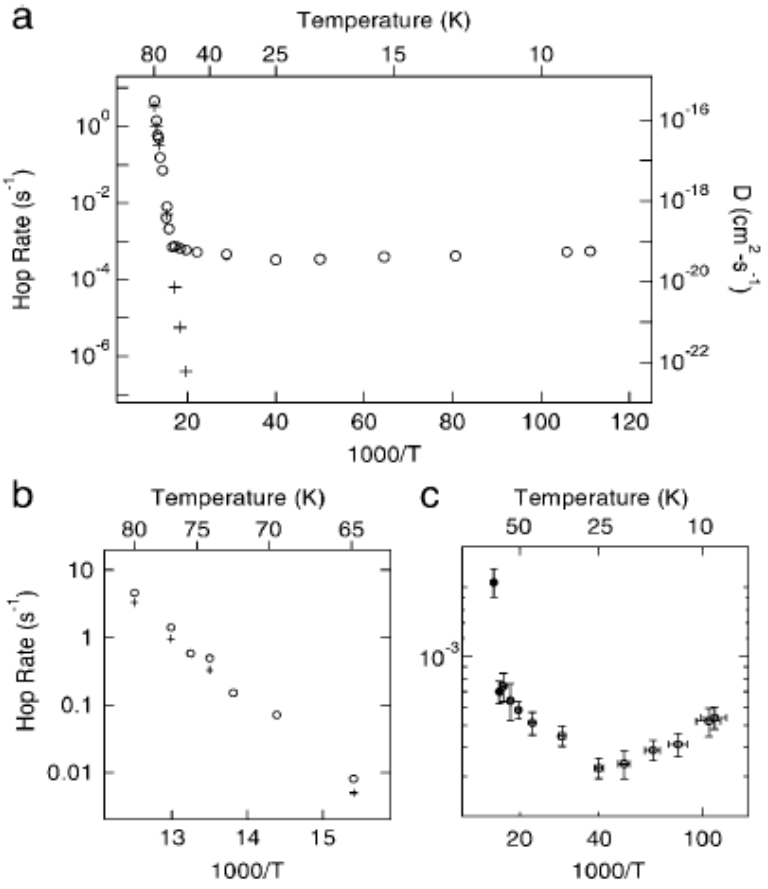

Figure 2.13: Temperature dependence of hydrogen hopping rate on Cu [8].

2.2 Electronic transport in metals

2.2.1 Temperature dependence

The electrical conductivity (σ) is expressed as

$$\sigma = en\mu, \tag{2.34}$$

where e, n and μ represent the charge of electrons, the density of conduction electrons and the electron mobility, respectively. The μ is given as

$$\mu = \frac{e}{m}\tau, \tag{2.35}$$

where m and τ represent the effective mass of electrons and the relaxation time of electron scattering, respectively, which shows that the conductivity of metals is large in the system having the large density of states around the Fermi level and/or in the system where the mobility is large due the good quality of crystal without impurity and defects. Conduction electrons in metals are scattered by various mechanisms such as lattice phonons, electrons, defects, impurities and so on, which is reflected in the temperature dependence in the the relaxation time (τ). According to Matthiessen's rule, the temperature dependence of the total resistivity $\rho(T)$ ($=\frac{1}{\tau}$) is empirically described as

$$\rho(T) = \rho_0 + \rho_{ph}(T) + \rho_{el}(T). \tag{2.36}$$

The first term represents the electron scattering by impurities and defects such as dislocations, lattice vacancies and grain boundaries, which is called the residual resistivity and independent of temperature. The second and the third terms are caused by electron scattering by phonons and electrons, respectively.

The temperature dependence of the resistivity by electron scattering with phonons $\rho_{ph}(T)$ is explained by the lattice vibration. An average kinetic energy of the lattice vibration E_K of an atom with mass m is expressed with the vibration amplitude A and the frequency ω as

$$E_K = \frac{1}{2}mA^2\omega^2. \tag{2.37}$$

Since the kinetic energy for the lattice vibration of the total atoms are approximated as $\sim k_B T$, the temperature dependence of the vibration amplitude A is expressed as follows:

$$A \propto T^{\frac{1}{2}}. \tag{2.38}$$

The temperature dependence of the scattering cross section S by the lattice atom is given as

$$S = \pi A^2 \propto T. \tag{2.39}$$

Accordingly, the temperature dependence of electron mobility is expressed as

$$\mu = \frac{e}{m}\tau \propto \frac{1}{S} \propto T^{-1}. \tag{2.40}$$

As a result, the temperate dependence of resistivity $\rho_{ph}(T)$ of the scattering by phonons is obtained

as

$$\rho_{ph} \propto \frac{1}{\mu} \propto T. \tag{2.41}$$

This equation represents that the resistivity linearly depends on temperature.

At low temperature sufficiently below the Debye temperature θ_D, however, Eq. 2.41 is not valid. The number of scattering events (ν) to make the velocity of electrons saturated get larger and depends on temperature as T^{-2} because the probability of forward scattering events is increased and the efficiency for a scattering event to decelerate the electrons is smaller at low temperature. On the other hand, the density of phonons n_{phonon} depend on temperature as T^3, reflecting the T^3 dependence of th lattice specific heat. Therefore, the electrical conductivity is expressed as

$$\sigma \propto v\tau \propto \frac{v}{n_{phonon}} \propto \frac{T^{-2}}{T^3} = T^{-5}, \tag{2.42}$$

and the temperature dependence of $\rho_{ph}(T)$ is obtained as

$$\rho_p \propto T^5. \tag{2.43}$$

On the other hand, at low temperature, the contribution on the electrical resistivity by electron scattering with electrons might be also crucial. It is theoretically proved that the resistivity depends on the temperature as $\rho_{el}(T) \propto T^2$ due to the interband electron-electron scattering, or mutual scattering of conduction electrons [46, 47]. In general, this contribution is possibly non-negligible in transition metals which have d electrons with large effective mass, though it is negligible in normal metals.

Therefore, the temperature dependence of the resistivity in normal metals is expressed as

$$\rho(T) \propto \begin{cases} \rho_0 + aT & (\theta_D < T) \\ \rho_0 + bT^5 & (T \ll \theta_D), \end{cases} \tag{2.44}$$

where a and b are constants independent of temperature. In case of transition metals, that is described as

$$\rho(T) \propto \begin{cases} \rho_0 + aT & (\theta_D < T) \\ \rho_0 + bT^5 + cT^2 & (T \ll \theta_D), \end{cases} \tag{2.45}$$

where c is a constant.

2.2.2 Kondo effect

Resistance minimum phenomena are famous behaviors observed in metals such as Au, Ag, Cu with dilute magnetic impurities such as Cr, Mn and Fe [48, 49]. Kondo revealed that the origin of the resistance minimum was explained by the interaction between the localized spin of a magnetic impurity and conduction electrons [50]. This many-body scattering processes are called the Kondo effect, where the third-order perturbation theory is applied to deal with the s-d electron scattering. The Kondo effect give rise to a term in the electrical resistivity which increases logarithmically with decreasing temperature. Including the Kondo effect, the temperature dependence of normal metals of eq. 2.44 is rewritten as

$$\rho(T) = \rho_0 + bT^5 - Cd \ln T, \tag{2.46}$$

C and d are a concentration of magnetic impurities and a constant, respectively. One recognizes that the temperature dependence of the resistivity depends on the concentration. By solving the equation of $\frac{d\rho(T)}{dT} = 0$, the temperature (T_{min}) at which the resistivity is the smallest is described as

$$T_{min} = \left(\frac{Cd}{5a}\right)^{\frac{1}{5}} \propto C^{\frac{1}{5}}. \tag{2.47}$$

In case of transition metals with magnetic impurities, the temperature-dependent resistivity is expressed as

$$\rho(T) = \rho_0 + bT^5 + cT^2 - Cd \ln T. \tag{2.48}$$

Figure 2.14 shows the resistance of Cu with the impurities of Fe. The logarithmic increase in resistance below ~40 K represents the Kondo effect.

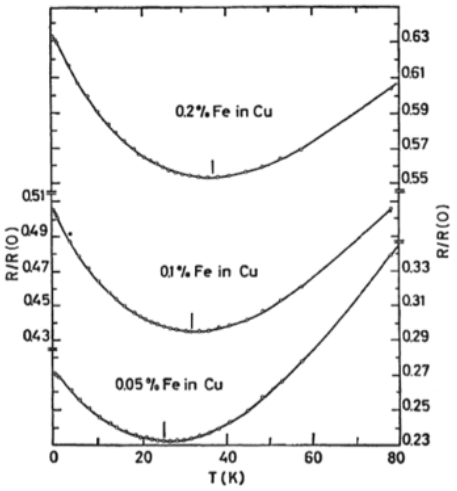

Figure 2.14: Temperature dependence of resistance of Cu with Fe [51].

2.2.3 Anderson localization

A resistance minimum phenomenon is also observed in ultra thin films and nanoparticles, which is called the Anderson localization [52, 53]. This phenomenon is attributed to the electron localization in a lattice potential whose degree of randomness is sufficiently large such as in metals and semiconductors with impurities and defects. According to the Scaling theory [54], the electrical conductivity σ in a one or two-dimensional system with a disordered potential depends on temperature as

$$\sigma(T) = a + b \ln T \propto \ln T, \tag{2.49}$$

where a_2 and b_2 are constants. Thus, the temperature-dependent logarithmic term as -ln T contributes to the resistivity. Figure 2.15 shows the resistance of two-dimensionally coupled Cu particles with a diameter of 30 Å, which increases logarithmically as decreasing temperature below ~10 K. In case of a three-dimensional system with a disordered potential, the electrical conductivity is

given by

$$\sigma(T) = a + bT^{\frac{p}{2}} \propto T^{\frac{p}{2}}, \tag{2.50}$$

where p is a constant (≤ 2).

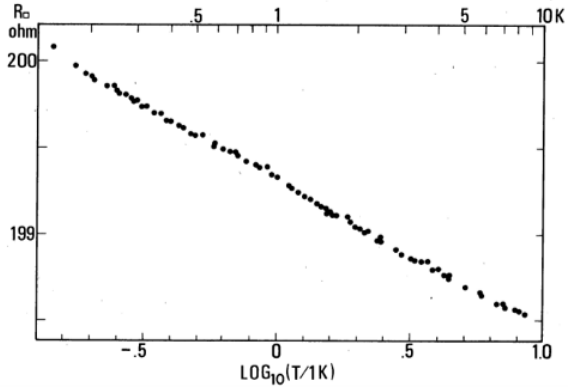

Figure 2.15: Temperature dependence of resistance of the two-dimensionally coupled Cu particles with a diameter of 30 Å [55].

2.2.4 Electronic properties of metal hydrides

Reflecting the changes of the density of states around the Fermi level and the electron mobility, electronic properties differently change in metals by the hydrogen absorption. The resistance is increased or decreased by hydrogen absorption depending on materials. The relation between hydrogen and superconductivity is interesting. Appearance of superconductivity by hydrogenation was observed [56]. Theoretically, Ashcroft predicted that hydrides with high concentration or metallic hydrogen possibly show high-temperature superconductivity owing to the high phonon frequency associated with the light mass of hydrogen [57, 58]. The high-temperature superconductivity with a citical temperature above 200 K was eventually discovered for H_3S in 2014 [59, 60], and the room-temperature superconductivity with a critical temperature of 287.7 K was reported in a carbonaceous sulfur hydride in 2020 [61].

The resistance minimum phenomenon and the logarithmic contribution as -ln T in resistance were also reported in some hydrides [62, 63, 64]. Figures 2.16 and 2.17 show the temperature dependence of the resistances for $YH_{3-\delta}$ and $NbH_{0.9}$. Theoretically, the Kondo-lattice-like effects by hydrogen atoms in transition metals, which originates from the strong dependence of the H 1s orbital radius on the occupation number was proposed [65]. Though the contributions of the Kondo effect and the Anderson localization are suggested as well as the Kondo-lattice, the origins are still not clear.

2.3 Palladium hydrides

2.3.1 Palladium

Palladium is a transition metal with symbol Pd and atomic number 46, whose structure is fcc with a lattice constant of $a = 3.8898$Å. The (111) plane is energetically the most stable. Pd absorbs H

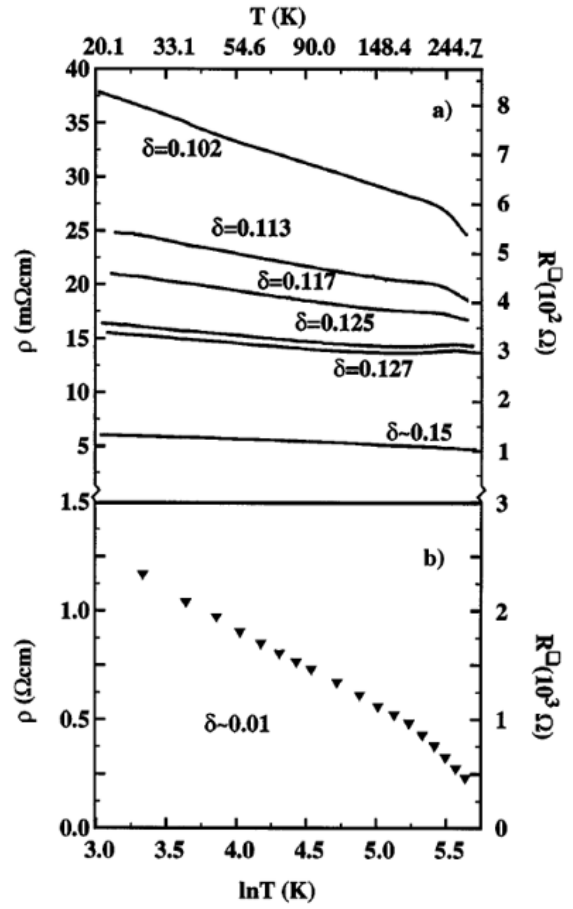

Figure 2.16: Temperature dependence of resistivity of $YH_{3-\delta}$ [62].

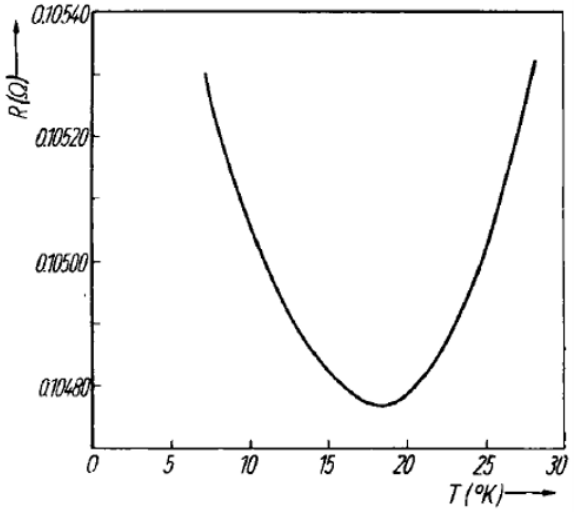

Figure 2.17: Temperature dependence of resistance of $NbH_{0.9}$ [63].

atoms exothermically, as the enthalpy of solution ΔH is -10 kJ/mol-H. It has been used in various industrial fields of hydrogen storage, purifier, catalyst and so on. Pd is also a good model to understand the interaction between metals and hydrogen atoms in scientific significance.

Figure 2.18 shows the electronic density of states by the x-ray photoelectron spectroscopy and the DFT calculation. The Fermi level is located around the sharp edge of the large density of states of 4d-electrons, and the electronic property is probably sensitive to the change in the electronic structure. Ferromagnetism was observed in the nanoparticles and nanofilms with (100) plane, which is considered to be consequence of the change in the electronic structure by the localization of electrons due to the size effect [66, 14] though Pd in bulk is paramagnetism with relatively great magnetism.

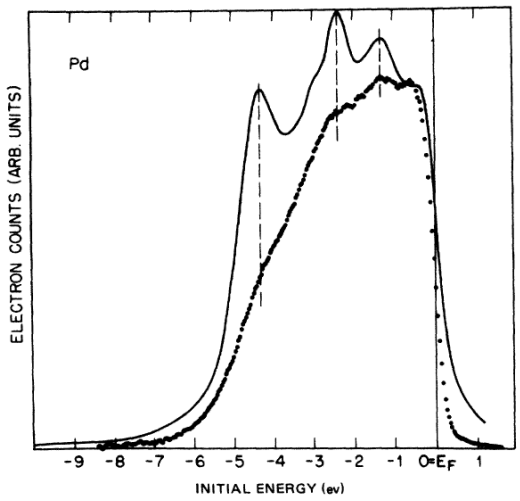

Figure 2.18: Density of states of Pd measured by XPS (black plot) and calculated by DFT calculation. [67]

2.3.2 Hydrogen absorption mchanism

Hydrogen molecules are dissociatively adsorbed on Pd surfaces, and the hydrogen atoms diffuse into the bulk through the subsurface region and absorbed in Pd. The Pd and hydrogen system has been widely studied so far. Figure 2.19 shows the results of thermal desorption spectroscopy (TDS) of mass 2 for the specimen of a Pd(100) single crystal after the hydrogen gas exposure at various low temperatures. The desorption peak around 350 K corresponds to the desorption of the adsorbed hydrogen atoms. The increase in the desorption area with increasing exposure amount shows the hydrogen absorption in the subsurface and the bulk, which are desorbed at lower temperature than the desorption of the adsorbed hydrogen atoms.

2.3.3 Structure of palladium hydrides

Figure 2.20 shows the pressure-composition-temperature (PCT) curve of Pd hydrides in bulk. PdH_x has two phases denoted as α and β with small and large $x's$ below ~600 K. α and β phases correspond to solid-solution and hydride phases, respectively. α and β phases coexist for the PdH_x

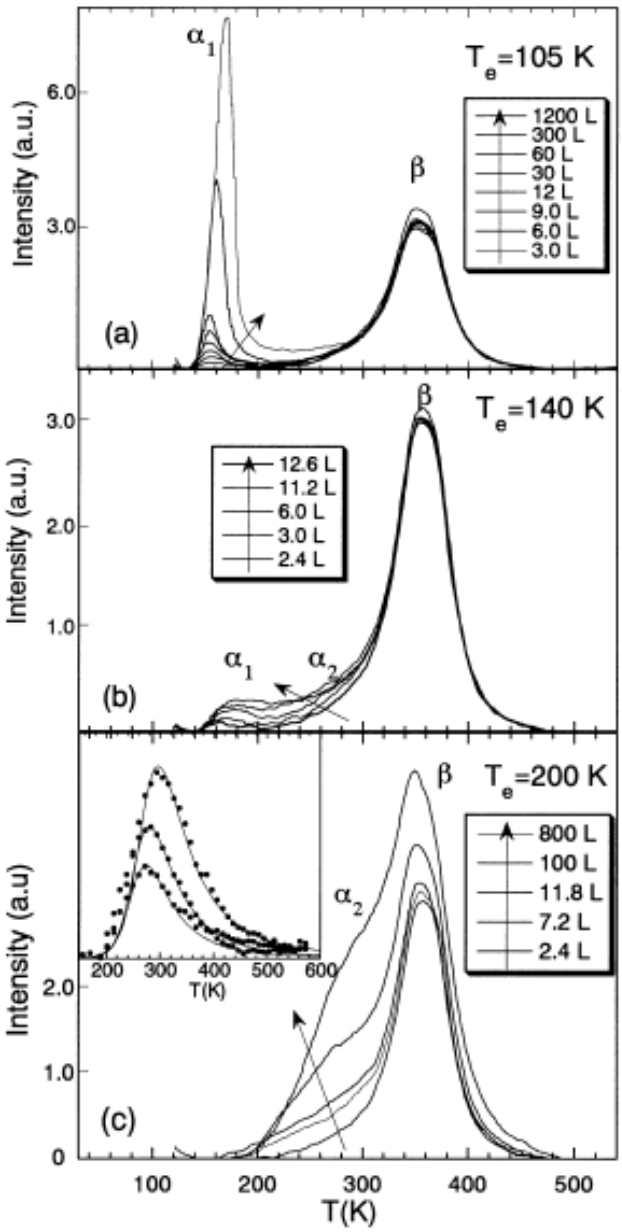

Figure 2.19: Results of thermal desorption spectroscopy for a Pd(100) single crystal after the hydrogen gas exposure at various low temperatures [68].

with x between $x's$ of α and β phases, which corresponds to the plateau region. The maximum composition ratio x for stable Pd hydrides is 1.

The candidates of hydrogen absorption sites in Pd with fcc structure are O and T sites. It is experimentally revealed by neutron scattering that the hydrogen is stably located in the O sites [69, 70]. Figure 2.21 shows the free energy profiles for hydrogen calculated by ab initio path-integral molecular dynamics in the DFT framework. It is theoretically shown that the O site is the most stable and the T site is metastable, which is consistent with the experimental studies. These results indicate that all of the O sites are occupied by hydrogen atoms in PdH_x with the maximum composition $x = 1$.

It is experimentally and theoretically revealed that the stability of hydrogen near the surface in Pd nanoparticle is modulated and hydrogen atoms partially occupy T sites beneath the surface as well as O sites in nanoparticle [15, 16]. Figure 2.22 shows the size dependence of the hyrogen PCT curve of PdH_x nanoparticle. The $(\alpha + \beta)$-phase region is narrowed as the size of the nanoparticle is reduced due to the size effects. While the size and/or surface effects on hydrogen absorption properties in nanoparticle were evaluated, size and/or surface effects near two-dimensional flat surface has not been investigated.

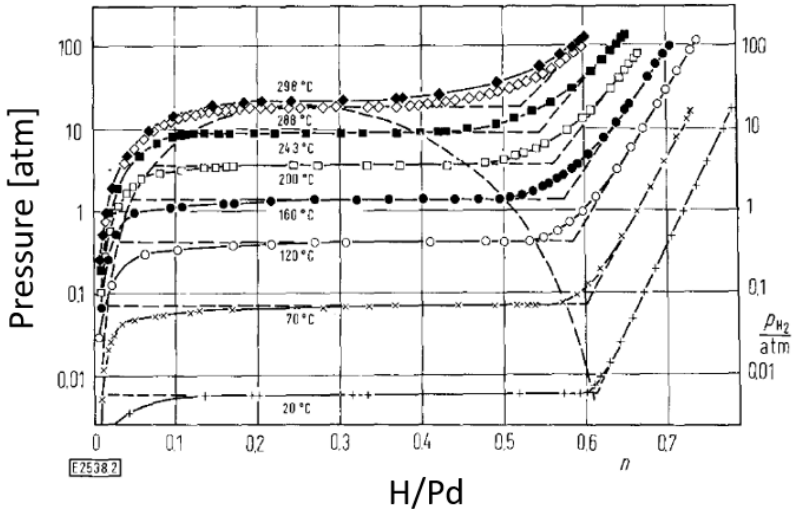

Figure 2.20: Hydrogen PCT curve for Pd bulk [71].

2.3.4 Hydrogen diffusion

Hydrogen and deuterium were observed to diffuse via a thermal manner above 200 K with activation barriers of 0.23 and 0.206 eV, respectively, as shown in Figure 2.9 [74, 75]. Compared with theoretical calculations of the potential of H in Pd [76, 77], the thermal diffusion is considered to take place along the minimum energy path between neighboring O sites via the metastable T site (O-T-O) through the saddle point (SP) instead of taking the direct shortest path between the O sites (O-O). As can been seen in Figure 2.9, the inverse isotope effect between hydrogen and deuterium on thermal diffusion was observed, which is attributed to the activation energy reflecting the quantum effect of the zero-point energies at the O site and the SP. The inverse isotope effect shows the zero-point energy is larger at the SP and so the potential curvature is larger in the SP than

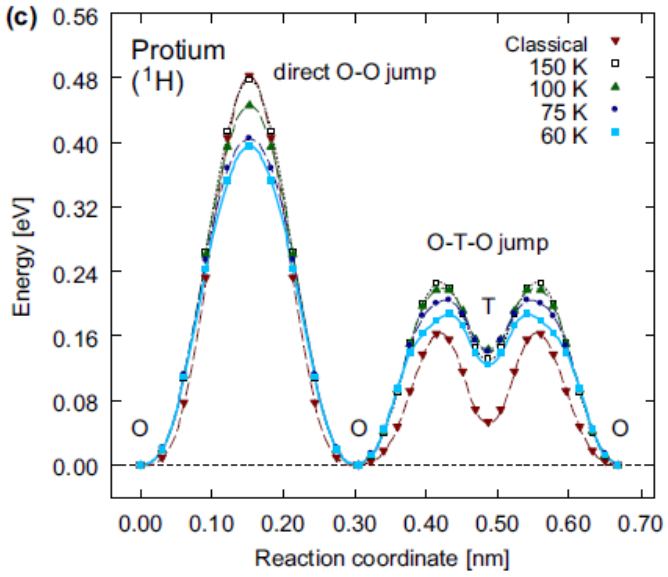

Figure 2.21: Free energy profiles for hydrogen calculated by ab initio path-integral molecular dynamics in the DFT framework [72].

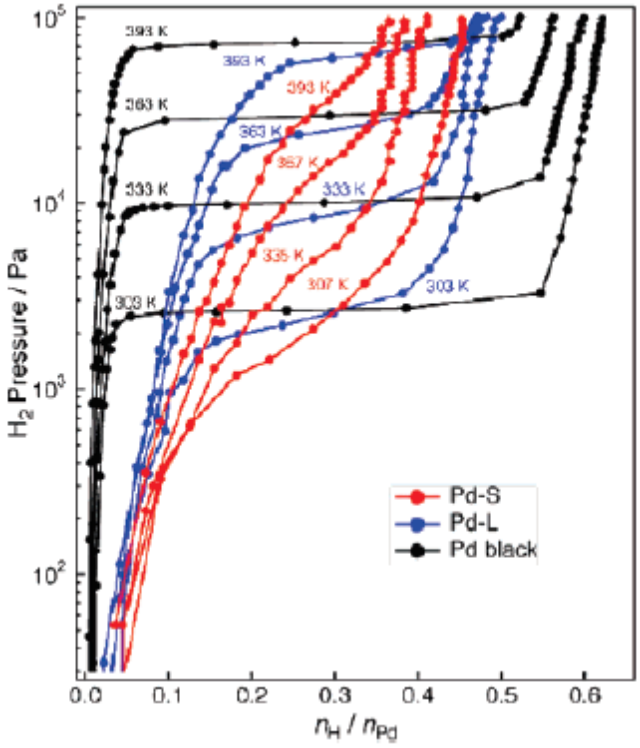

Figure 2.22: Hydrogen PCT curve for Pd nanoparticle. Red and blue and black plots represent to nanoparticles with diameters of 2.6 and 7.0 nm, respectively. Black plots represent Pd black [73].

in the O site. At low temperature, quantum effects are expected to set in, and the onset temperature of the quantum diffusion is expected to be about one fifth of the Debye temperature of a host lattice, i.e. ∼55 K in Pd considering the Debye temperature of 271 K for Pd [33, 78]. Figure 2.23 shows protium and tritium hopping rates in Pd calculated by the path integral method [72]. This predicts that the diffusion is promoted by the tunneling around the SP in the O-T-O path, reducing the apparent activation energy with decreasing temperature, which results in upward deviation of the hopping rates in the Arrhenius plot at low temperature. This corresponds to tunneling from vibrationally excited states. The calculation also showed that the deviation is more prominent for the protium hopping. Figure 2.24 shows schematic diffusion path of hydrogen in Pd. Considering the potential shape of H in Pd, furthermore, the tunneling regime is expected to change depending on the tunneling path, i.e. either direct O-O path as a shortest path or indirect O-T-O as an energy minimum path, and also on the vibrational levels as to whether H(D) temporarily resides at the T site or not. However, there is still no experimental data of hydrogen diffusion at low temperature in Pd.

2.3.5 Electronic transport

It is known that the resistance increases as the hydrogen(deuteriums) concentration increases in Pd [79, 80, 81], reflecting the change on the density of stages around the Fermi level and the electron mobility due to the hydrogen absorption. Figure 2.25 shows the pressure and the resistance according to the hydrogen concentration at 273 K in Pd. The resistance of the single β phase is twice larger than that of Pd. The decrease in the resistance above $x = 0.7$ is attributed to the improved periodicity of the hydrogen ordering in β phase resulting in the decrease of electron scattering.

Pd shows unique electronic behaviors by hydrogen absorption [82]. PdH_x with $x \sim 0.4$ shows anomalies in resistance, specific heat and the Hall coefficient around 50 K, which is called the 50 K anomaly [26, 83, 84]. This phenomenon was first observed in 1968. Figure 2.26 shows the temperature dependence of the resistance for $PdD_0.58$, where the open circle and the filled circle represent slow and rapid cooling [85], showing that the 50 K anomaly is suppressed by the rapid cooling. A study by the neutron scattering indicated that the long-range ordering of hydrogen atoms occurs by the slow cooling [86, 87]. It is also suggested by a specific heat measurement that the 50 K anomaly is related to the glass transition[88]. Though the origin of the 50 K anomaly is still not clear, at least the 50 K anomaly is associated with the hydrogen diffusion. Since the recovery from the rapidly-quenched metastable state is accompanied by H diffusion, we can expect to analyze the hydrogen diffusion in Pd by a quench-recovery experiment around 50 K. However, few systematic studies have been performed to date [89, 90, 91, 88].

Furthermore, PdH_x with large x of the single β phase region shows a superconductivity, whose critical temperature (T_c) increases as the hydrogen concentration increases [12, 92]. The maximum $T_c \sim 10$ K was reported for specimens with $x \sim 1$. It was experimentally revealed that the type of the superconductor changes depending on the concentration [93]. The inverse isotope effect in the critical temperature was observed between hydrogen and deuterium [94].

2.3.6 Possibility of metastable palladium hydrides

In 2016, Shed *et.al* reported the possibility of the high-temperature superconductivity with $T_c = 54$ K for the metastable Pd specimen hydrogenated at 600 K and 10 MPa and subsequent quenching [95]. It was suggested that the increase in the critical temperature originates from the contribution of the T site occupation, whose phonon frequency is larger than that of the O site occupation

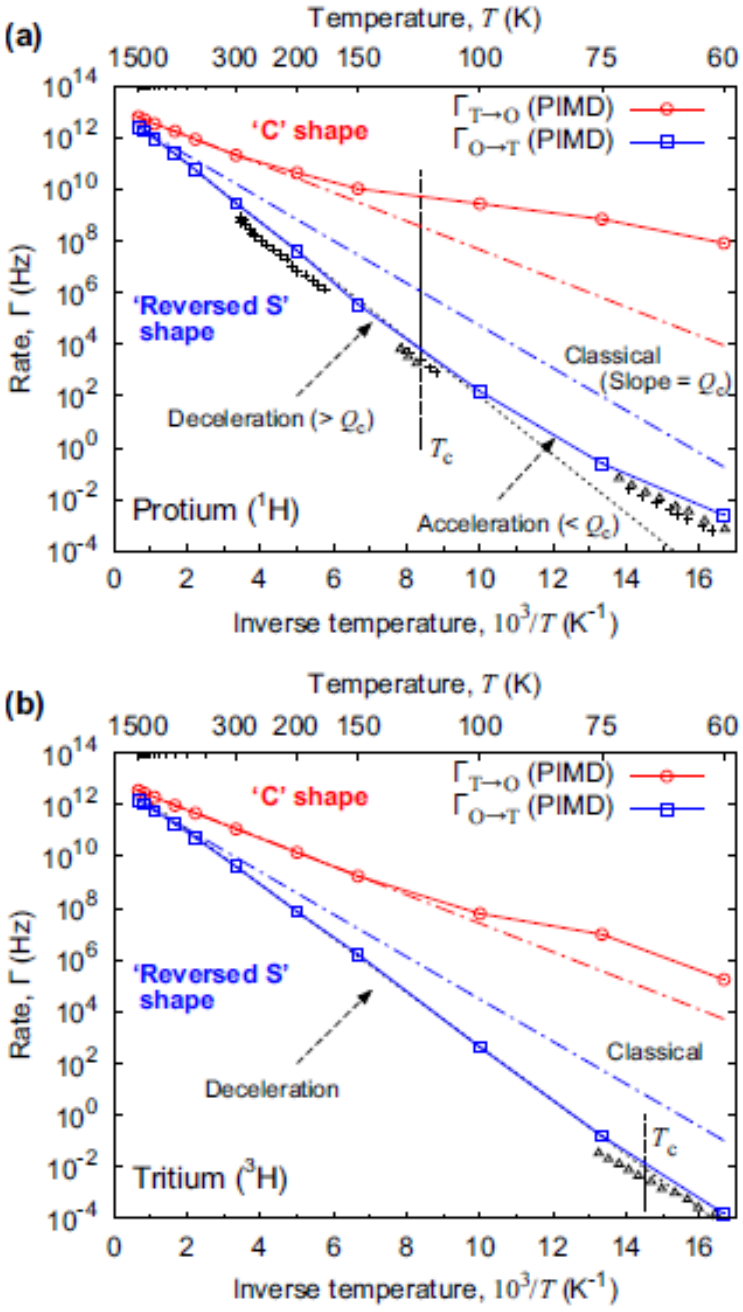

Figure 2.23: Protium and tritium hopping rates in Pd calculated by the path integral method [72].

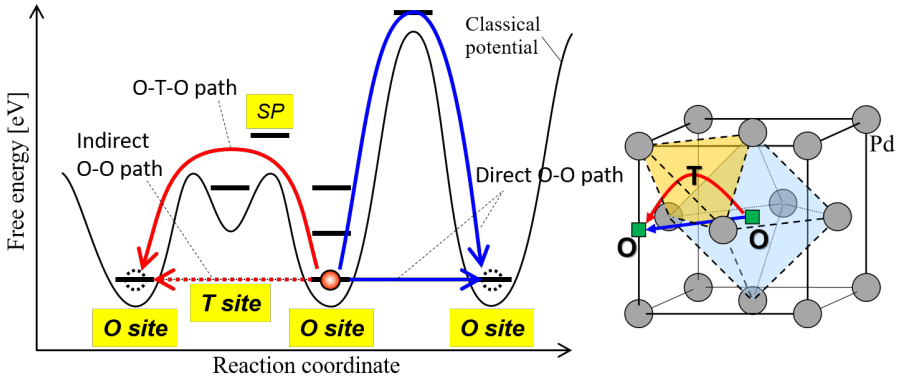

Figure 2.24: Schematic diffusion path of hydrogen in Pd.

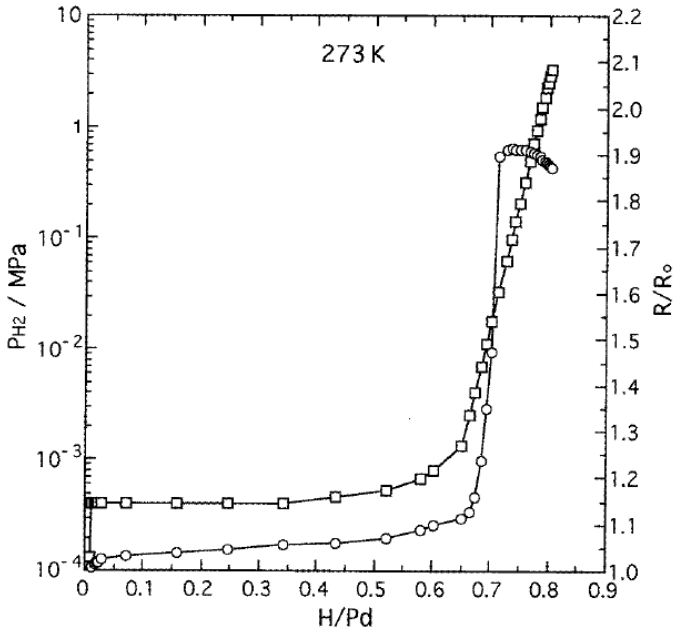

Figure 2.25: Relative resistance (circle) and pressure (square) as a function of hydrogen concentration in PdH_x [80].

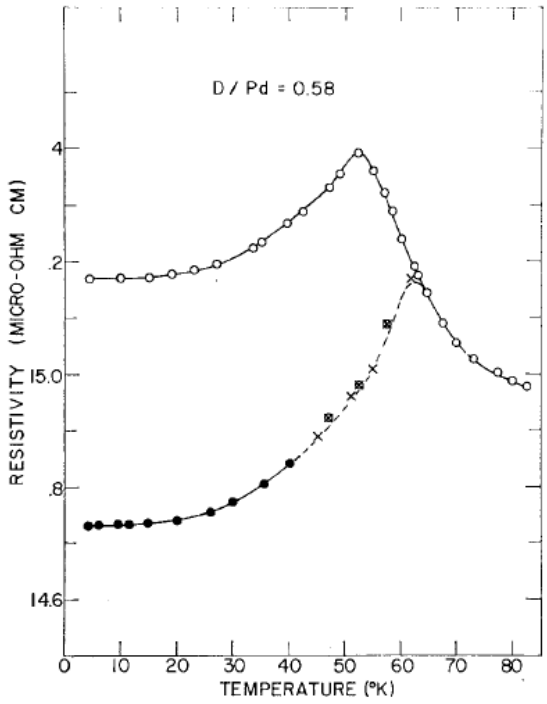

Figure 2.26: Temperature dependence of the PdH_x according to rapid cooling (filed circle) and slow cooling (open circle) [85]. The humps are called the 50 K anomaly.

reflecting the curvature of the potential. This result demonstrated the possibility that the electronic property of metal hydrides changes drastically depending on the hydrogen position, though the consistency of the experiment is still controversial.

Metastable structures of Pd hydrideds formed by various hydrogenation methods were reported. In case of the electrolysis charge, the formation of metastable supersaturated PdH_x with $x > 1$ were reported [18, 21]. Considering that the atomic ratio of O site against Pd is 1, a part of the absorbed hydrogen might be located in T sites though the structure analysis was not performed. The lattice vacancies formed by the electrolysis charge are also expected to be related to the supersaturated composition. The hydrogenation by ion implantation can also form metastable hydrides. Supersaturated PdD_x with $x = 1.6$ by deuterium ion implantation at 41 K was reported [20]. Figure 2.27 shows results of channeling NRA with a non-resonant reaction for the PdD_x formed by the deuterium implantation at 25 K [19]. This reveled that the implanted deuterium atoms are initially located in O site and move to T site above 80 K. T site occupation was also observed by neutron scattering in the PdD_x formed by the gas exposure followed by quenching from $\sim$ 600 K, which corresponds to supercritical region [23].

Hence, Pd hydrides with a metastable structure are possibly formed by quenching, electrolysis charge and ion implantation, in which novel physical properties might be hidden.

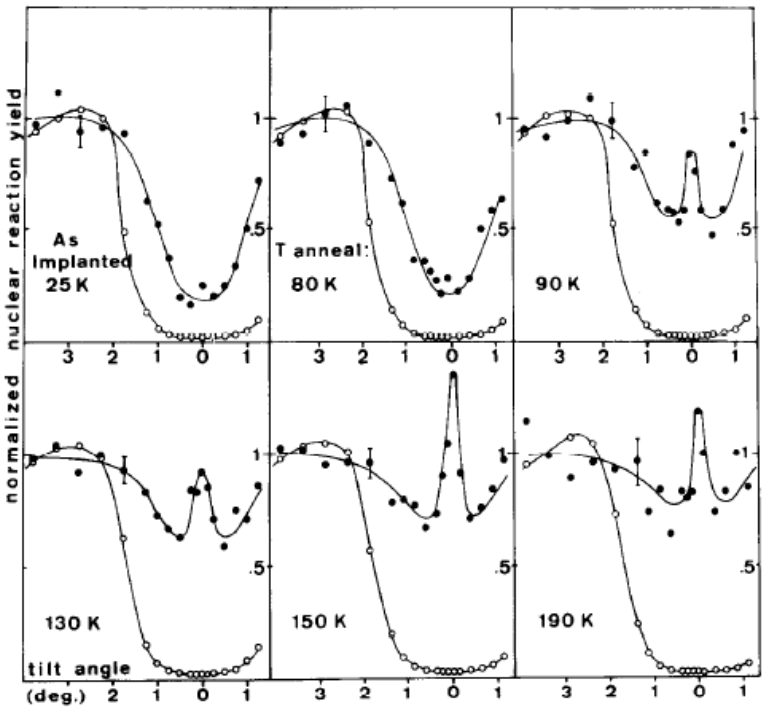

Figure 2.27: Channeling NRA with a non-resonant reaction along the <100> axis for the PdD_x formed by the deuterium implantation at 25 K [19].

Chapter 3

Experiment

3.1 Experimental principle

3.1.1 Resistance measurement

Ohm's law states the current (I) between two points in a material is proportional to the voltage (V) across the points, which is a fundamental principle of electrical resistance measurement. The resistance (R) is expressed as

$$R = \frac{V}{I}. \tag{3.1}$$

Two-terminal and four-terminal resistance measurements are introduced below.

Two-terminal resistance measurement

The two-terminal measurement is used to measure the resistance of samples with relatively large resistance. Figure 3.1 illustrates a schematic picture of the two-terminal resistance measurement under a direct voltage between two points, where the contact resistance and the lead wire resistance are described altogether as R_1 and R_2. R_s and I_s denote the resistance of the specimen and the current through the specimen, and the measured values of the voltage and the current are described as V and I, respectively. Since the internal resistance of the voltmeter is as large as 1 GΩ, I_s is approximated as below.

$$I_s \approx I. \tag{3.2}$$

When a DC voltage is applied between the two points, an equation about V and I is obtained as

$$\frac{V}{I} \approx R_1 + Rs + R_2. \tag{3.3}$$

Therefore, as long as R_s is substantially larger than R_1 and R_2, the measured resistance ($\frac{V}{I}$) corresponds to the sample resistance. In general, the two-terminal measurement is applied for specimens with a resistance larger than ∼1 kΩ.

Four-terminal resistance measurement

The four-terminal measurement is suited to accurately measure the resistance of specimens smaller than 1 kΩ. Figure 3.2 is a schematic picture of the four-terminal resistance measurement under a DC voltage between two points, where R_1, R_2, R_3 and R_4 denote the contact resistances including the resistances of lead wires. I_s and V_s are the current and the voltage through the specimen. Since the internal resistance of a voltmeter is substantially larger than R_3 and R_4, the measured voltage (V) and current (I) are approximated as

$$I_s \approx I, \quad V_s \approx V. \tag{3.4}$$

Therefore, the resistance of the specimen (R_s) is described as

$$R_s = \frac{V_s}{I_s} \approx \frac{V}{I}. \tag{3.5}$$

As you can see from this equation, the contact resistances R_1 and R_2 have no effects on the measured resistance in the four-terminal method. It should be mentioned that if the distance between the terminals connected to the voltmeter and the ammeter is long, the observed $\frac{V}{I}$ is smaller than the true value of the specimen resistance because of the distribution of voltage in the specimen.

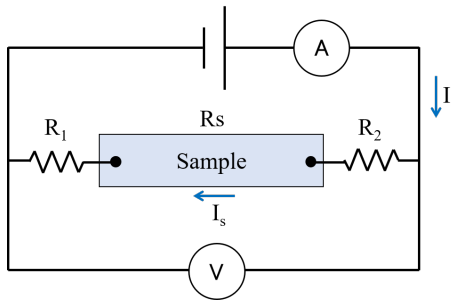

Figure 3.1: Schematic picture of two-terminal resistance measurement.

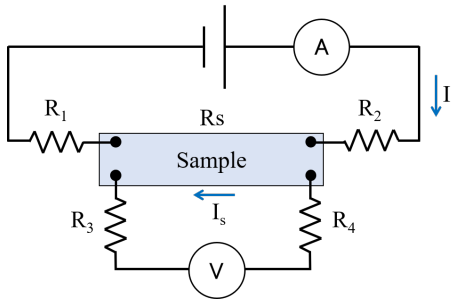

Figure 3.2: Schematic picture of two-terminal resistance measurement.

3.1.2 Thermal desorption spectroscopy

Thermal desorption spectroscopy (TDS), or Temperature programmed desorption, is an experimental method to observe atoms and molecules desorbed from a surface in heating. The adsorption

energies of molecules on a surface and the interaction between adsorbates are evaluated. The area of thermal desorption spectrum corresponds to the amount of molecules adsorbed on and absorbed in materials. Desorbed atoms and molecules are distinguished by the ratio of mass and charge by means of quadrupole mass spectrometer (QMS).

Desorption from surface

Desorption of molecules adsorbed on a surface is described by the Polanyi-Wigner equation [96, 97]. If an elimination reaction is a rate-limiting process, the desorption rate $\nu(t)$ is expressed as

$$\nu(t) = -\frac{d\theta}{dt} = \nu_0 \theta^n \exp\left(-\frac{E_{des}}{k_B T}\right) \tag{3.6}$$

where θ, ν_0, n, E_{dos} and T denote the coverage of adsorbed molecules, the pre-exponential factor, the order of the reaction, the desorption energy and the absolute temperature of the surface, respectively. k_B is the Boltzmann constant. When the temperature of the specimen increases linearly as $T(t) = T_0 + \beta t$, where β is a heating rate, Eq. 3.6 is rewritten as

$$-\frac{d\theta}{dT} = -\frac{d\theta}{dt}\frac{dt}{dT} = \frac{1}{\beta}\nu_0 \theta^n \exp\left(-\frac{E_{des}}{k_B T}\right). \tag{3.7}$$

Figure 3.3 shows simulation results of TDS according to n in which the elimination reaction is a rate-limiting process. The order of n relates the coverage with the desorption rate. The elimination reaction is classified by n as below.

$n = 0$
The desorption with $n = 0$ corresponds to multilayer desorption of adsorbates. Since the desorption rate is independent of the coverage, the onset temperature of the desorption is constant regardless of the initial coverage.
$n = \frac{1}{2}$
This represents the desorption reaction occurring at the edge of a two-dimensional domain of adsorbates. This is because the number of adsorbates in the edge is proportional to $\sqrt{\theta}$.
$n = 1$
This is observed when the desorption event is independent of each other and the interaction between adsorbates is negligible. The desorption with $n = 1$ is also observed for molecules when the desorption occurs by collisions of molecules which move along the edge of the two-dimensional region. The peak temperature of the desorption rate is independent of the initial coverage, and the desorption spectrum is asymmetric with respect to the peak temperature.
$n = 2$
This represents the associative desorption of adsorbates moving on a surface. As the initial coverage increases, the peak temperature of the desorption gets lower as a consequence of the increased collision frequency. The desorption spectrum is symmetric about the peak temperature.

Desorption from bulk

When atoms originally absorbed in a bulk are desorbed from a surface in heating, the atoms need to diffuse from the bulk up to the surface. We consider the case of a film in which the internal diffusion is a rate-limiting process for the desorption. If the absorbed atoms are desorbed from the

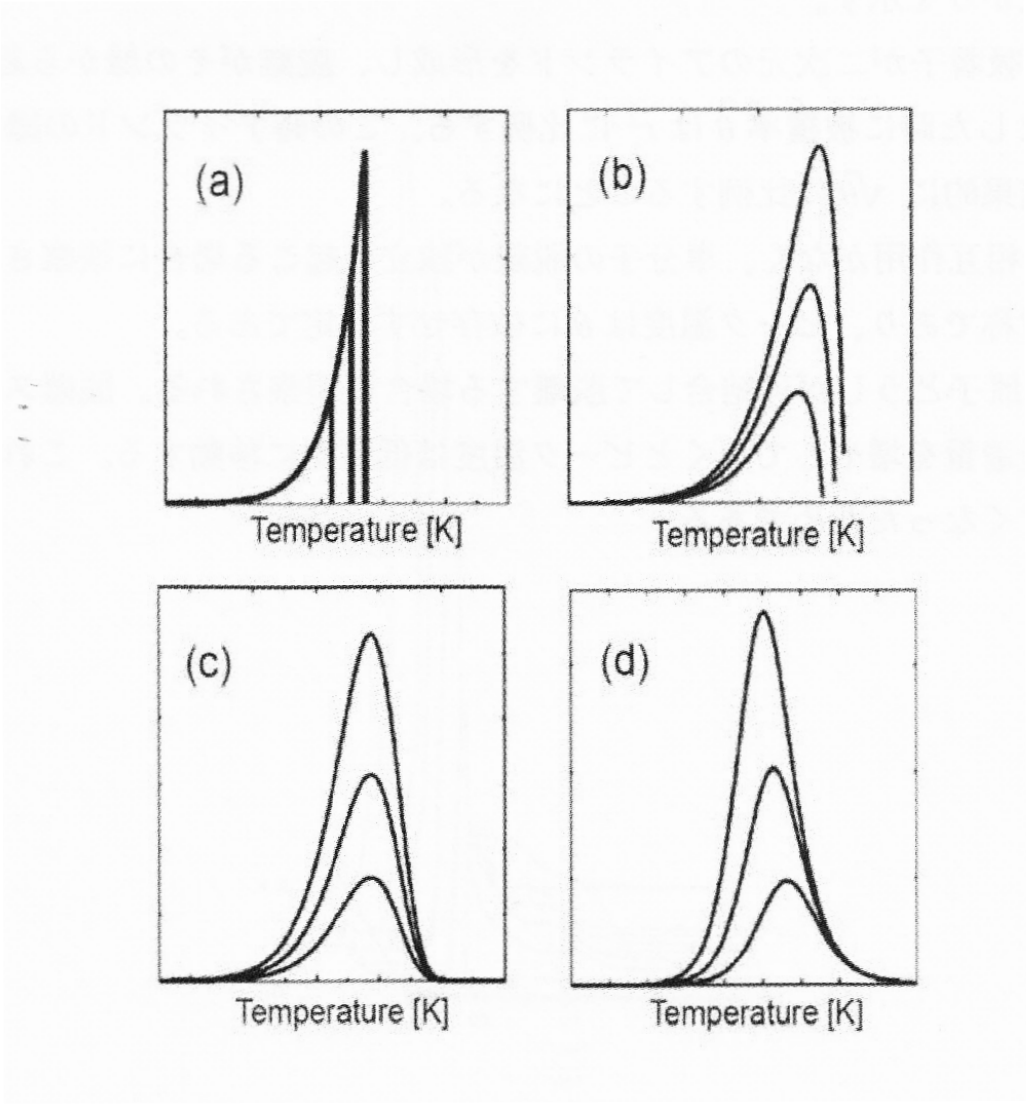

Figure 3.3: Simulation results of TDS according to n in which the elimination reaction is a rate-limiting process. (a)$n = 0$, (b)$n = 1/2$, (c)$n = 1$ and (d)$n = 2$ [98].

both sides of the specimen with a thickness of d, the desorption rate is expressed as

$$\nu(t) = -2D \left.\frac{\partial C(x,t)}{\partial x}\right|_{x=0}, \tag{3.8}$$

where $C(x,t)$ and D represent the concentration distribution of the atoms and the diffusion coefficient. According to the Fick's laws, Eq. 3.8 is rewritten as

$$\nu(t) = \frac{3C_0D}{d} \sum_{n=0}^{\infty} \exp\left[-\left(\frac{\pi(2n+1)}{d}\right)^2 Dt\right], \tag{3.9}$$

where it is assumed that the initial concentration given by C_0 is uniform in the specimen. At high temperature region, the temperature dependence of $D(T)$ is described by using the activation energy E_a and the diffusion constant at $T = \infty$, D_0, as

$$D(D) = D_0 \exp\left(-\frac{E_a}{k_BT}\right). \tag{3.10}$$

In case of liner heating with a heating rate of β, the desorption rate is approximately obtained as [99, 100].

$$\nu(t) \approx \frac{8C_0D_0}{d} \exp\left(-\frac{E_a}{k_B(T_0+\beta T_0)}\right) \times \sum_{0}^{\infty} \exp\left[-\left[\frac{\pi(2n+1)}{d}\right]^2 \frac{D_0k_B(T+\beta t)^2}{\beta E_a} \exp\left(-\frac{E_a}{k_B(T_0+\beta t)}\right)\right]. \tag{3.11}$$

Figure 3.4 shows simulation results of TDS for the specimens with various initial concentrations in which the internal diffusion is a rate-limiting process [99]. The desorption spectra are steep above the peak temperature. It should be mentioned that in the simulation the activation energy E_a is assumed to be independent of the temperature and the concentration, which means that the change in the peak temperature depending on the initial concentration implies the change of the activation energy in the internal diffusion depending on the temperature and/or concentration.

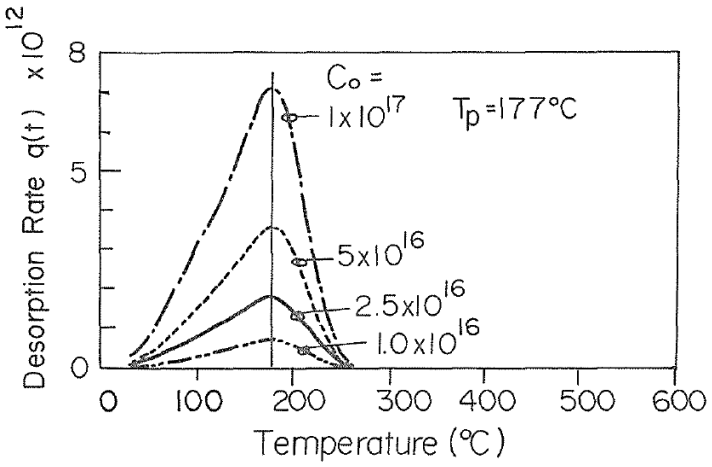

Figure 3.4: Simulation results of TDS according to various initial concentrations in which the internal diffusion is a rate-limiting process. [99]

3.1.3 Nuclear reaction analysis

Nuclear reaction analysis (NRA) is a non-destructive and quantitative method to detect chemical elements in gases and bound to solid materials by using nuclear reaction between a projectile particle and a target element. The resonance NRA via the resonant ^{1}H(^{15}N, $\alpha\gamma$)^{12}C nuclear reaction is used in this thesis, which is a versatile method to directly observe hydrogen atoms on and in materials and quantify the hydrogen concentration versus depth with nanometer resolution [101]. A monochromatized ^{15}N ion beam is delivered onto a specimen. When the ^{15}N ion overcomes the Coulomb barrier and collides with hydrogen atoms, the nuclear reaction with a sharp resonance in the reaction cross section at 6.385 MeV (E_{res}) proceeds as

$$^{15}\mathrm{N} + ^{1}\mathrm{H} \rightarrow ^{16}\mathrm{O}^{*} \rightarrow ^{12}\mathrm{C}^{*} + \alpha, \quad ^{12}\mathrm{C}^{*} \rightarrow ^{12}\mathrm{C} + \gamma, \tag{3.12}$$

where * represents an excited state. The emitted γ-ray has a characteristic energy of 4.4389 MeV [102]. γ-rays are detected by a $Bi_4Ge_3O_{12}$ BGO scintillator. The narrow energy width of the resonance (Γ = 1.8 keV) and the low natural background of γ-radiation around 4.4389 MeV enable the sensitive detection of hydrogen with high depth resolution [103]. When the incident energy (E_i) of ^{15}N is equal to E_{res}, the adsorbed hydrogen on a surface is detected. ^{15}N beams with $E_i > E_{res}$ react with hydrogen below the surface after the ^{15}N ions are decelerated in the specimen down to E_{res} by the stooping power S ($= \frac{dE}{dz}$) specific to materials. Hence, the probing depth d is determined as

$$d = \frac{E_i - E_{res}}{S} \qquad (E_i \geq E_{res}). \tag{3.13}$$

Since the γ-ray yield is proportional to the hydrogen concentration, one can know the concentration of hydrogen atoms at depth d by counting the γ-rays with an energy of 4.43 MeV after calibrating the γ-ray detection efficiency in the experimental setup.

In case of a Pd specimen, the stopping power is given as 3.90 keV/nm, which corresponds to the depth resolution of ~2 nm near the surface for the normal beam incidence, considering the Doppler effect due to the hydrogen vibration in a potential well [103]. Actually, however, the resolution degrades at a larger depth due to the energy struggling of ^{15}N ions in the specimen.

3.1.4 Inelastic neutron scattering

X-ray and electron scattering is not applied to detect light elements since the x-ray and electron beam is scattered by electron clouds in materials and their scattering amplitude is roughly proportional to the atomic number. A neutron, which has no electric charge and spin $\frac{1}{2}$, tends to penetrate through electron clouds and directly be scattered by nuclei. The scattering is a consequence of interaction between a neutron and nuclear states including a spin, which is described as the potential scattering and the resonant scattering. Its scattering amplitude depends non-monotonously on the atomic number. The neutron scattering cross sections for various materials are tabulated in Table 3.1. The neutron scattering cross section for hydrogen and deuterium are equal to or greater than other elements, and so the neutron scattering is a suitable method for their analysis. Elastic neutron scattering is used to analyze the structure using like as x-ray diffraction. Inelastic neutron scattering (INS), on the other hand, reflects local dynamics of atoms and molecules such as vibrations and diffusion by the energy transfer in the scattering. It is noteworthy that the energy of neutrons with a wave length of 1 Å is similar to typical vibrational energies of atoms and molecules (1.8 Å= 25 meV), thus the neutron beams are useful to analyze both of the structure and the dynamics

Element	$\sigma_{coherent}$ (barn)	$\sigma_{incoherent}$ (barn)	σ_{total} (barn)
H	1.7583	80.27	82.03
D	5.592	2.05	7.64
C	5.551	0.001	5.551
O	4.232	0.0008	4.232
Al	1.495	0.0082	1.503
Fe	11.22	0.4	11.62
Ni	13.3	5.2	18.5
Cu	7.485	0.55	8.03
Pd	4.39	0.093	4.483
Ag	4.407	0.58	4.99

Table 3.1: Neutron scattering cross sections. $\sigma_{coherent}$, $\sigma_{incoherent}$ and σ_{total} represent bound coherent scattering cross section, bound incoherent scattering cross section and total bound scattering cross section, respectively. Coherent and incoherent scattering originate from the two possible spins of the compound nucleus formed by the incident neutron and the target nucleus. 1 barn = 10^{-28} m^2.

of hydrogen.

3.1.5 Hydrogenation of Pd

In general, hydrogenation of metals are performed in three ways: hydrogen gas exposure, hydrogen ion implantation and electrolytic reaction. In this thesis, hydrogen gas exposure and hydrogen ion implantation are used.

Gas exposure

Formation of metal hydrides by hydrogen gas exposure proceeds by dissociative adsorption of hydrogen molecules and subsequent internal diffusion of hydrogen atoms. Metal hydrides in thermal equilibrium are formed, and the composition ratio of hydrogen to metals are uniquely determined by temperature and pressure. It is often performed at high temperature and high pressure to enhance the hydrogen diffusion. Conversely, the hydrogenation at low temperature is slow because of the limited hydrogen diffusion. The hydrogen gas exposure at a pressure above ~1 GPa possibly brings about many lattice vacancies in addition to the hydrogenation of a specimen [104, 105, 106].

Ion implantation

Formation of metal hydrides are assisted by the kinetic energies of implanted hydrogen ions. This method can be operated at low temperature at which the hydrogen diffusion is substantially limited, and randomly implanted hydrogen atoms can be frozen in metastable sites resulting in the formation of metastable metal hydride [20]. It is easy for the ion implantation to control the hydrogen concentration by controlling the number of the incident ions, and formation of lattice vacancies is controlled by the implantation energy. On the other hand, formation of metal hydrides with a perfectly uniform hydrogen concentration is difficult by means of the ion implantation.

Electrolysis

By means of electrolytic reaction, the applied voltage increases the chemical potential of protons and assists the formation of metal hydrides. Electrolysis has a possibility to form supersaturated metal hydrides [18, 21]. On the other hand, the hydrogenation is impossible at low temperature where an electrolytic solution freezes.

3.2 Experimental apparatus

3.2.1 In siu measurement of resistance and TDS

To evaluate the electrical property of a hydrogenated specimen, we developed an apparatus for simultaneous measurements of resistance and TDS in situ. The experiment is performed in the ultra-high vacuum chamber in which the residual gas pressure evacuated with two TMPs connected in series is below 3×10^{-8} Pa after the baking. Figure 3.5 shows a schematic top view of the apparatus. The sample stage made of Cu is fixed at the tip of the rotatable manipulator, which is located at the center of the vacuum chamber. The chamber is equipped with the ion gun for surface preparation and hydrogen implantation, QMS for TDS and a W filament, to which the sample is faced by the rotation of the manipulator. The energy of the ion gun is controllable between 500 to 3000 eV. The W filament can be electrically heated up to $\sim 1700^{\circ}$. The temperature of the specimen is measured by the Si diode sensor located next to the specimen on the sample stage. When TDS is performed, the tip of the QMS approaches near the sample surface and the NEG pump is used for efficient pumping of hydrogen gas in QMS.

The manipulator is cooled by a 4K-Gifford-McMahon (GM) refrigerator. At low temperature below ~30 K, heat transfer by thermal radiation is no longer ignorable. According to the Stefan–Boltzmann law, the total energy (q) radiated per unit surface area and unit time from a material at temperature (T) is give as

$$q = \epsilon \times \sigma \times T^4, \tag{3.14}$$

where σ (=5.67 $\times$ 10^{-8} [W/(m^2 $\cdot$ K^4)]) and ϵ represent the Stefan–Boltzmann constant and the emissivity of the gray body, respectively. ϵ depends on materials and surface gloss, and it is known that ϵ of Al and Cu is relatively small. In the present apparatus, the manipulator is surrounded by the radiation shield with a temperature of ~50 K made of Al and Cu, as shown in Figures 3.6 and 3.7. The radiation shield is opened only above the specimen when the hydrogen ion implantation and TDS are operated. Furthermore, wires made of phosphor bronze are used to reduce the heat transfer by thermal conduction from electrical wires. The sample can be cooled below 2.8 K when the radiation shield is completely closed. The sample is heated up to ~600 K by a ceramic heater.

Figure 3.8 shows the sample stage. The resistance measurement are performed by the four-terminal method. Four Au wires with a diameter of 0.1 mm connected to the phosphor bronze wires for the 4-terminal resistance measurement are fixed on the sample surface by In.

3.2.2 Nuclear reaction analysis

The resonance NRA measurement using the resonant ^{1}H(^{15}N, $\alpha\gamma$)^{12}C nuclear reaction was performed in MALT at the University of Tokyo in this thesis. Monochromatized $^{15}N^{2+}$ ions (ΔE = 3 keV) accelerated by an electrostatic accelerator are delivered onto a specimen in an ultra-high vacuum chamber with a base pressure below 1×10^{-5} Pa. Figure 3.9 illustrate the vacuum chamber. γ-rays are detected by the BGO scintillator surrounded by a Pc shield. The chamber is equipped

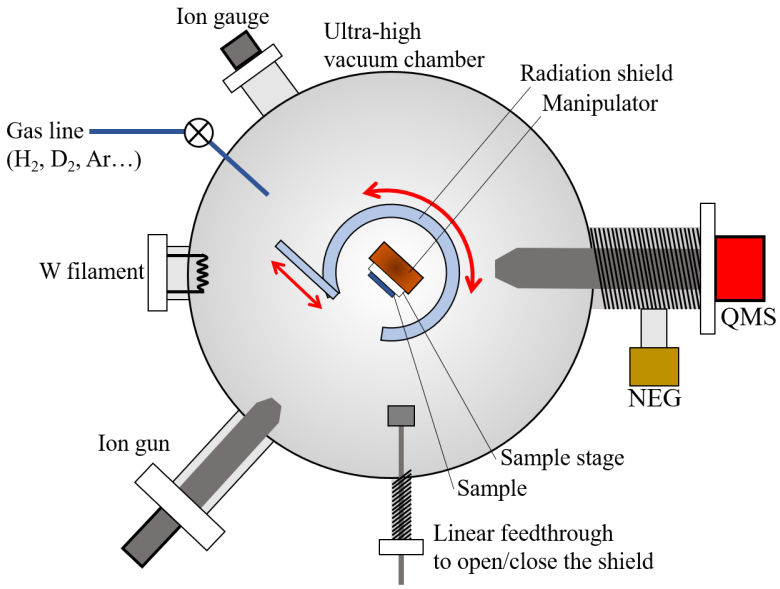

Figure 3.5: Schematic top view of the vacuum chamber for the simultaneous measurement of resistance and TDS.

Figure 3.6: Radiation shield surrounding the manipulator with the sample stage.

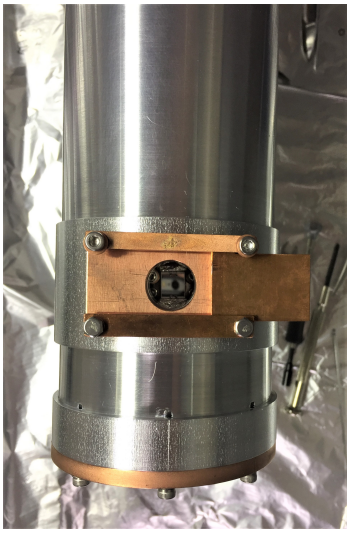

Figure 3.7: Radiation shield when it is opened for hydrogen ion implantation and TDS. The diameter of the window is 15 mm.

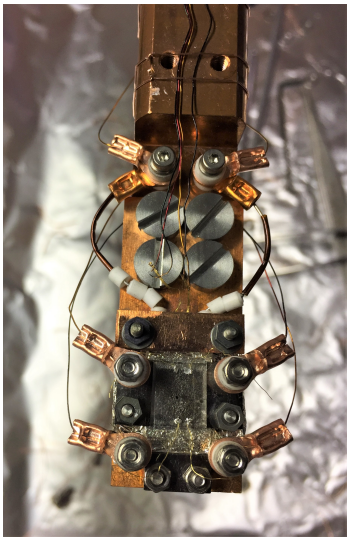

Figure 3.8: Sample stage with a sample.

with the ion gun for surface preparation and hydrogen implantation, QMS for TDS and LEED for the analysis of surface structure. The specimen is cooled by liquid nitrogen down to 80 K, or by the 4K-GM refrigerator down to 9 K by using a Al shield.

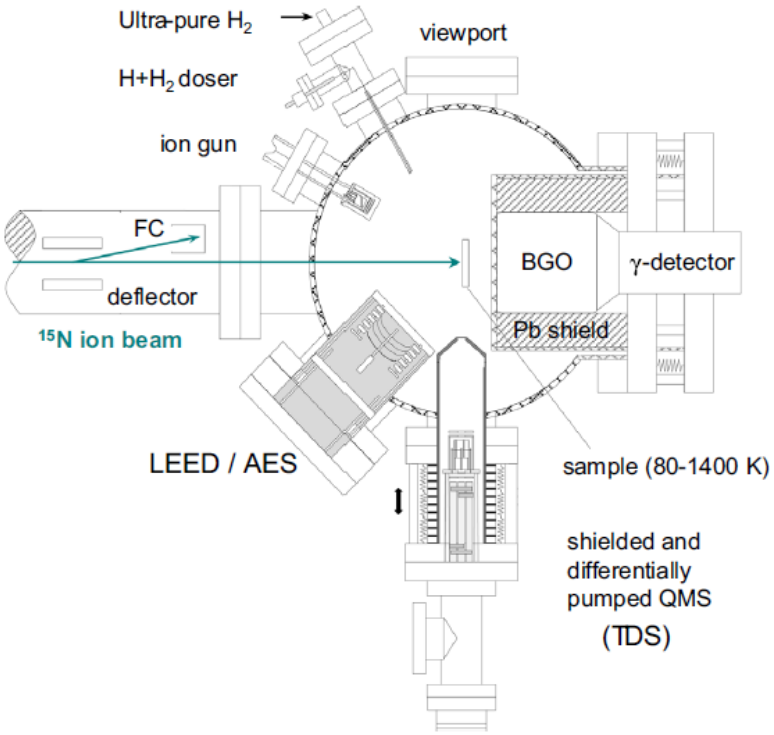

Figure 3.9: The illustration of the UHV chamber for NRA in MALT at the University of Tokyo [101].

3.2.3 Inelastic neutron scattering

INS was performed at the BL-01 (4SEASONS) in J-PARC in this thesis [107]. Figure 3.10 illustrates the apparatus. A selectively monochromatized neutron beam between 5 and 300 meV is delivered on to a sample in a vacuum chamber. The total scattering angle coverage is between -35 and +130° horizontally, and between -25 and +27 ° vertically. The neutron flux at the sample is calculated to be 3×10^5 n/s/cm^2 at an incident energy of 50 meV. Thanks to the high flux and the effective detection, INS is feasible for specimens with weak inelastic signals. The scattered neutrons are detected by ^{3}He tubes surrounding the sample in a vacuum chamber. The multiple-incident-energy measurement using a Fermi chopper is operated in 4SEASONS by the repetition-rate multiplication techniques as schematically shown in Figure 3.11. The energy and momentum transfer is obtained from the analysis of the time-of-flight (TOF) of the neutrons.

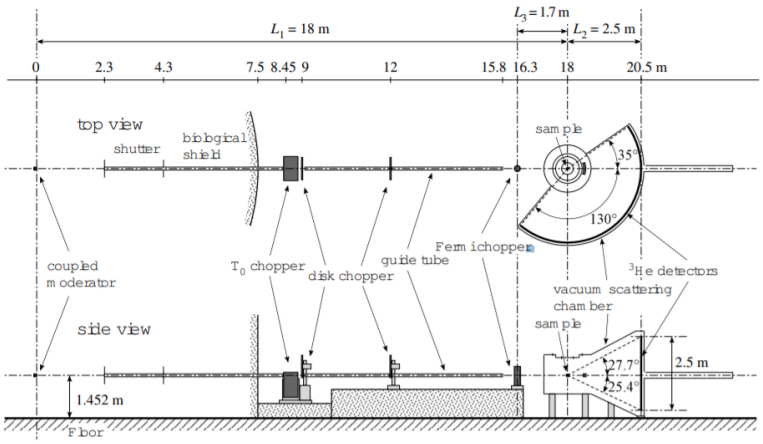

Figure 3.10: The illustration of 4SEASONS in J-PARC [107].

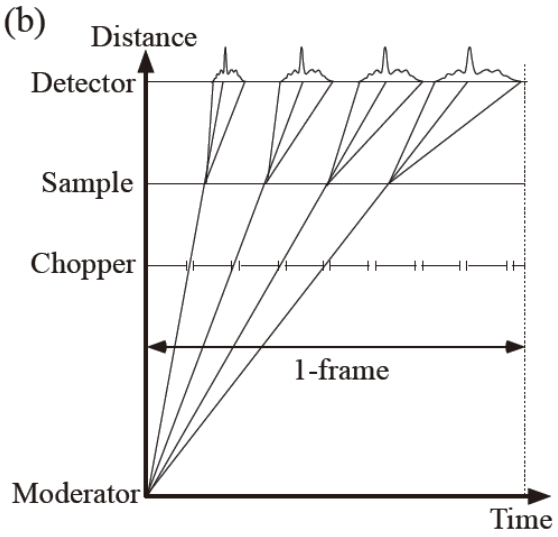

Figure 3.11: TOF diagram of multiple-incident-energy measurement [108].

Chapter 4

Quantum diffusion of hydrogen

Hydrogen diffusion at low temperature in Pd was successfully observed by electrical resistance measurements. The hydrogen hopping is evaluated by taking advantage of metastable states associated with the 50 K anomaly and the hydrogen ion implantation. The experiment of the 50 K anomaly clarifies the hydrogen hopping mechanism and path around the crossover temperature between thermal and quantum regimes. The results derived from the hydrogen ion implantation reveal the non-adiabatic effect of electrons on hydrogen quantum tunneling.

4.1 Principle to detect the hydrogen diffusion

In general, it is difficult to directly observe hydrogen hopping in bulks since an electron beam or x-ray diffraction is not applied to detect hydrogen atoms which a small electronic density. To overcome this problem, we focused on electrical resistivity. Electrical resistivity, reflecting the electronic density of states (DOS) around the Fermi energy and the electronic mobility, is sensitive to the change of the electronic structure. Different hydrides states which have hydrogen atoms in different states such as O or T sites in fcc metals can be distinguished as schematically shown by Figure 4.1.

Since the electrical resistance measurements sense the change in the DOS, the resistance measurement is a useful way to evaluate the time evolution of the relaxation from a metastable to stable states. If the relaxation is caused by hydrogen diffusion, which takes place between inequivalent sites or which induces electronic structure changes such as ordering of hydrogen, the derived resistance relaxation time corresponds to the inverse of the hydrogen hopping rate as shown schematically by Figure 4.2.

To observe and evaluate the hydrogen hopping by resistance measurements, fabrication of a metastable state of hydrides is needed as an initial state. Firstly, we focused on the 50 K anomaly of Pd hydrides. This is the phenomenon where an ordered structure of hydrogen atoms in the stable O sites is formed below about 50 K from the disordered state [86, 87]. It has been revealed that a metastable disordered state is frozen by quenching a specimen [85]. Taking advantage of the quenched metastable state related to the 50 K anomaly, we observed the hydrogen diffusion between O sites.

Secondly, we focused on a metastable state of Pd hydrides formed by hydrogen ion implantation at low temperature as an initial state. As is discussed in section 6.1, a part of the hydrogen atoms implanted into Pd are located in the metastable T sites. From the resistance relaxation of the metastable state, we evaluated the hydrogen hopping from T to O sites.

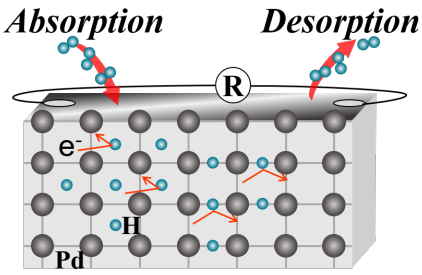

Figure 4.1: Schismatic picture of hydrogen detection by resistance measurement.

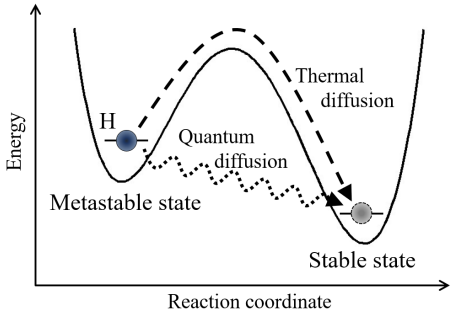

Figure 4.2: Schematic picture of relaxation from metastable to stable states by hydrogen diffusion.

4.2 50 K anomaly

4.2.1 Samples

The sample used in this experiment is a 50nm-thick Pd film deposited on a $SrTiO_3(100)$ substrate by magnetron sputtering at room temperature. Figures 4.3 and 4.4 show the two-dimensional XRD pattern and its corresponding θ-2θ diffraction pattern, which confirmed that the deposited Pd film is polycrystalline. The average grain size derived from the Pd(111) ring is 42.3 nm from Scherrer's equation with the Scherrer constant of 0.9.

4.2.2 Results and discussion

4.2.2.1 Hydrogenation by H_2 gas exposure

Figure 4.5 shows the resistance change of a Pd film with a thicknesses of 50 nm during the hydrogenation under hydrogen gas exposure around 200 K. The exposure pressure of hydrogen gas was between 1 to 1×10^5 Pa. A monotonous increase in the resistance was observed for the elapsed time with increasing H_2 pressure, showing that PdH_x is formed by the hydrogen gas exposure. The sample was kept to be exposed to the hydrogen gas until the resistance change was almost saturated, and cooled under the hydrogen gas under 10 K followed by pumping the gas below 100 K. Some cycles of H_2 gas exposure and pumping were performed at 380 K to promote the hydrogenation and dehydrogenation of the Pd sample before the experiment.

Figure 4.6 shows the simultaneous measurements of TDS of mass 2 and the resistance for the hydrogenated samples with a thickness of 50 nm during heating with a heating rate of 0.6 K/s.

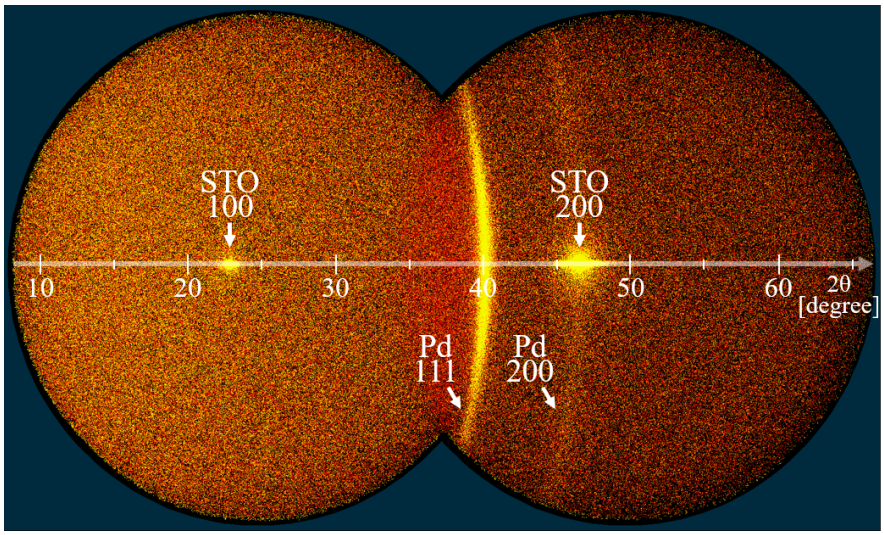

Figure 4.3: Two-dimensional XRD profiles of Pd(50nm/)$SrTiO_3$(100).

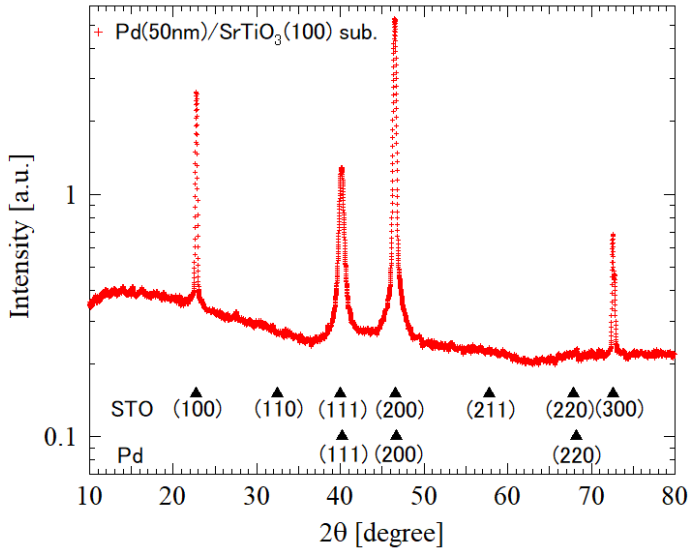

Figure 4.4: θ-2θ XRD pattern for Pd(50nm/)$SrTiO_3$(100).

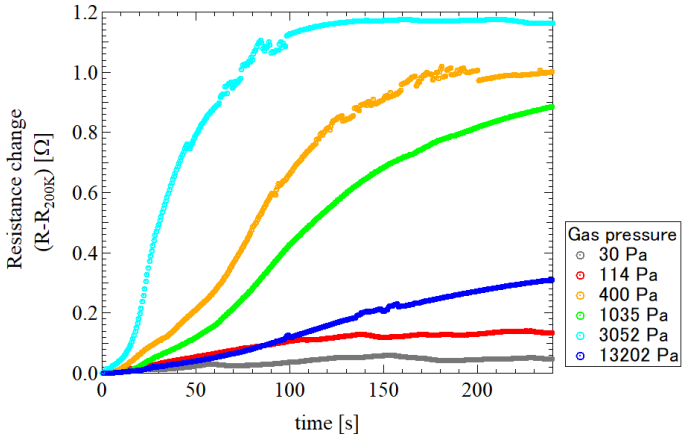

Figure 4.5: Resistance change of the 50-nm-thick Pd film under hydrogen gas exposure with various pressures at 200 K. $R_{200\mathrm{K}} = \sim 1.6\ \Omega$.

A hydrogen desorption peak appeared around 250 K as can been seen in TDS. Its intensity was increased as the exposure gas pressure was increased. In accordance with the hydrogen desorption around 250 K, the increased resistance induced by the hydrogen gas exposure returned to the original value of the resistance for Pd without hydrogen, showing that the resistance recovers in accordance with the transition from PdH_x to pure Pd. The perfect recovery of the resistance confirmed that formation of Pd defects such as vacancy or dislocation was negligibly small in the H absorption and desorption cycles.

Looking at the TDS carefully in Figure 4.6, an additional peak was observed below 200 K for the samples exposed to the hydrogen gas above 10^3 Pa. We calculated the hydrogen absorption energy by the DFT calculation including lattice relaxation as will be mentioned in detail in section 4.2.2.7. The calculation shows that hydrogen absorption energy per one hydrogen atom is 2.54 eV for $PdH_{0.5}$ corresponding to $(\alpha+\beta)$-phase PdH_x, which is larger than that of 2.46 eV for PdH_1 of β-phase PdH_x. Therefore, the additional peak below 200 K in TDS seems to correspond to desorption from the β-phase PdH_x.

On the other hand, the resistance for the sample after the the gas exposure with 0.1 MPa was smaller than that after the exposure with 0.01 MPa. Since the resistance of β-phase PdH_x decreases with increasing hydrogen concentration with reference to the phase diagram of PdH_x, this decrease in resistance indicates the formation of β-phase PdH_x. During heating, as is apparently shown by $(-dR/dT$ in Figure 4.6 (b), the resistance of the Pd exposed to the hydrogen gas with high pressure increased around 200 K followed by the recovery around 250 K. This indicates a transition from β with large x to β with small x or $(\alpha+\beta)$-phases of PdH_x, which is consistent with the TDS results.

NRA measurements were performed for 50-nm-thick Pd films to obtain the hydrogen depth distribution in bulk. Figure 4.7 shows NRA results at 89 K for the samples after hydrogen gas exposure at 1012 and 100 Pa at 200 K. Hydrogen distribution after the hydrogenation followed by 380 K heating is also shown in Figure 4.7. The peak around 0 nm corresponds to adsorbed H and/or H_2O on the surface. The hydrogen depth distribution in the Pd film is uniform after the hydrogenation, and the absorbed hydrogen atoms are completely desorbed by the heating up to 380 K.

The results of resistance measurement and TDS for the Pd film after the deuterium gas exposure confirmed that the resistance behavior of PdD_x is similar to PdH_x.

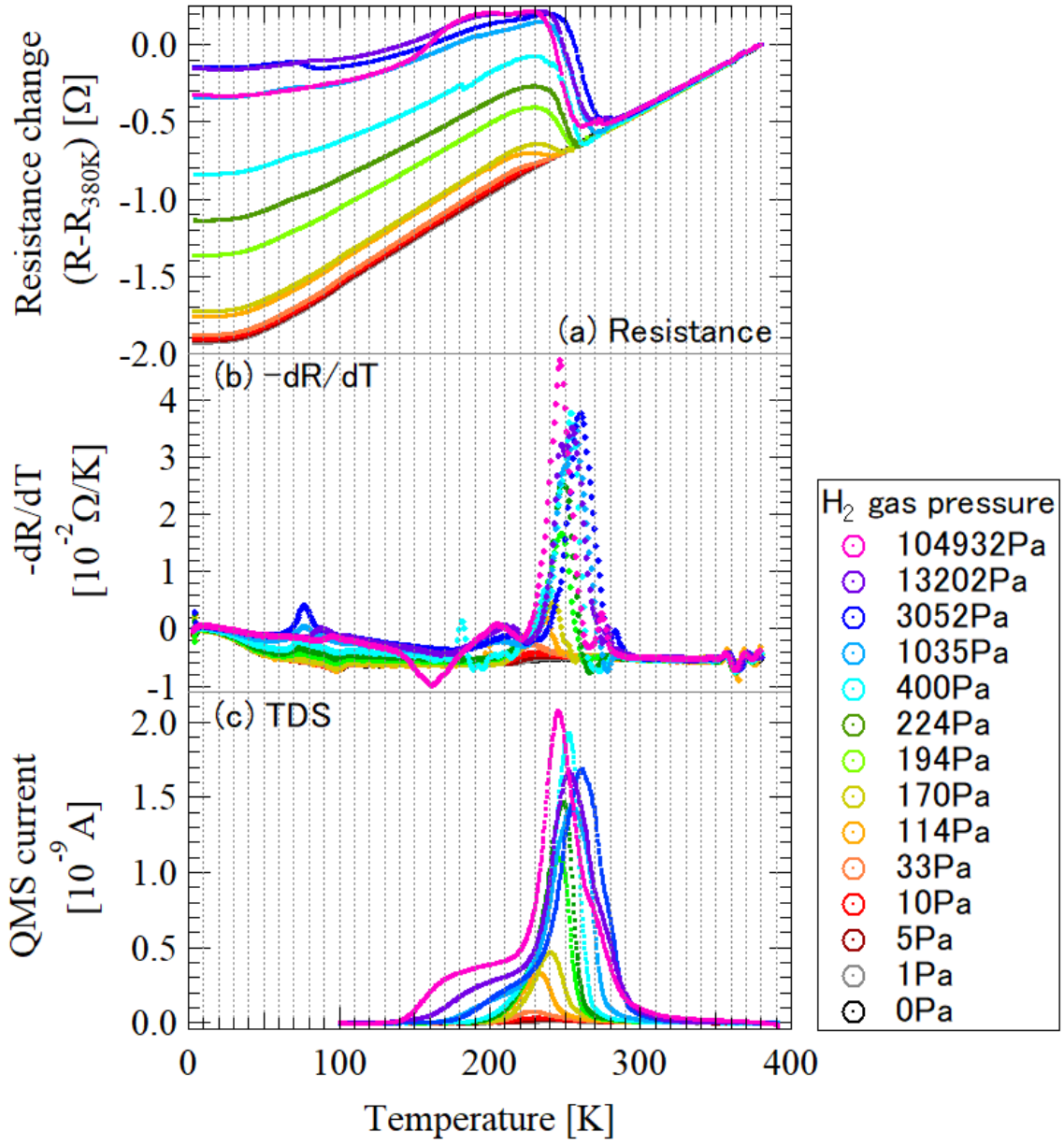

Figure 4.6: The result of simultaneous measurement of resistance and TDS for the 50-nm-thick Pd film after hydrogen gas exposure with various pressures at 200K. (a) resistance referred to that at 380 K (R_{380K} = ~2.6 Ω), (b) temperature deferential of the resistance and (c) TDS.

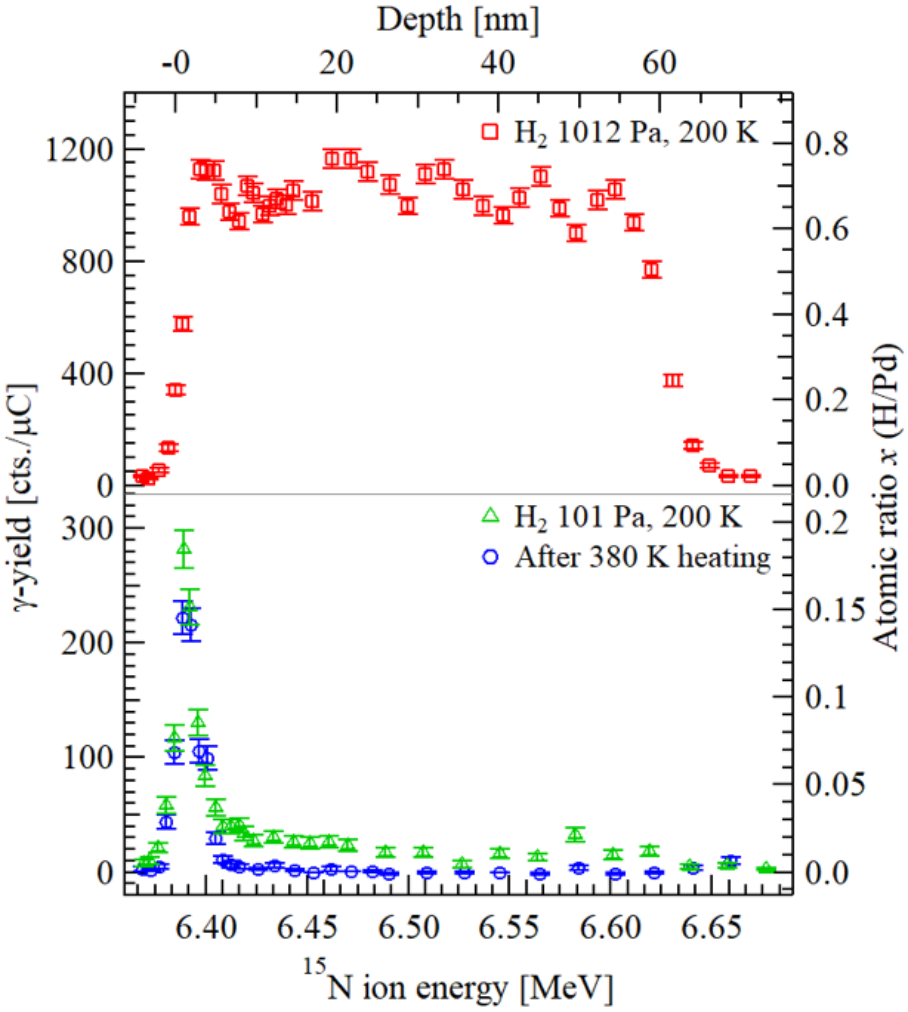

Figure 4.7: Hydrogen depth distribution obtained by NRA at 89 K for the 50-nm-thick Pd film after the hydrogen gas exposure with 1012 Pa and 101 Pa. The result after the subsequent heating up to 380 K is also shown.

Figure 4.8 shows a relationship between the gas pressure at 200 K and the hydrogen concentration obtained from the simultaneous measurement of TDS and resistance, where the atomic ratio x of $PdH(D)_x$ is estimated from the TDS intensity by assuming $x = 0.82$ at 0.1 MPa for H and $x = 0.79$ at 0.1 MPa for D [109]. A plateau at $x \simeq 0.1$-0.6 indicates the (α+β)-phase for both PdH_x below 10^3 Pa, and β-phase PdH_x is confirmed above it. This is consistent with the additional peak in TDS and the resistance decrease for the sampled exposed to high pressure hydrogen gases. These properties are consistent with previous studies for bulk Pd [71]. The concentration of absorbed hydrogen derived by TDS is consistent with the estimation by NRA though a slight difference of the derived x between the NRA and TDS may be attributed to the difference in the effective H_2 gas pressure on the sample surface in the different vacuum chambers.

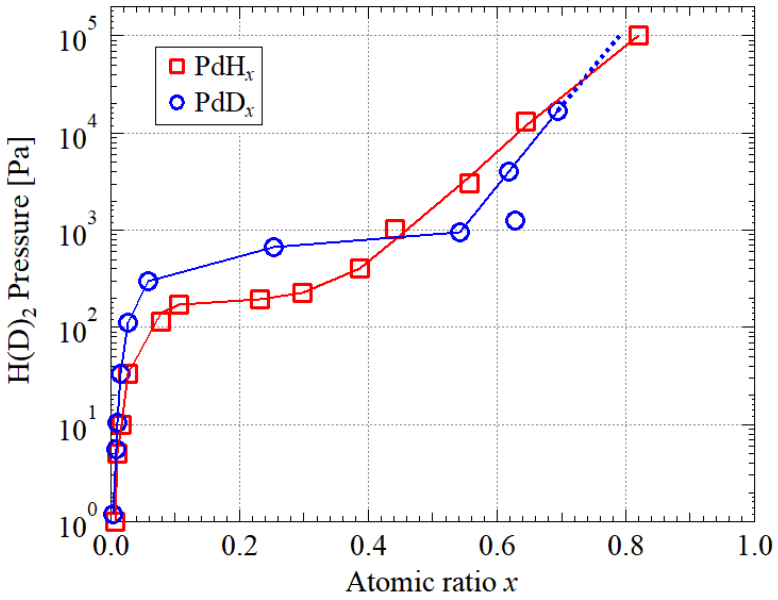

Figure 4.8: Relationship derived from TDS in Figure 4.6 between hydrogen(deuterium) gas pressure and atomic ratio x for the 50-nm-thick Pd film. It is assumed that $x = 0.82$ at 0.1 MPa for H and $x = 0.79$ at 0.1 MPa for D [109].

4.2.2.2 Appearance of the 50 K anomaly in resistance

Figure 4.9 shows the resistance measurement during cooling for the 50-nm-thick PdH_x with various $x's$. A hump in the resistance appeared around 60 K for PdH_x with $x \geq 0.23$, which corresponds to the 50 K anomaly. As x increases, the anomaly was enhanced in the (α+β) phase and subsequently suppressed in the β phase. This indicates a partial existence of the β phase is related to the 50 K anomaly. Figure4.10 shows the resistance change of the specimen with $x = 0.56$ during cooling at various cooling rates. The anomaly was suppressed when the cooling was faster. Since no hydrogen desorption was detected by QMS in this temperature region and the resistance change was reproduced in heating and cooling cycles below 100 K, this resistance change of the 50 K anomaly is induced by an internal structure change, which is consistent with previous studies [86, 87].

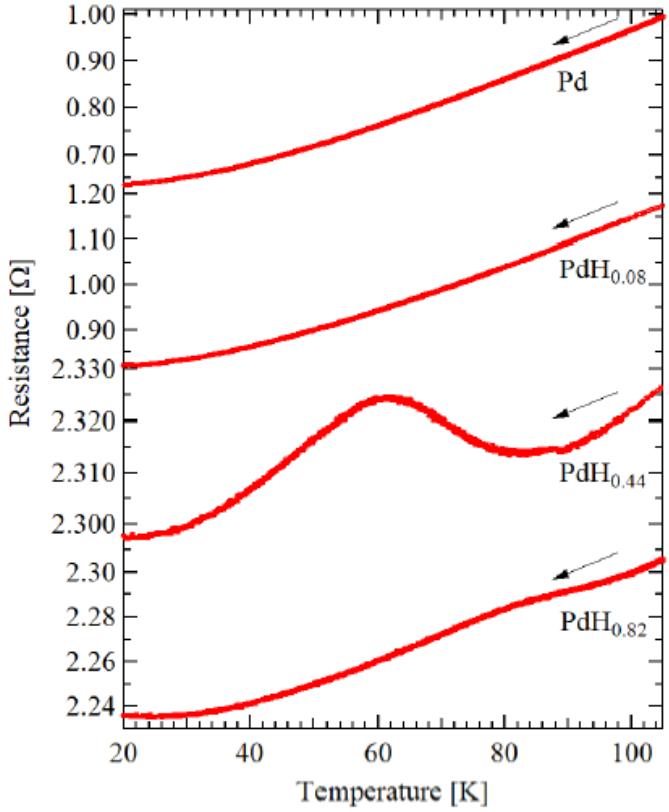

Figure 4.9: Resistance change in cooling of the 50-nm-thick PdHx with various $x's$.

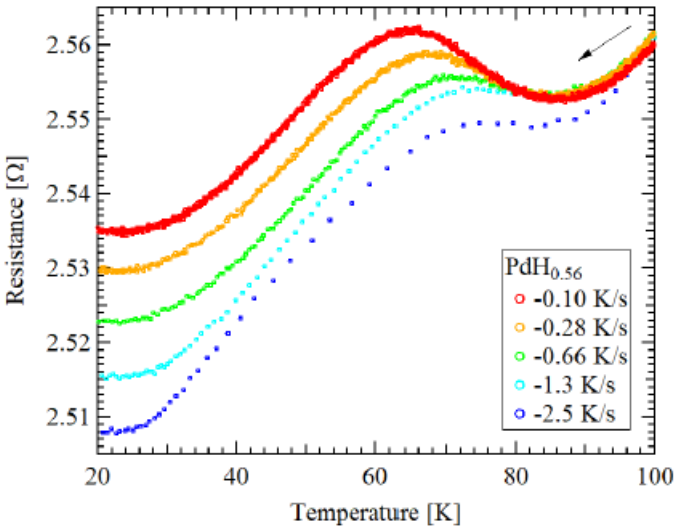

Figure 4.10: Resistance change of the 50-nm-thick $PdH_{0.56}$ in cooling with various cooling rates.

4.2.2.3 Relaxation of resistance

Figure 4.11 shows the time evolution of the resistance of $PdH_{0.30}$ kept at 52.5 K after rapid cooling from ~100 K to 3 K with a rate of -2.5 K/s. Also shown in Figure 4.11 is the temperature change as it was elevated from 3 K to 52.5 K at a constant heater power, resulting in an exponential dependence of the temperature on time with a time constant τ_1 as shown by the dotted line. The resistance relaxation was successfully observed and the resistance increased as time (t) elapses. Accordingly, the resistance change $R(t)$ is described by a sum of two exponential functions as below, one of which has the time constant τ_1;

$$R(t) = R_1 \exp(\frac{-t}{\tau_1}) + R_2 \exp(\frac{-t}{\tau_2}) + C, \tag{4.1}$$

where τ_2, R_1, R_2, and C are constants. The first and second terms originate from the temperature change and the internal structure change, respectively, where the latter represents the relaxation from the quenched metastable state to the stable state (MTS). An approximation result was shown by the a dashed-and-dotted line in Figure 4.11. It is reasonable to assume that this structure change is closely related to internal H diffusion because Pd self-diffusion is much slower in this temperature region [110]. The enthalpy change in the ordering at 44 K was measured to be 0.33 meV per one H atom in $PdH_{0.638}$ by means of adiabatic calorimetry [88]. Since this small value does not account for the relaxation rate observed in Figure 4.11, there is an activation barrier that governs the MTS change. Considering the 50 K anomaly is a disorder-to-order transition of hydrogen atoms in the O sites, it is reasonable to suppose that hydrogen diffusion is the rate-determining step in the MTS process, and that τ_2^{-1} represents the hydrogen hopping rate between O sites. It should be noted that τ_2^{-1} is a lower limit of the real hopping rate, because hydrogen might take a few hopping steps until it reaches the ordered stable state, which do not involve the resistance change.

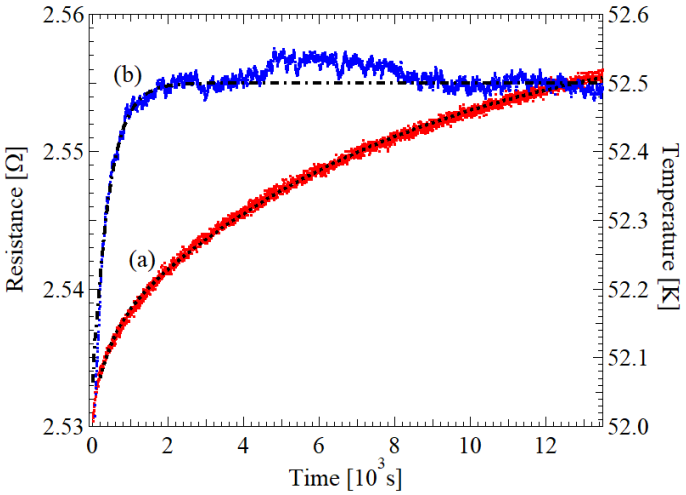

Figure 4.11: Time evolutions of (a) the resistance of the 50-nm-thick $PdH_{0.30}$ and (b) the temperature after the rapid cooling from ~100 K to 3 K.

The temperature dependence of τ_2^{-1} for PdH_x with various $x's$ is shown in Figure 4.12. An extrapolation of the thermal over-barrier hopping with an activation energy of 0.23 eV for hydrogen is represented by a dashed line [74, 75]. It is clear that the hopping rates are larger at low tempera-

ture than the extrapolations of the thermal diffusion. This upward deviation is a clear manifestation of the nuclear quantum effects. As can been seen in Figure 4.12, as the hydrogen concentration increases, the hydrogen hopping rates above 50 K are suppressed. In contrast, the hydrogen hopping rates below 50 K are similar regardless of the concentration. For small x, the hopping rate of hydrogen calculated by the path integral method smoothly connects the experimental data with the thermal hopping curve [72], while the hydrogen hopping rates considerably deviates from the thermal hopping line. Since this calculation takes into consideration the quantum tunneling around the top of the barrier, the present result suggests that the quantum tunneling at vibrationally excited states is prominent for the H diffusion above ~60 K. On the other hand, for large x, the hydrogen hopping rates are connected to the thermal hopping line.

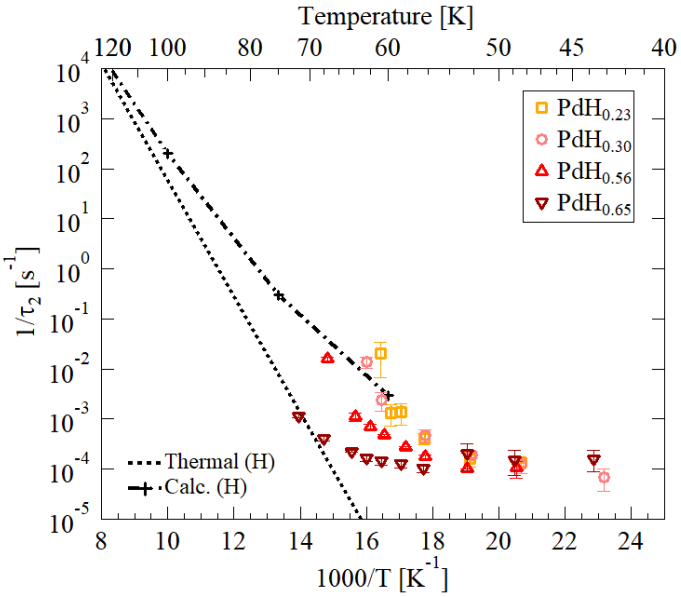

Figure 4.12: Temperature dependence of τ_2^{-1} for the PdH_x with various $x's$. τ_2^{-1} corresponds to the hoping rate. The dashed and the dash-dotted line represent the extrapolation of the thermal over-barrier hopping with an activation energy of 0.23 eV and the calculation result, respectively. [74, 75, 72].

In a similar way, the temperature dependence of τ_2^{-1} representing the deuterium hopping rate was obtained from the the resistance relaxation of the quenched PdD_x as shown in Figure 4.13. The extrapolation of the thermal over-barrier hopping with an activation energy of 0.206 eV for deuterium is represented by a dashed line [74, 75]. Note that the inverse isotope effect in the thermal diffusion of hydrogen and deuterium was observed. Derived D hopping rates are smoothly connected to the thermal hopping line around 65 K unlike the H hopping. It should be noted that the difference in the hopping rate between the two isotopes is small below ~60 K.

4.2.2.4 Analysis of the experimental data

We analyze the temperature dependence of the hopping rates taking account of the nuclear quantum effects. Three types of hopping mechanisms are considered as mentioned in section 2.1.3; (1) over-barrier hopping (OBH), (2) quantum tunneling via excited states (TE) and (3) quantum tunneling

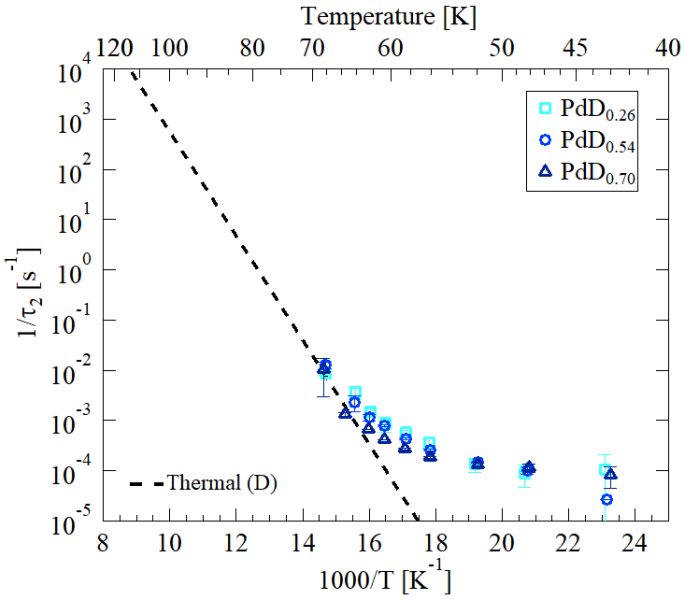

Figure 4.13: Temperature dependence of τ_2^{-1} for the PdD_x with various $x's$. τ_2^{-1} corresponds to the hoping rate. The dashed represent the extrapolation of the thermal over-barrier hopping with an activation energy of 0.206 eV [74, 75].

from the ground state (TG), which are schematically described in Figure 4.14. The total hopping rate ν at temperature of T is expressed as

$$\nu = \nu_{OBH} \exp(\frac{-E_a}{k_B T}) + \sum_{n=1}^{N} \nu_n \exp(\frac{-E_n}{k_B T}) + \nu_{TG} T^{\alpha}, \tag{4.2}$$

where k_B is the Boltzmann constant. The first term represents OBH prevalent at high temperature, where E_a and ν_{OBH} are an activation energy and a frequency factor, respectively. The second term corresponds to TE, where tunneling occurs via vibrationally excited states with energies of E_n (n : the excitation number) [29, 30]. The hopping rate is described by the product of the tunneling and thermal excitation probabilities, where ν_n is a prefactor including the bare tunneling probability. The hopping rate of TG is expected to slightly depend on temperature as T^{α} due to interaction with phonons and electrons [4, 2, 34, 31, 36]. This process should be dominant at low temperature. By taking into consideration two terms for TE, we fit Eq. 4.2 to the experimental data with ν_n, E_n, ν_{TG} and α fit parameters. Here, we fixed ν_{OBH} and E_a at the values reported in previous studies [74, 75].

As shown in Figure 4.15 (a), the experimental results of both hydrogen and deuterium are well described by Eq. 4.2 in a wide temperature range. Since TE terms of $n \geq 2$ were not significant for D, we fitted Eq. 4.2 with TE of $n = 1$ to the data of D. The obtained fit parameters are tabulated in Table 4.3. The predominant terms are presented in Figure 4.15 (b). Above ~100 K, OBH is dominant for both H and D. At T = 50-100 K, on the other hand, a TE term dominates the H diffusion, whereas TE is not significant for D. The activation energy of the dominant TE for H is derived to be 0.15 eV. This value is similar to the second vibrational excitation energy of H in the O site [15, 30, 111, 112, 113], suggesting that the thermal excitation to the second vibrational state in

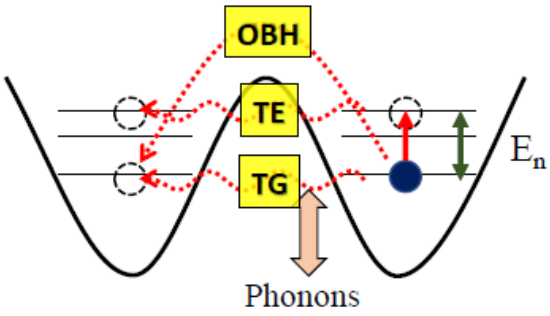

Figure 4.14: Schematic picture of diffusion by OBH, TE and TG.

the O site is involved in the H hopping. Note that the H hopping rate becomes larger than that of D below 85 K despite the inverse isotope effect for OBH, which is in agreement with the calculation result [72]. Figure 4.15 (b) also shows that TG is dominant for both H and D below 50 K, and α was derived to be about 3 for both isotopes.

4.2.2.5 WKB approximation

We discuss TE and TG within the one-dimensional Wentzel-Kramers-Brillouin (WKB) approximation. The bare tunneling probability W for a particle with mass m and energy E_n and the hopping probability P_n of TE is given as

$$W = \exp(\frac{-2}{\hbar}\int_{l_1}^{l_2}\sqrt{2m[V(x)-E_n]}dx) \tag{4.3}$$

$$P_n = W\exp(\frac{-E_n}{k_BT}), \tag{4.4}$$

where the hopping probability P_n is described by the product of the tunneling and thermal excitation probabilities. P_0 corresponds to the hopping probability of TG. Two geometric paths of the direct O-O and the O-T-O are considered as schematically shown by Figure 4.16. One-dimensional model potentials for the two paths were constructed based on the theoretical potential including the zero-point vibrational energies at the O site, T site, and the saddle point of the transition states [72]. The model potential for hydrogen ${}^{\mathrm{H}}_{\mathrm{O-T-O}}V(x$ is described as a sixth-degree equation for the O-T-O path of ${}^{\mathrm{H}}_{\mathrm{O-T-O}}V(x) = \epsilon_0 + \epsilon_1(x^2-a^2)(x^2-b^2)(x^2-c^2)$, where $\epsilon_0 = 0.15$ eV, $\epsilon_1 = 71500$ eV/nm^6, $a = 0.18$ nm, $b = 0.116$ nm and $c = 0.023$ nm, and the ${}^{\mathrm{H}}_{\mathrm{O-O}}V(x)$ for the O-O path is described as a quartic equation of ${}^{\mathrm{H}}_{\mathrm{O-O}}V(x) = \epsilon_2 + \epsilon_3(x^2-d^2)(x^2-e^2)$, where $\epsilon_2 = 0.24$ eV, $\epsilon_3 = 1520$ eV/nm^3, $a = 0.174$ nm and $b = 0.072$ nm. For deuterium, model potentials are described as ${}^{\mathrm{D}}_{\mathrm{O-T-O}}V(x) = \epsilon_4 + \epsilon_5(x^2-a^2)(x^2-b^2)(x^2-c^2)$, where $\epsilon_4 = \epsilon_0 \times 0.206/0.23$ eV and $\epsilon_5 = \epsilon_1 \times 0.206/0.23$ eV/nm^6 for the O-T-O path, and ${}^{\mathrm{D}}_{\mathrm{O-O}}V(x) = \epsilon_2 + \epsilon_3(x^2-d^2)(x^2-e^2)$ for the O-O path. The constructed model potentials for H and D are shown in Figure 4.17.

There are two paths of the direct O-O and the O-T-O as shown schematically in Figure 4.16. The direct O-O path is the energy minimum path for hydrogen(deuterium) to hop between neighboring O sites. In the O-T-O path, there are two possible channels of tunneling with and without residence at the T site. As seen in Figure 4.18, H might be able to tunnel between the O sites without residing at the T site when H is in low vibrational states at the O site, which we call the

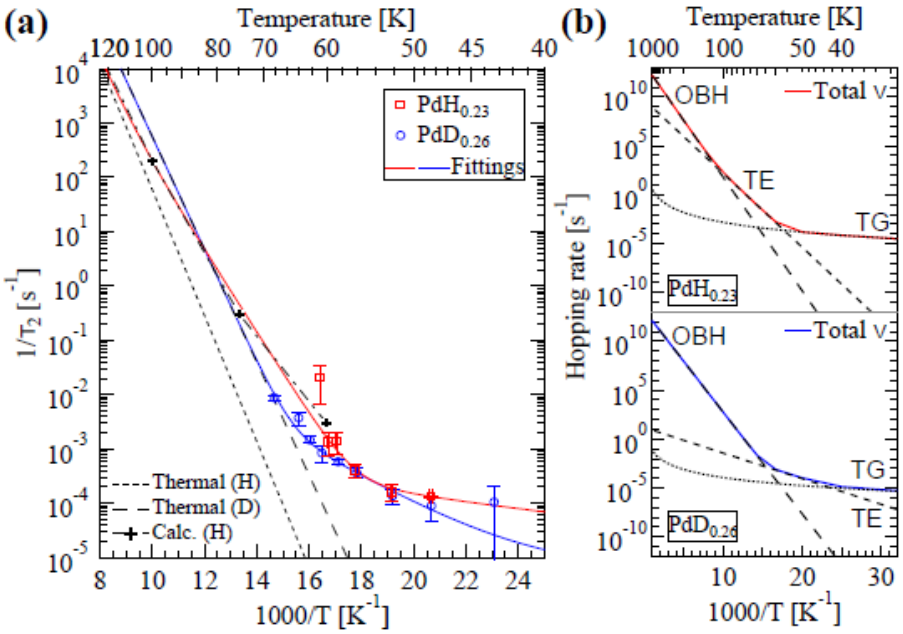

Figure 4.15: (a) Temperature dependence of the H(D) hopping rates in $PdH_{0.23}$ and $PdD_{0.26}$ derived from the time evolution of the resistance. Solid curves are fit results using Eq. 4.2. Dashed lines and the dash-dotted curves present extrapolations of the thermal over-barrier hopping rates and the calculation [74, 75, 72]. (b) Predominant terms of the fit results with Eq. 4.2.

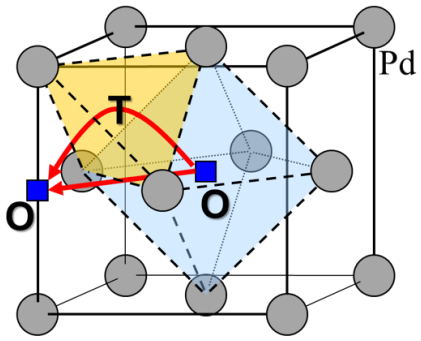

Figure 4.16: Two geometric hopping paths of O-O and O-T-O in Pd.

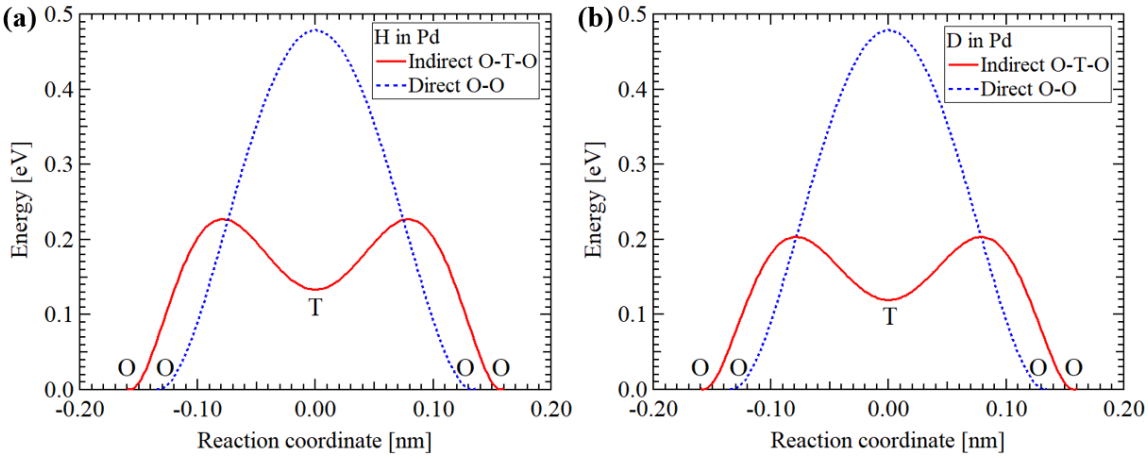

Figure 4.17: The model potentials for (a) hydrogen and (b) deuterium.

indirect O-O path. When H is at higher vibrational levels at the O site, on the other hand, H might temporarily reside at the T site during tunneling between the O sites, which we call the O-T path; the total hopping rate of the latter is approximated by the O-T hopping rate because the hopping from the T to the O sites is sufficiently fast and the O-T hopping is rate-limiting as confirmed by the theoretical calculation [72].

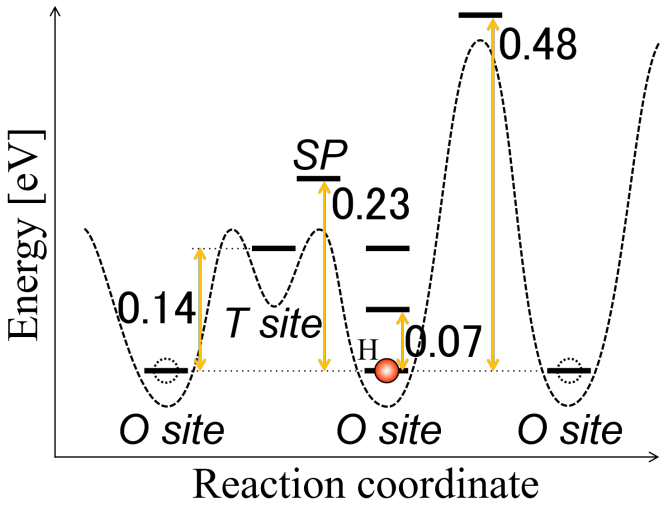

Figure 4.18: Schematic drawing of potential for H in Pd.

Figure 4.19 shows the WKB calculation results of P_n for the three paths of the O-T, indirect O-O and direct O-O hopping for H with the vibrational energy $E_n = 0.07 \times n$ eV in the O site [15, 30, 111, 112, 113]. O_{ground} represents the H in the ground state and O_n represents the H in the n-th vibrationally excited state. This result shows that the H hopping occurs via the direct and/or indirect O_{ground}-O tunneling below ~40 K and via the O_{2nd}-T tunneling above ~40 K. Neither direct nor indirect O-O hopping is significant above ~40 K because the barrier height is high for the direct

path and the barrier width is broad for the indirect path. These analyses qualitatively agree with the present experimental result in Figure 4.15, and are consistent with the calculation by the path integral method [72].

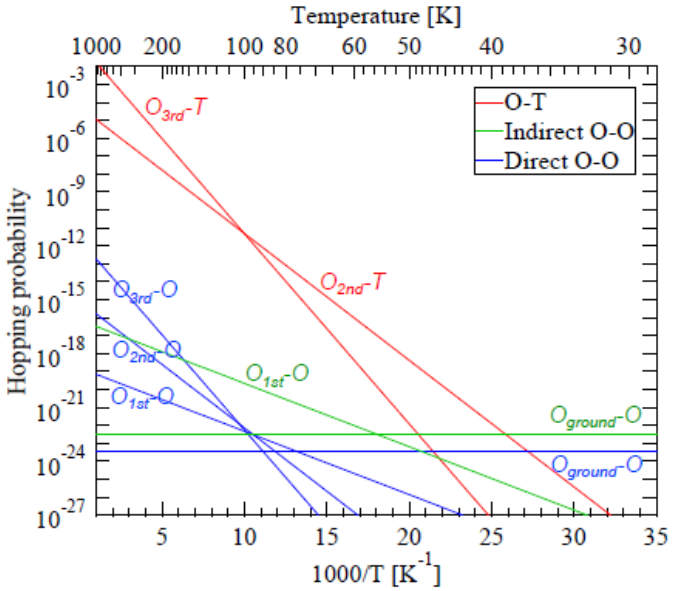

Figure 4.19: Hydrogen hopping probability within the WKB approximation for the O-T, indirect O-O and direct O-O paths in the model potential. The subscript denotes the vibrational level.

Figure 4.20 shows the calculation results of P_n within the WKB approximation for the three paths for D with $E_n = 0.05 \times n$ eV in the O site, which is the value of hydrogen multiplied by $1/\sqrt{2}$. As compared to the substantial contribution of O_{2nd}-T for H, the O_{2nd}-T tunneling of D is not significant, because the $n = 2$ level of D is lower than the level of the T site. Although the $n = 3$ level of D might be sufficiently high for the O_{3rd}-T tunneling to occur as expected by the WKB approximation for D in Figure 4.20, such TE process via $n = 3$ was not observed in the present experiment.

4.2.2.6 Concentration dependence

Figure 4.21 shows the hopping rates and analysis results of PdH(D)$_x$ with larger $x's$. The obtained fit parameters and the contributions to the hopping rate of the OBH, TE and TG processes derived by the fit of Eq. 4.4 for the H(D) hopping rate are shown in Figure 4.22 and Table 4.3. The hopping rate of TG is almost independent of the concentration, and the α in Eq. 4.4 were derived to be 3 regardless of the concentration and the isotopes. In contrast,TE gets suppressed as the H(D) concentration increases. The hopping rates of both H and D are described by OBH and TG with little contribution of TE. The hopping rate of H is found to be substantially suppressed at T = 50-70 K with increasing x and the D hopping rate is only slightly dependent on x. This suppression of the hopping rates in TE comes from the significant decrease in the prefactor ν_2. This seemes to be related to the decrease in E_2. The TE for H via $n = 2$ is suppressed because the $n = 2$ level becomes lower than the T site level, which is similar to the situation where TE of the D hopping is not sufficient. The present analysis reveals a tendency for the activation energy in TE to decrease

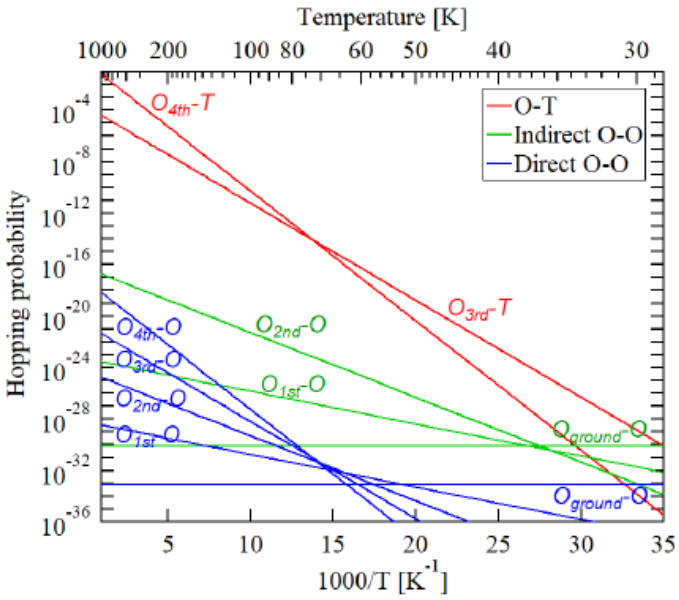

Figure 4.20: Deuterium hopping probability within the WKB approximation for the O-T, indirect O-O and direct O-O paths in the model potential. The subscript denotes the vibrational level.

with increasing x, which is consistent with previous experimental results and DFT calculations showing that the vibrational energy in the O site decreases due to a lattice expansion for larger x [30, 113]. The abrupt transition of H hopping from OBH to TG in PdH_x with large x is similar to the temperature dependence of D hopping. It is worth stating that this abrupt transition from OBH to TG around 70 K is analogous to the case of H hopping via a broad-top barrier, where tunneling around the top of the barrier is substantially suppressed [114]. This similarity supports that the TE process is not included in the H hopping with large x and the D hopping.

4.2.2.7 DFT calculation

To evaluate the hydrogen concentration dependence of the energy levels in O and T sites, we theoretically calculated the energy gains by H atoms incorporated in bulk Pd structures by applying the PHASE code [115]. The calculations are based on density functional theory (DFT) with the generalized gradient approximation (GGA) in the scheme of the Perdew-Burke-Ernzerhof (PBE) [116]. The calculations were performed using projector-augmented wave potentials (PAW) for H and Pd atoms with 64 k points for Brillouin-zone samplings [117]. The cutoff energies are 25 Ry for the wave functions and 196 Ry for the augmented electron densities. The bulk Pd structures are represented by a $(2 \times 2 \times 2)$ unit cell consisting of 32 Pd atoms with periodic boundary conditions. The H atoms were placed randomly in O sites in the bulk Pd, and then the structures were relaxed to be in equilibrium positions in the x-, y- and z-axis directions to find the lowest total energies. Each H atom was aligned with a Pd atom in-between the two second nearest neighbor H atoms. The energy gain E_{gain} is given as

$$E_{\mathrm{gain}} = E(\mathrm{Pd}_{32}) + nE(\mathrm{H}) - E(\mathrm{Pd}_{32} + n\mathrm{H}), \tag{4.5}$$

where E represents a total energy calculated by the DFT.

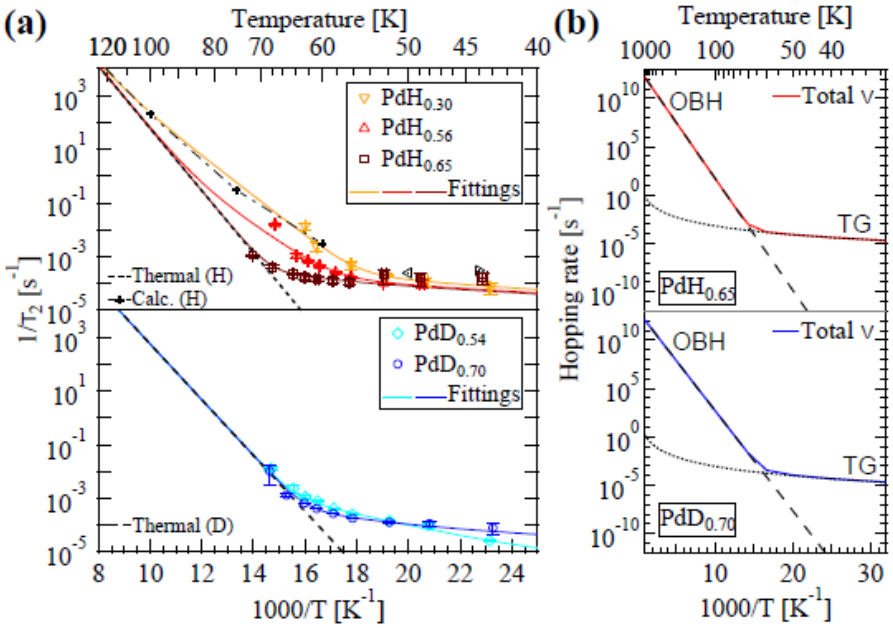

Figure 4.21: (a) Temperature dependence of the H(D) hopping rates in PdH_x and PdD_x with large $x's$ derived from the time evolution of the resistance. (b) Predominant terms of the fit results with Eq. 4.2. for $PdH_{0.65}$ and $PdH_{0.70}$.

Calculation results of the energy gain per H atom ($E_{\rm gain}^{{\rm H}_n{\rm o}}$) and the magnification rate of the lattice constant for $Pd_{32}H_{no}$, where n (=1, 8, 16, 24, 32) H atoms are located at O sites in the unit cell of Pd_{32}, are tabulated in Table 4.1, and the corresponding structures of (a), (b), (c), (d) and (e) are shown in Figure 4.23. The calculation shows that the energy gain increases as the hydrogen concentration is increased and in turn decreases above $n = 16$. The lattice is expanded by the H absorption. According to the Bader charge analysis, which derives the effective valence electron charges sliced at charge nodes between adjacent two atoms, the average charges for H are -1.49, -1.11 and -1.18, and those for the nearest Pd atoms are -10.058, -9.943 and -9.82 for $n = 1, 16$ and 32. This indicates that the coulomb interaction between H and the Pd atoms increases as H increases, which is repulsive for $n = 1$ and attractive for $n = 16$ and 32. Figure 4.24 shows the total density of states for $n = 1$, 16 and 32. The Pd band width is narrowed due to the charge transfer by the hybridization with H and the lattice expansion, resulting in the reduction of Pd-Pd cohesive energy. Therefore, the total energy gain was determined by the competition between the increased H-Pd attraction energy and the reduced Pd-Pd cohesive energy.

The energy gain ($E_{\rm gain}^{{\rm H}_n{\rm o}+{\rm H}_{\rm It}}$) by adding one additional H atom into T site in $Pd_{32}H_{no}$ was calculated as tabulated in Table 4.2. The structures are shown in Figure 4.25. The energy gain is different depending on the position of the T site, and the cases of A and B in Figure 4.25 represent the structures which have relatively large and small energy gains, respectively. The concentration dependence of the energy gain is similar to that in O sites, as it increases below $n = 16$ and decreases above it.

The difference of the energy gain of H in O and T sites ($E_{\rm gain}^{{\rm H}_n{\rm o}} - E_{\rm gain}^{{\rm H}_n{\rm o}+{\rm H}_{\rm It}}$) is shown in Figure 4.26. The difference of the energy gain gets larger above $n = 16$, i.e. the H concentration $x = 0.5$, which

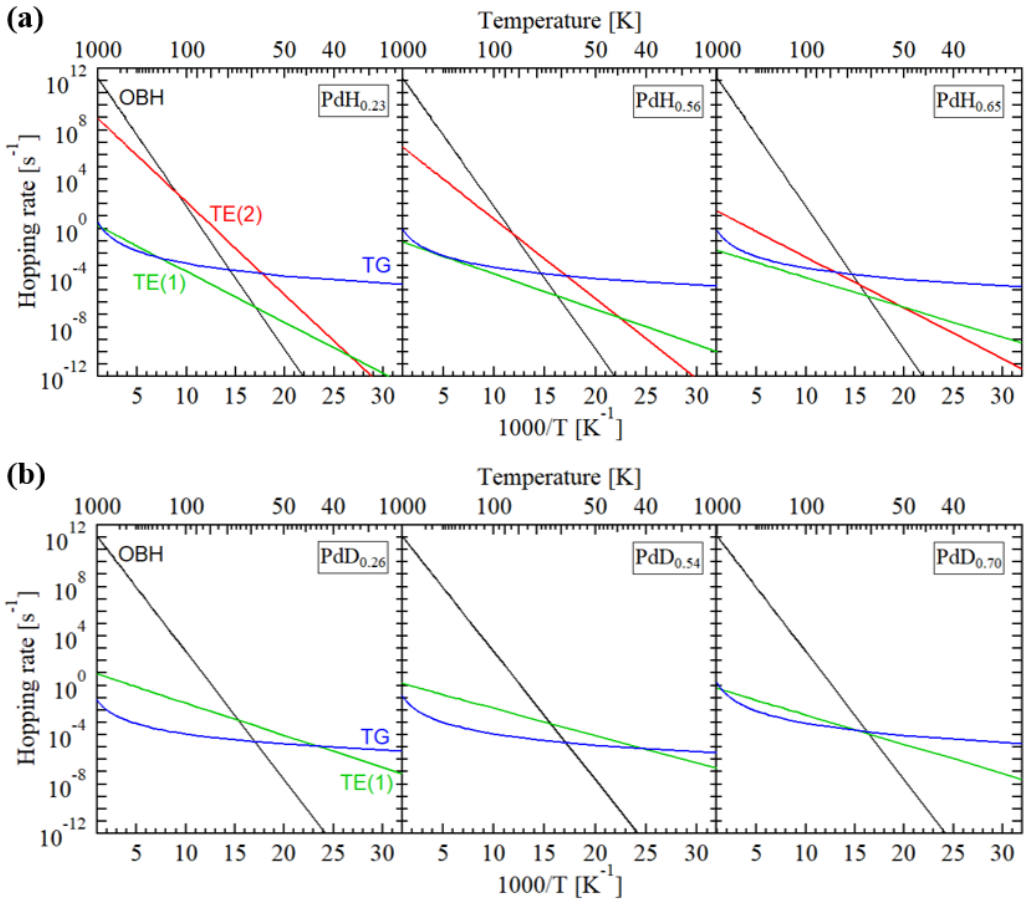

Figure 4.22: Terms of the fit results with Eq. 4.2 for the hopping rates in PdH_x and PdD_x.

	(a) $Pd_{32}H_{1o}$	(b) $Pd_{32}H_{8o}$	(c) $Pd_{32}H_{16o}$	(d) $Pd_{32}H_{24o}$	(e) $Pd_{32}H_{32o}$
Energy gain /H (eV)	2.28	2.54	2.54	2.51	2.46
Magnification rate of lattice constant	1	1.03	1.04	1.05	1.06

Table 4.1: Energy gain per H atom and the magnification rate of the lattice constant for $Pd_{32}H_{no}$ with (a) $n = 1$, (b) $n = 8$, (c) $n = 16$, (b) $n = 24$ and (d) $n = 32$. n H atoms are located in O sites.

means that the energy levels in O sites shift lower than those in T sites. The onset value agrees with the value we experimentally derived of the onset concentration ($x = 0.56$) of the suppression in the H tunneling from the second vibrationally excited state in O the site to the T site. The DFT calculation showed that the suppression of TE is induced by the H absorption is attributed to the energy level mismatching.

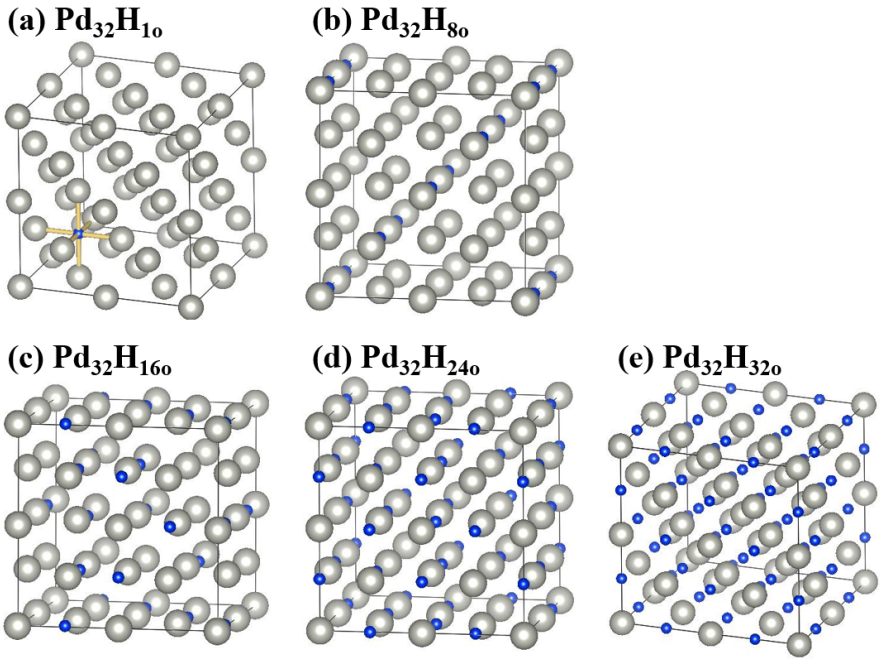

Figure 4.23: Unit cell structures for the DFT calculation of $Pd_{32}H_{no}$ with (a) $n = 1$, (b) $n = 8$, (c) $n = 16$, (b) $n = 24$ and (d) $n = 32$. n H atoms are located in O sites.

4.2.2.8 Hydrogen hopping mechanism between O sites

Figures 4.27 and 4.28 show schematic pictures of the hopping mechanism and path for hydrogen and deuterium, respectively.

At sufficiently high temperature above 100 K, the diffusion of hydrogen and deuterium is governed by OBH, which is consistent with the calculation in the O-T-O path, where the O-T hopping is rate-limiting [72].

At temperature region between 50 and 100 K, the H hopping is dominated by TE via the second vibrationally excited state in the O site in the O-T path with temporal residence at the T site. On

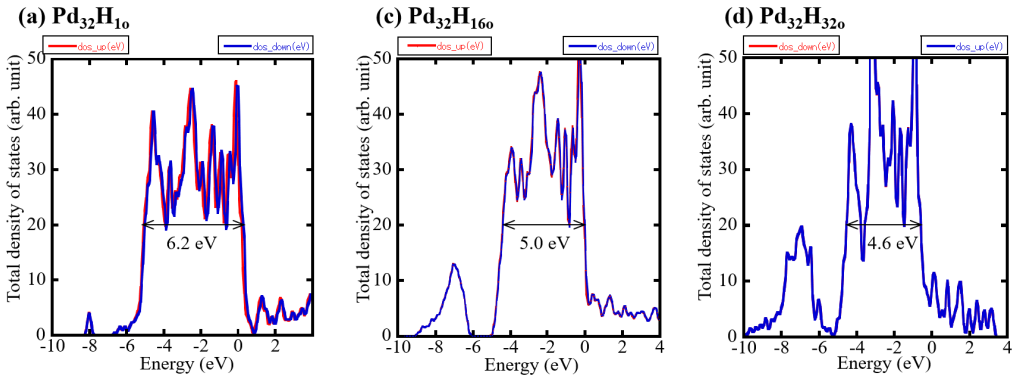

Figure 4.24: The calculated total density of states for $Pd_{32}H_{1o}$, $Pd_{32}H_{16o}$ and $Pd_{32}H_{32o}$.

	(f) $Pd_{32}+H_{1t}$	(g) $Pd_{32}H_{1o}+H_{1t}$	(h) $Pd_{32}H_{8o}+H_{1t}$	(i) $Pd_{32}H_{16o}+H_{1t}$	(j) $Pd_{32}H_{24o}+H_{1t}$	(k) $Pd_{32}H_{32o}+H_{1t}$
Energy gain /H (eV)	2.16	2.05	2.39 (A) 2.25 (B)	2.39 (A) 2.36 (B)	2.09 (A) 1.95 (B)	1.78
Magnification rate of lattice constant	1	1	1.03	1.04	1.05	1.06

Table 4.2: Energy gain by adding one additional H atom into T site in $Pd_{32}H_{no}$ with (f) $n = 0$, (g) $n = 1$, (h) $n = 8$, (i) $n = 16$, (j) $n = 24$ and (k) $n = 32$. n H atoms are located in O sites.

the other hand, as the hydrogen concentration increases, the TE of the H hopping is suppressed. As for deuterium, the TE is substantially small regardless of the concentration. These suppression of TE is attributed to the energy matching between the vibrationally excited states in the O site and the state in the T site. The energy level matching before and after the tunneling is crucial in the TE process. The increased energy mismatching due to the lattice expansion with large x results in the suppression of TE in H hopping. The level of O_{2nd} and O_{3rd} do not match the level of the T site for D, which leads to a small tunneling probability of D. Thus, the TE for H in PdH_x with small x is allowed between the second excited state in the O site to the T site since the energy levels of them are circumstantially close, and this enhancement of hydrogen diffusion is associated with the characteristic potential of Pd where a hollow of the metastable T site is located in a plateau-like potential between the O sites.

Below ~50 K, the hopping of the OBH and TE processes are not significant and dominated by TG. Within the WKB approximation, the tunneling probability of D via either direct or indirect O-O path is over 7 orders of magnitude smaller than that of H. Nevertheless, the hopping rates measured for H and D below 50 K are similar as shown in Figure 4.15. In the tunneling regime, the interaction with surrounding environments such as phonons and electrons makes the hopping rate slightly depend on temperature as mentioned in section 2.1.3. The present experiment reveals temperature dependence of the TG hopping rate with an α of about 3 regardless of isotopes implying the interaction with the surroundings. The value of α, however, is not explained by conventional theories such as one- or two- phonons process or the non-adiabatic effect of electrons. This small isotope effect in TG should be associated with the 50 K anomaly, in which collective motion of hydrogen(deuterium) atoms might be responsible to form an ordered state. Namely, the present result shows a possibility that hydrogen(deuterium) quantum tunneling is affected by the interaction

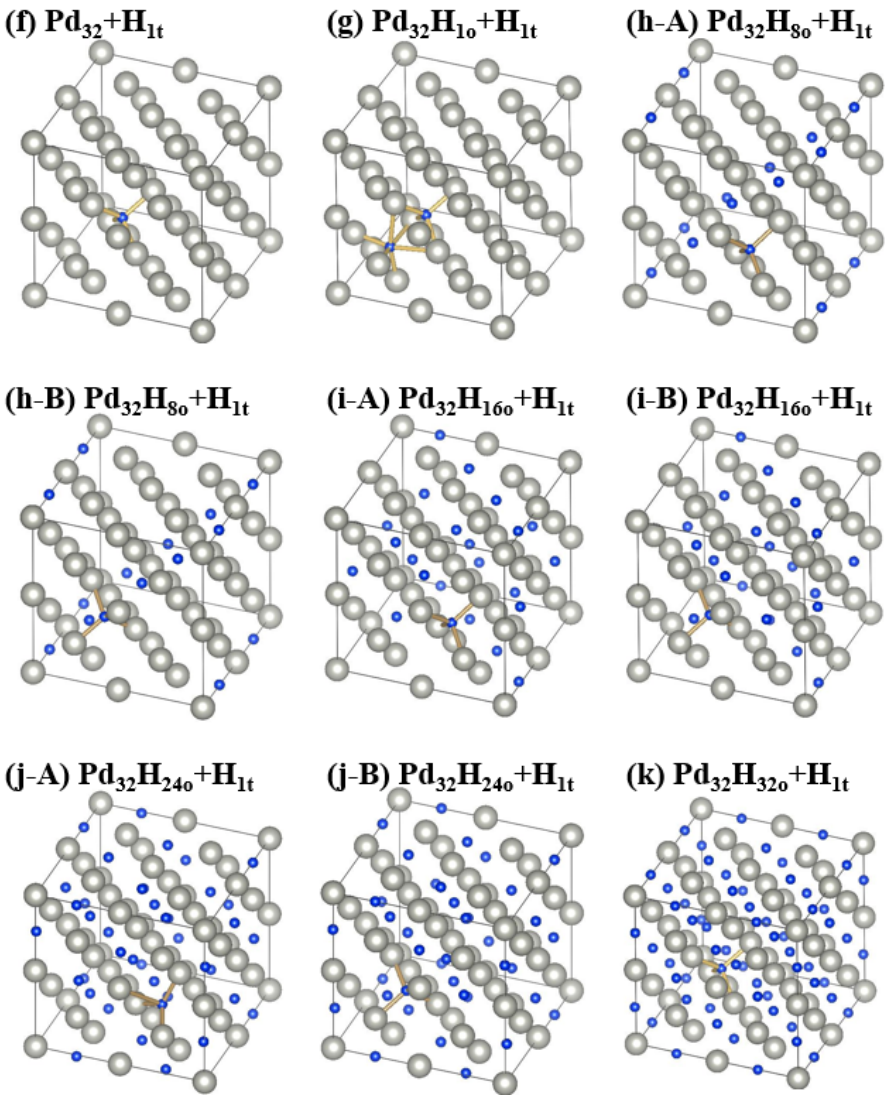

Figure 4.25: Unit cell structures for the DFT calculation of $Pd_{32}H_{no}+H_{1t}$ with (f) $n = 0$, (g) $n = 1$, (h) $n = 8$, (i) $n = 16$, (j) $n = 24$ and (k) $n = 32$. n H atoms are located in O sites and one H atom is in T site. The position of the T site is different in A and B.

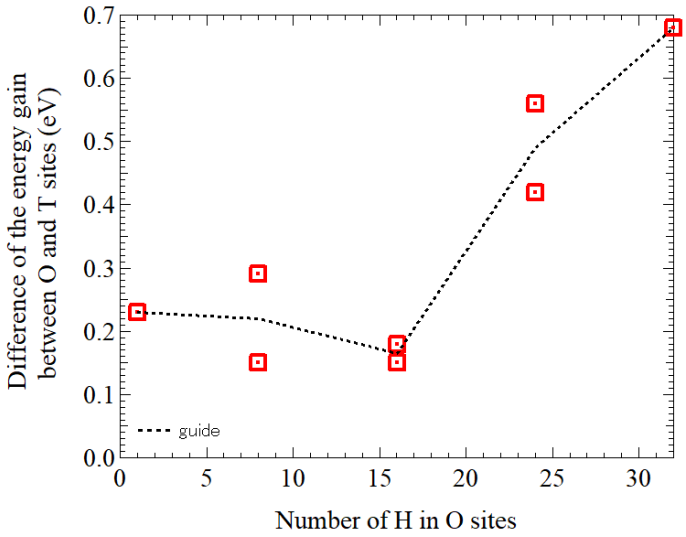

Figure 4.26: The difference of the energy gain of H in O and T sites ($E_{\text{gain}}^{\text{H}_n\text{O}} - E_{\text{gain}}^{\text{H}_n\text{O}+\text{H}_{\text{1t}}}$) according to the number of H atoms in O sites.

between hydrogen(deuterium) atoms.

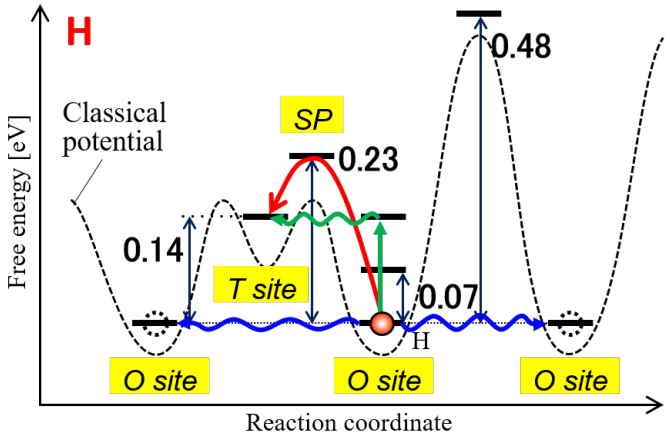

Figure 4.27: Schematic pictures of the hopping mechanism and path for hydrogen in Pd.

4.2.3 Conclusion

Hydrogen(deuterium) hopping in Pd was investigated by the quench-recovery method associated with the 50 K anomaly. We revealed that the hydrogen hopping changes from over-barrier hopping to tunneling from second vibrationally excited state in the O site to the T site below ~100 K, and subsequently to tunneling between the ground states in the O sites below ~50 K in PdH_x with small x. This result indicates that the H hopping in the crossover region between the thermal and quantum regimes sensitively reflects the potential shape including the metastable T site between

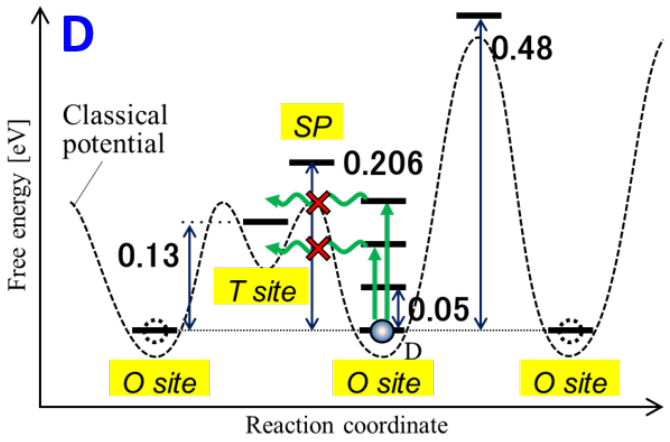

Figure 4.28: Schematic pictures of the hopping mechanism and path for deuterium in Pd.

	TE				TG	
	ν_1 (s^{-1})	E_1 (eV)	ν_2 (s^{-1})	E_2 (eV)	ν_{TG}	α
$PdH_{0.23}$	4.4	0.082	4.8×10^9	0.15	3.1×10^{-10}	3.3
$PdH_{0.30}$	3.1	0.055	4.5×10^9	0.15	2.7×10^{-10}	3.3
$PdH_{0.56}$	0.15	0.057	1.8×10^7	0.13	5.5×10^{-10}	3.1
$PdH_{0.65}$	0.028	0.048	66	0.082	5.8×10^{-10}	3.0
$PdD_{0.26}$	15	0.052	-	-	3.8×10^{-10}	2.7
$PdD_{0.54}$	2.3	0.044	-	-	8.8×10^{-11}	3.1
$PdD_{0.70}$	0.97	0.047	-	-	2.6×10^{-10}	3.3

Table 4.3: Fit parameters in Eq. 4.2 for the hydrogen(deuterium) hopping rates derived by the resistance relaxation in PdH_x and PdD_x. ν_{OBH} and E_a are 2.3×10^{13} s^{-1} and 0.23 eV, respectively.

the adjacent O sites and vibrational states in these sites. TE of H for large x, on the other hand, is suppressed, and TE of the D hopping is not significant irrespective of x. The effect of energy matching on quantum tunneling appears explicitly as the dependence of hydrogen concentration and isotopes observed in the present study, which indicates that the energy matching can be crucial in tunneling between inequivalent sites.

4.3 H ion implantation

4.3.1 Samples

The sample used in this experiment is a 10-nm-thick Pd film deposited on a glass substrate by magnetron sputtering at room temperature. Figure 4.29 shows a glazing incidence XRD pattern for the sample at a grazing angle of 1° with CuKα radiation (λ = 1.5418Å). There are diffraction peaks corresponding to the Pd(111), (200) and (220). Scherrer's equation with the Scherrer constant of 0.9 gives an average grain size of 11.5 nm as obtained from the width of the Pd(111) peak.

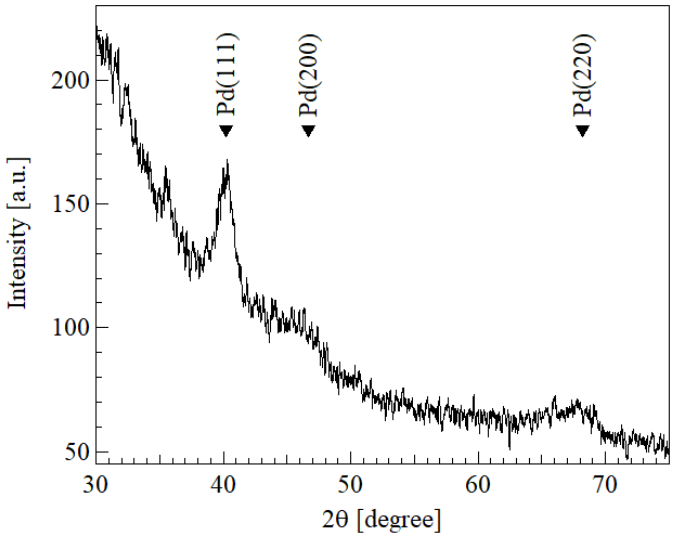

Figure 4.29: Grazing incidence XRD pattern for the 10-nm-thick Pd film on a glass substrate at a glancing angle of 1° with CuKα radiation (λ = 1.5418Å).

4.3.2 Simulation of hydrogen distribution

Figures 4.30 and 4.31 show the simulated distribution of hydrogen atoms and Pd vacancies after hydrogen ions are implanted into a Pd bulk in normal incidence calculated by TRANSPORT OF IONS IN MATTER (TRIM). The implantation energies are assumed between 500 to 3000 eV. As the ion implantation energy increases, the hydrogen distribution is deepened and broadened and the the number of Pd vacancies formed by the implantation is increased. Hydrogen atoms are expected to be distributed between the surface and a depth of ~15 nm and the number of Pd vacancies is derived to smaller than 10^{-10} (Vacancies/cm^3)/(Ions/cm^2) for the hydrogen ion implantation with an energy of 500 eV. Since Pd vacancies affect the hydrogen diffusion as trapping sites for hydrogen atoms, they are desired to be avoided in the study of hydrogen diffusion. Therefore in the present

experiment, the energy of the hydrogen implantation was set as 500 eV, and the 10-nm-thick Pd film was used for hydrogen atoms to be distributed in the whole film.

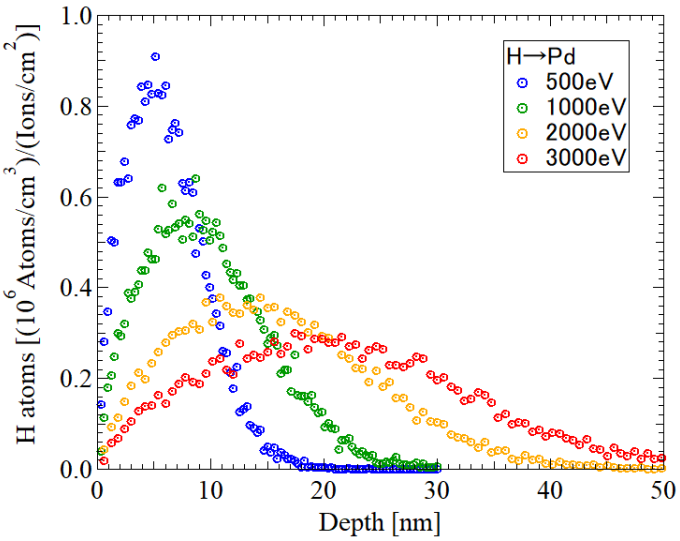

Figure 4.30: Distribution of hydrogen atoms in Pd calculated by TRIM for H^+ implantation with energies from 500 to 3000 eV.

4.3.3 Results and discussion

4.3.3.1 Hydrogenation by hydrogen ion implantation

According to the study of temperature dependence of hydrogen diffusion using the 50 K anomaly in section 4.2, which shows that the over-barrier hopping of hydrogen between O sites is suppressed below ~100 K, metastable states of PdH_x with hydrogen atoms randomly implanted into metastable sites can be effectively frozen at lower temperature. NRA results performed at 105 K for the sample after hydrogen ion implantations with 500 eV in the normal incidence at 105 K are shown in Figure 4.32. The hydrogen signal before the hydrogen implantation around surface is attributed to ice or hydrogen adsorbed on the Pd surface. As the amount of the hydrogen implantation increased, the peak area of NRA got larger. The hydrogen distribution obtained by NRA had a maximum point at ~6 nm from the surface, which is similar to the calculation by TRIM in Figure 4.30. The 10-nm-thick Pd film was confirmed to be hydrogenated by the hydrogen ion implantation as expected by TRIM. The relationship between the hydrogen implantation amount evaluated from the sample charge current and the average hydrogen concentration between 1 to 10 nm derived by NRA is shown in Figure 4.33, where we assumed that the implanted hydrogen ion is in the form of H^+. The similarity of the hydrogen distribution obtained by NRA and the TRIM calculation means that macroscopic hydrogen distribution is almost frozen at 105 K. This is consistent with the result hydrogen diffusion using the 50 K anomaly in section 4.2. The amount of absorbed hydrogen atoms approximately linearly depends on the implantation amount when the implantation amount is below 5 mC/cm^2. Though the amount of absorbed hydrogen is larger than the expectation of TRIM in Figure 4.30, this is possibly because H^{2+} and H^{3+} ions are included in the hydrogen ions source as well as H^+ ions. Although the saturation amount of hydrogen was expected to be x =

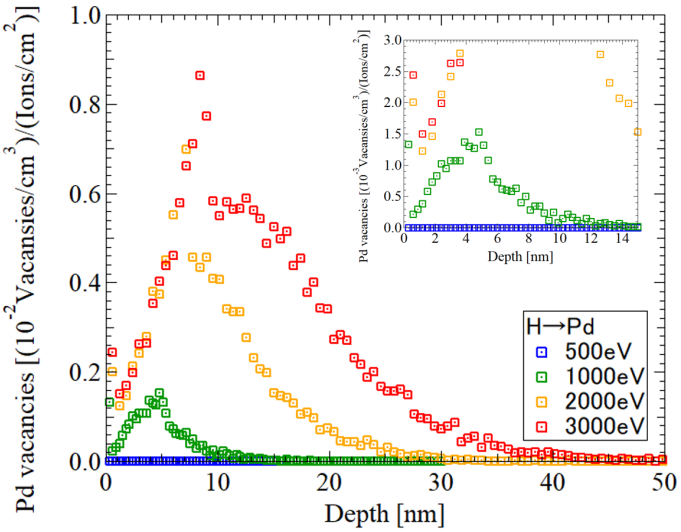

Figure 4.31: Distribution of Pd vacancies in Pd calculated by TRIM for H^+ implantation with energies from 500 to 3000 eV.

1 or more, the absorbed hydrogen was saturated at $x = 0.65$ as shown in Figure 4.33. Since the implantation depth is shallow and near the surface, a part of the implanted hydrogen atoms with some kinetic energies might be easily desorbed.

Figure 4.34 shows the resistance change of the 10-nm-thick Pd film under the hydrogen ion implantation with an energy of 500 eV at 7 K. Note that hydrogen atoms are not absorbed and the resistance does not change by hydrogen gas exposure at 7 K. In contrast to the case of hydrogen gas exposure, the resistance showed a non-monotonous change; as the implantation amount is larger, the resistance increases and subsequently decreases, and increases again. This implies the possibility of formation of a metastable Pd hydride. The results of the simultaneous measurement of resistance and TDS are shown in Figure 4.35 for the sample after the hydrogen implantation with 1 mC. The hydrogen desorption peak in TDS around 50 K comes from the hydrogen molecules physisorbed on the manipulator surface, which has no relation with the sample. The increased resistance by the hydrogen implantation returned to the original value of Pd around 150K, at which the hydrogen desorption was observed similarly to the recovery from the Pd hydrides formed by hydrogen gas dose to Pd. Furthermore, another resistance change was observed below 100 K. Since this change in the resistance was not accompanied with hydrogen desorption and was irreversible for a heating and cooling cycle, it was ascribed to an internal structure change in the PdH_x rather than hydrogen desorption. These results indicate that the hydrogen ion implantation at 7 K forms a metastable state of Pd hydrides, and such a metastable state relaxes at ~80 K.

Here, we consider three possibilities for the internal structure change below 100 K; diffusion of recoiled Pd atoms, hydrogen diffusion in a macroscopic scale, and microscopic hydrogen hopping between inequivalent sites. We firstly discuss the Pd vacancy diffusion. The number of Pd vacancy caused by the hydrogen implantation with 500 eV is numerically zero by TRIM calculations. Even if some vacancies were formed, the vacancy migration energy of Pd was calculated to be larger than ~1.4 eV, which was sufficiently large for the recoiled Pd atoms to be frozen at such a low temperature region [110]. Furthermore, because the present experiment shows that the increased resistance of PdH_x by the hydrogen implantation returned to the original value after heating up to

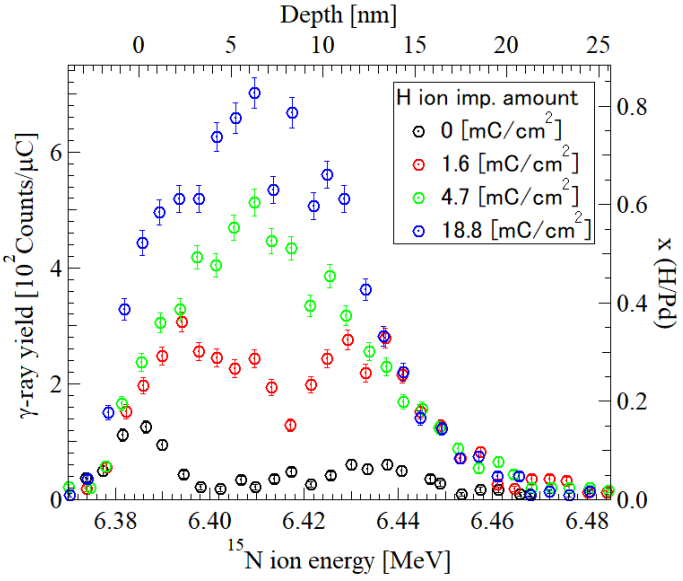

Figure 4.32: Hydrogen distribution obtained by NRA at 105 K for the 10-nm-thick Pd film on a glass substrate after the hydrogen ion implantations.

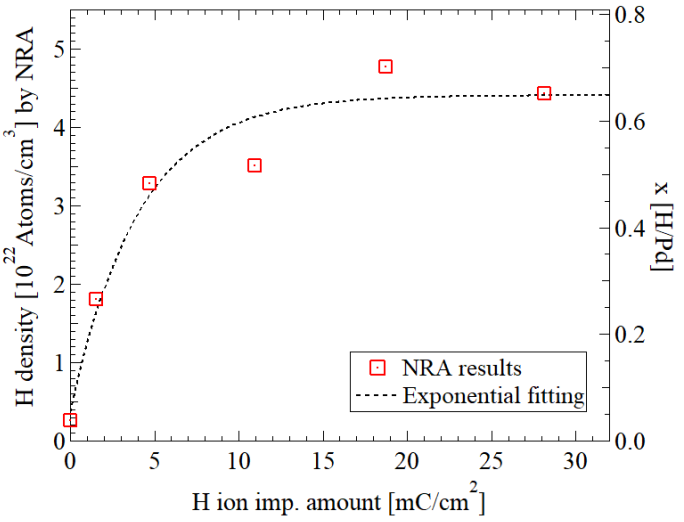

Figure 4.33: Relationship between the amount of hydrogen ion implantation evaluated from the charge current and the average hydrogen concentration between 1 to 10 nm derived from NRA.

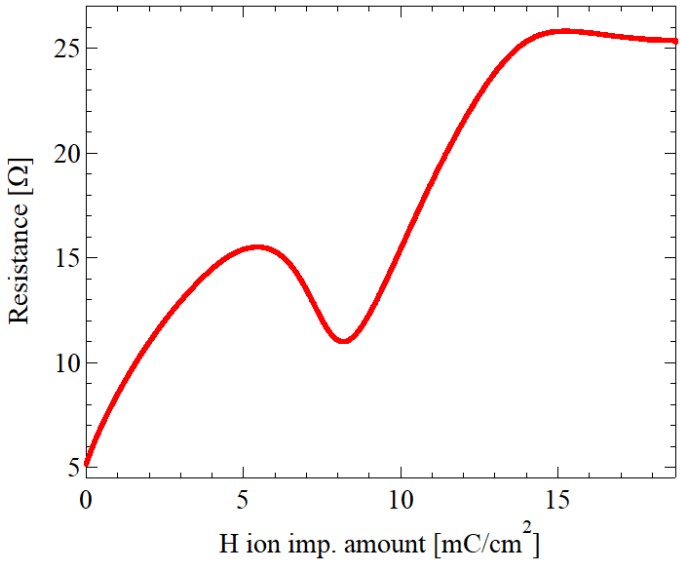

Figure 4.34: Resistance change of the 10-nm-thick Pd film on a glass substrate under the hydrogen ion implantation with a energy of 500 eV at 7 K.

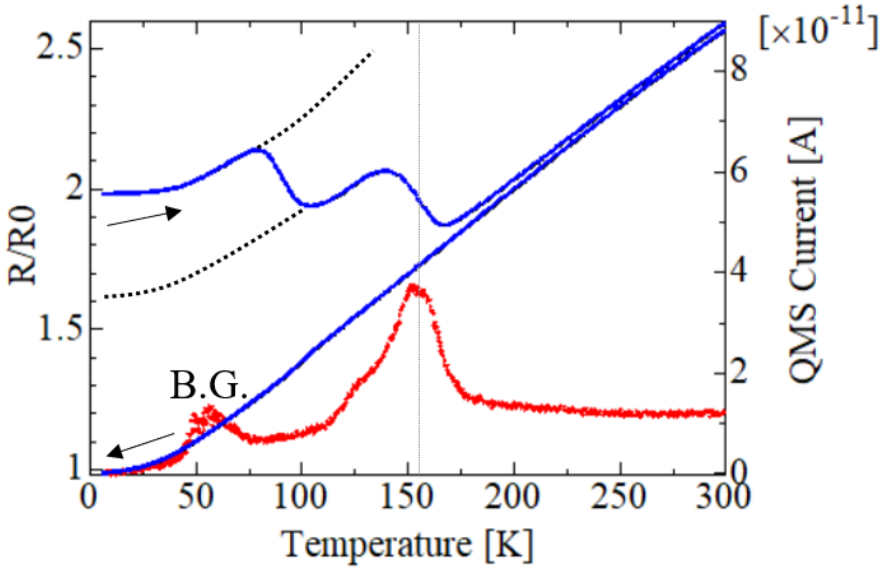

Figure 4.35: Simultaneous measurement of resistance and TDS of the 10-nm-thick Pd film on a glass substrate with a heating rate of 0.8 K/s after the hydrogen ion implantation with 1 mC at 7 K.

380 K, the damage on Pd lattice such as a sputtering effect is negligible. Thus, we can conceive that the resistance change below 100 K is not related to the diffusion of Pd vacancies formed by the hydrogen implantation. Secondly, we discuss the possibility of macroscopic hydrogen diffusion. Macroscopic hydrogen diffusion below 100 K is, however, ruled out by comparing the TRIM calculation with the NRA result. The hydrogen distribution of NRA at 105 K is similar to the calculation of the TRIM, which means that macroscopic hydrogen distribution is conserved below 105 K. If an ununiform distribution of hydrogen atoms formed by the hydrogen implantation becomes uniform, the resistance should increase assuming that the resistance of PdH_x almost linearly depends on the hydrogen concentration, and that the electronic conduction path of the Pd film should be parallel to the surface from the requirement of the terminal arrangement. In the experiment, however, the resistance decreased. Phase separation of PdH_x is also excluded because the resistance change was observed below ~50 K. The phase separation of hydrides should include long-range diffusion of hydrogen atoms. In the experiment of the 50 K anomaly, nevertheless, the hydrogen hopping between neighboring O sites is significantly suppressed below 100 K. Hence, it is quite reasonable to assume that the change in the resistance below 100 K is caused by a local hopping of hydrogen atoms between inequivalent states.

As will be mentioned in section 6.1 in detail, structure analysis was performed by channeling NRA, which can determine the hydrogen lattice location in single crystals. The results show that a part of the implanted hydrogen atoms are located in the metastable T site, and that they diffuse to the stable O site by heating up to 80 K. Therefore, the change in the resistance observed below 100 K for the PdH_x formed by hydrogen ion implantation is caused by the hydrogen hopping between inequivalent sites, i.e. from T to O sites.

Figure 4.36 shows the temperature dependence of the resistance of the PdH_x during cooling after the hydrogen ion implantation with the amount of 6 mC at 7 K followed by heating to 89 K. Interestingly, the 50 K anomaly does not appear below 100 K in this metastable Pd hydride formed by the hydrogen implantation. The 50 K anomaly is the phenomenon related to ordering of hydrogen atoms in the O sites of the Pd [86, 87]. The metastable PdH_x formed by the implantation has hydrogen atoms in the T site as well as in the O site, implying that the hydrogen in the T site suppresses the 50 K anomaly. This might be valuable knowledge to elucidate the 50 K anomaly. Figure 4.37 shows the temperature dependence of the resistance after the subsequent heating up to 119 K for the PdH_x formed by the implantation. The 50 K anomaly appearers after the heating. This indicates that the change of the lattice location of hydrogen atoms from the metastable T site to the stable O site contributes to the appearance of the 50 K anomaly. These results experimentally revealed that the 50 K anomaly is a phenomenon strongly related to the hydrogen location and state.

4.3.3.2 Relaxation of resistance

We measured the time evolution of the resistance of the 10-nm-thick Pd film at various temperatures between 6 to 80 K after the hydrogen or deuterium ion implantation of 1 mC at 7K. Figures 4.38 and 4.39 show the resistance changes at 80 K and 6 K after the implantation at 7 K, respectively [118]. There is a large isotope effect on the resistance change at 6 K. Whereas the relaxation of the resistance was observed for hydrogen at all temperatures, the samples to which deuterium ions were implanted did not show relaxation of the resistance below 50 K. The time evolution of the resistance $R(t)$ is described with an exponential function with the time constant τ_1 as

$$R(t) = R_1 \exp(\frac{-t}{\tau_1}) + C, \tag{4.6}$$

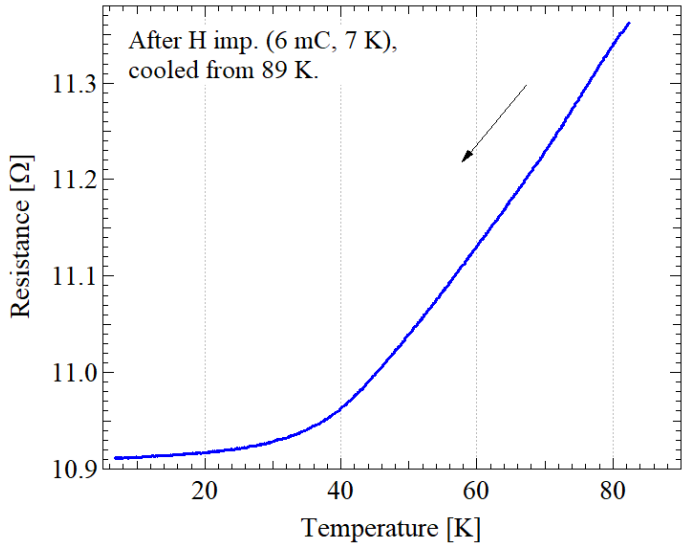

Figure 4.36: Temperature dependence of resistance of the 10-nm-thick Pd film on a glass substrate after the hydrogenation with 6 mC at 7 K.

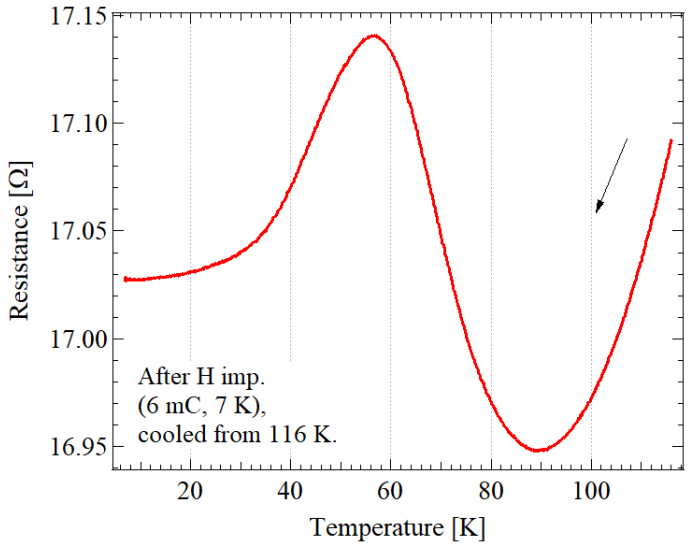

Figure 4.37: Temperature dependence of resistance of the 10-nm-thick Pd film on a glass substrate after the hydrogenation with 6 mC at 7 K followed by heating up to 120 K.

where R_1 and C are constants. The resistance changes were well fitted by Eq. 4.6 after the temperature was stabilized. τ_1^{-1} represents the hydrogen(deuterium) hopping rate from the T to O sites assuming that the resistance change linearly reflects the number of hydrogen hopping. The temperature dependence of hydrogen(deuterium) hopping rate is obtained by analyzing the relaxation rate of the resistance at various temperatures.

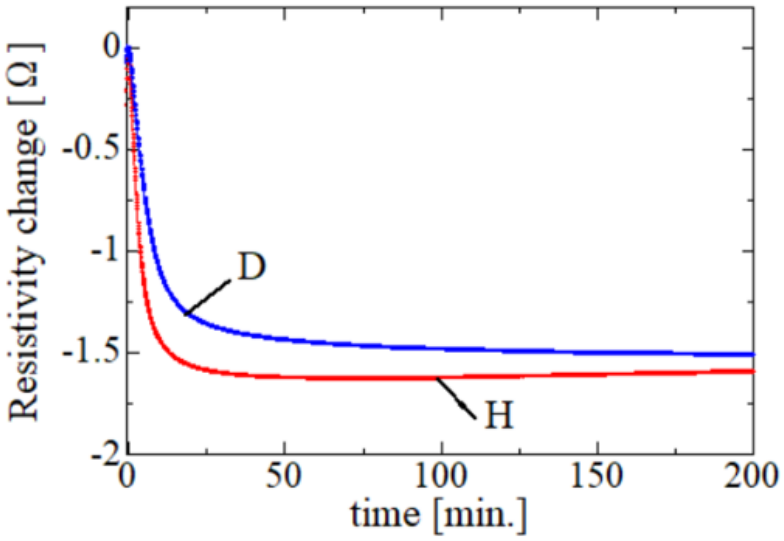

Figure 4.38: Resistance change of the 10-nm-thick Pd film on a glass substrate at 80 K after the hydrogen ion implantation with 1 mC and 500 eV at 7 K.

Figure 4.40 shows the temperature dependence of the hydrogen and deuterium hopping rates derived from the relaxation of resistance after the hydrogen(deuterium) ion implantation with an amount of 1 mC at 7K. The hopping rates of both hydrogen and deuterium similarly depend on the temperature strongly above 60 K. While the hydrogen hopping was still observed below ~50 K, the deuterium hopping was substantially suppressed. As can been seen in Figure 4.40 , the hydrogen hopping rate is almost independent of temperature below 30 K. Here we emphasize that the observed hydrogen(deuterium) hopping is from the T to O sites.

4.3.3.3 Hydrogen hopping mechanism from T to O sites

From a one-dimensional WKB approximation, the tunneling probability is expected to strongly depend on mass as given by Eq. 4.4. Thus, the large isotope effect observed in the hopping rates below ~50 K is a convincing evidence of quantum tunneling. Looking at the temperature dependence of the hydrogen hopping carefully, the hydrogen hopping rate takes a minimum around 20 K as shown in Figure 4.41. We discuss the hydrogen hopping in the temperature regions below and above 20 K in terms of electron- and phonon- mediated tunneling, respectively.

Non-adiabatic effect of electrons at low temperature

Below 20K, the hydrogen hopping rate slightly increased with decreasing temperature. This temperature dependence agrees with Kondo's prediction about the non-adiabatic effect of electrons; the tunneling of light particles is enhanced at low temperature [2, 37]. The temperature dependence

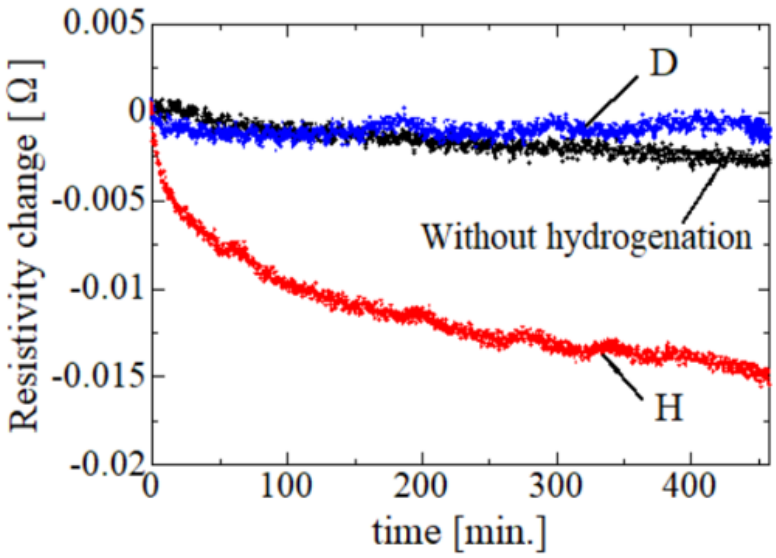

Figure 4.39: Resistance change of the 10-nm-thick Pd film on a glass substrate at 6 K after the hydrogen ion implantation with 1 mC and 500 eV at 7 K.

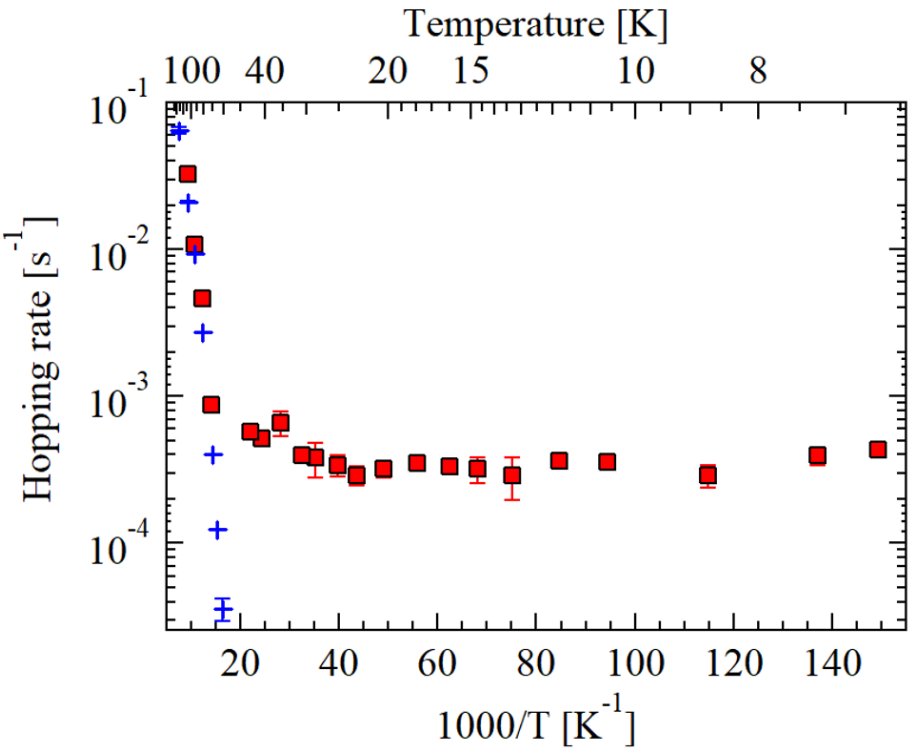

Figure 4.40: Hydrogen and deuterium hopping rates derived from the resistance relaxation of the 10-nm-thick Pd film on a glass substrate after the hydrogen(deuterium) implantation with 1 mC and 500 eV at 7 K.

of the hydrogen hopping rate (ν) governed by the non-adiabatic effect is described as $\nu \propto T^{2K-1}$, where $2K-1$ is expected to has a negative value for a particle with one positive charge. Thus the hopping rate is expected to get larger with decreasing temperature. The fit with a function of T^{2K-1} is shown by the solid line in Figure 4.41. The electron-particle coupling constant K was derived to be 0.41, which is consistent with the theoretical prediction by Yamada that K must be between 0 and 0.5 in fcc metals [37].

The electron-particle coupling constant K which represents the non-adiabatic effect of electrons is controversial because of the lack of experimental data. So far K has been derived to be 0.22 for for muon in Cu, and 0.32 for muon in Al by μSR [40, 41, 42, 43, 44, 5], and 0.25 for hydrogen on Cu by STM [8]. The derived K in the present experiment for hydrogen hopping from the T to O sites in Pd is larger as compared to those values.

Here in general, considering spin degeneracy, when a local potential is screened by the electrons with $l = l_0$, the coupling constant K_{l_0} is given as

$$K_{l_0} = 2(2l_0 + 1)K_0(x, \delta_{l_0}), \tag{4.7}$$

where δ is a phase shift due to the complete screening of the nuclear charge Z. If we assume the screening by the electrons with s-symmetry without spin degeneracy, $K_0(x, \delta)$ is expressed using the spherical Bessel function of zero order j_0 and hopping distance a as [37]

$$K_0(x, \delta) = \left(\frac{1}{\pi}\tan^{-1}\left[\frac{\sqrt{1-x}\tan\delta_l}{\sqrt{(1+x)\tan^2\delta_l}}\right]\right)^2 \tag{4.8}$$

$$x = j_0^2(k_F a). \tag{4.9}$$

The phase shift δ_l obeys the Friedel sum rule as

$$\frac{2}{\pi}\sum_l (2l+1)\delta_l = Z. \tag{4.10}$$

The coupling constant K_{l_0} is determined by k_F and a, which depend on host materials. If the elections have s-symmetry ($l = 0$) and the charge of the particle Z is 1, δ becomes $\frac{\pi}{2}$. Figure 4.42 shows $K_0(x, \delta)$ as functions of δ and $(k_F a)^{-1}$ calculated by Yamada [37]. As $(k_F a)^{-1}$ decreases, K_0 tends to increase. Since the hopping in the present experiment is between T and O sites in Pd, the hopping distance is smaller than that between O sites in previous studies for Cu and Al. Nevertheless, the derived coupling constant K in Pd is larger than those for Cu and Al. This might be related to the contribution of plane waves with $l \neq 0$. As Eq. 4.7 shows, the contribution of $l \neq 0$ can make K_{l_0} larger. In the present case, however, since electrons are scattered by protons, the contribution of plane waves with $l \neq 0$ is expected to be small. We speculate that this inconsistency originates from the assumption that the conduction electron is a free electron. The large value of K in Pd is possibly related to the band structure characteristic to Pd, which has the large density of states of electrons due to the 4d orbitals with effectively large mass around the Fermi level. This is different from simple metals in which the conduction electron are composed of sp-electrons such as Al and Cu. Thus, the large K derived in Pd might reflect the characteristic band structure of Pd. Furthermore, it should be mentioned that hydrogen tunneling occurs between inequivalent sites from T to O sites in the present experiment. An asymmetry potential between the T and O sites might be also important for the coupling constant K [119]. Further experimental information of the coupling constant K in a variety of metals is needed to clarify the the non-adiabatic effect of

electrons in hydrogen quantum tunneling.

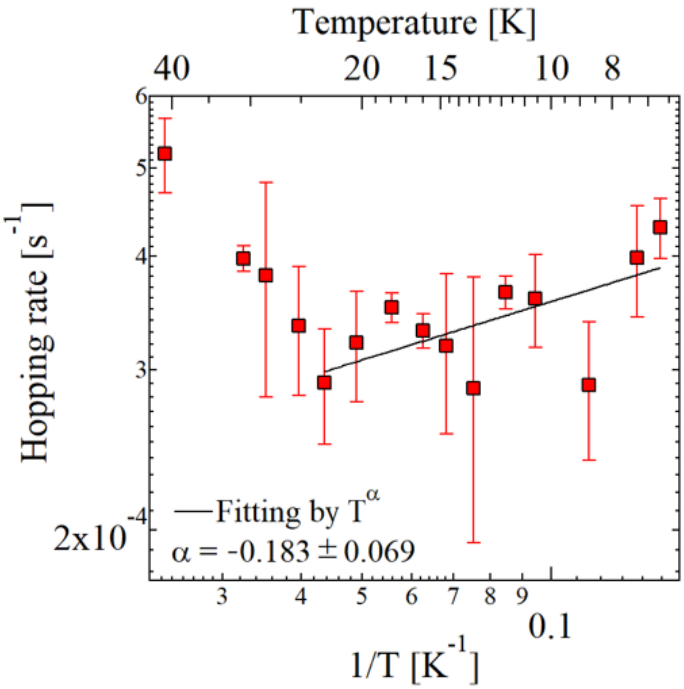

Figure 4.41: Hydrogen hopping rates at low temperature in the 10-nm-thick Pd film on a glass substrate after the hydrogen ion implantation.

Phonon-assisted tunneling

In the temperature region between 20 to 50 K, the hydrogen hopping rate obeyed the Arrhenius law while deuterium hopping was still suppressed as shown in Figure 4.43. This implies that diffusion of hydrogen(deuterium) in this temperature region includes a thermal process with a quantum nature kept. Apparent activation energy derived from the slope of the temperature dependence of the hydrogen hopping was 3.1 meV. Since this activation energy is too small to excite the hydrogen atom to vibrationally excited states, this diffusion is different from the diffusion process of tunneling via the vibrationally excited states. This process corresponds to what is called phonon-assisted tunneling, where the interaction with phonons promotes the tunneling diffusion. The phonons help the energy levels of hydrogen before and after the tunneling to coincide with. The energy coincidence results in increase in tunneling probability. The phonon-assisted tunneling is expected to be allowed around the crossover temperature between quantum and thermal regimes, and can be crucial for tunneling where energies in the initial and final states are slightly different because of the lattice distortion or tunneling between inequivalent sites [34, 33, 34, 35]. The result in section 4.2 that the tunneling from the second excited states in the O site to the T site is allowed for hydrogen shows that the energy level mismatch between them is small. Thus, it is reasonable to conceive that the small activation energy derived here corresponds to the coincidence energy between the second excited states in the O site and the ground state in the T site.

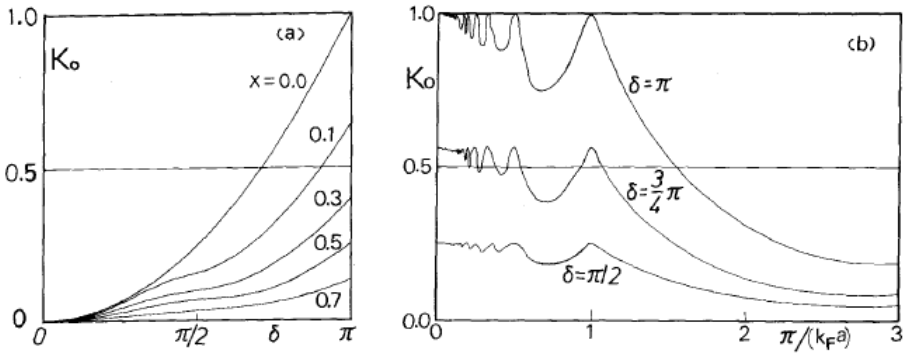

Figure 4.42: $K_0(x, \delta)$ as functions of δ and $(k_F a)^{-1}$ calculated by Yamada [37].

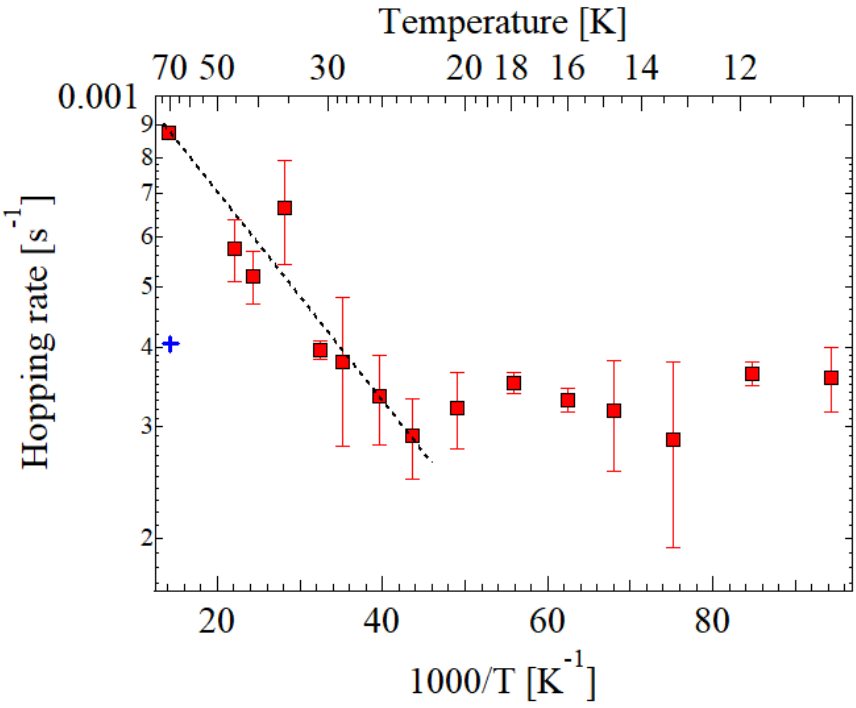

Figure 4.43: Hydrogen hopping rates at low temperature in the 10-nm-thick Pd film on a glass substrate after the hydrogen ion implantation.

Isotope effects in thermal hopping at high temperature

Above 50 K, the hopping rates of both hydrogen and deuterium from the T to O sites obeyed the Arrhenius law as described by dashed lines in Figure 4.44. Since the hopping rates of the isotopes were similar, the hopping process of hydrogen and deuterium above 50 K is governed by a thermal process rather than quantum tunneling. the activation energies derived by the slopes of the hopping rates were 64.1 meV and 72.3 meV for hydrogen and deuterium, respectively. According to the transition state theory, the activation energy for thermal reaction corresponds to the difference of the energy levels between the initial and transition states. The free energy profile in Pd calculated by Kimizuka using the ab initio path integral method shows that the energy difference of the T site and the transition state is 0.061 eV for protium and 0.091 eV for tritium at 60 K. These values and the mass dependence are in good agreement with our results, which supports that the diffusion path observed in the present study is that from T to O sites.

The difference in the activation energies between the isotopes gives information about the shape of the energy potential. The thermal hopping reflects the quantum nature of hydrogen as a zero-point vibration. When a particle with mass m is located in a one-dimensional harmonic potential with a curvature k, the zero-point energy E_0 is expressed as

$$E_0 = \frac{\hbar}{2}\sqrt{\frac{k}{m}}. \tag{4.11}$$

The larger the potential curvature is, the larger the zero-point energy of particles in the potential. Since the derived activation energy was smaller for hydrogen than deuterium, the potential of the initial site is sharper than that of transition state between the T and O sites, as schematically shown in Figure 4.45 This knowledge about the potential curvature of the T site and saddle point is obtained thanks to the hydrogen hopping from the T to O sites. This is also consistent with the theoretical calculation showing that the zero-point energy is larger at the transition site than that at the T site [72]. In contrast, previous experimental studies for hydrogen diffusion between O sites in the Pd bulk revealed that the activation energy corresponding to the energy difference between the O site and the transition state is larger for hydrogen than that for deuterium. This implies that the potential around the O site is wider than that around the transition state. Therefore, the order of the potential curvature is concluded to be at T site, transition state and O site as schematically shown in Figure 4.45.

4.3.4 Conclusion

We successfully observed the hydrogen diffusion from the metastable T to the stable O sites in Pd by resistance measurements combined with H ion implantation. The hopping rates of both hydrogen and deuterium obeys the Arrhenius law above 60 K. While the deuterium hopping was substantially suppressed below ~50 K, the hydrogen hopping was still observed. The temperature dependence and isotope effect on the hopping rates revealed that hydrogen diffuses thermally above 50 K, via phonon-assisted tunneling between 20 to 50 K, and via tunneling below 20 K. The temperature dependence of the hydrogen hopping rate below 20 K is expressed by the Konto theory, which takes into account the non-adiabatic effect of electrons, and the electron-particle coupling constant K was derived to be 0.41. Furthermore, the activation energies of thermal hopping process for hydrogen and deuterium from the T to O sites was derived to be of 64.1 meV and 72.3 meV, respectively. This revealed that potential curvature is larger at the T site than that at the saddle point between the T and O sites.

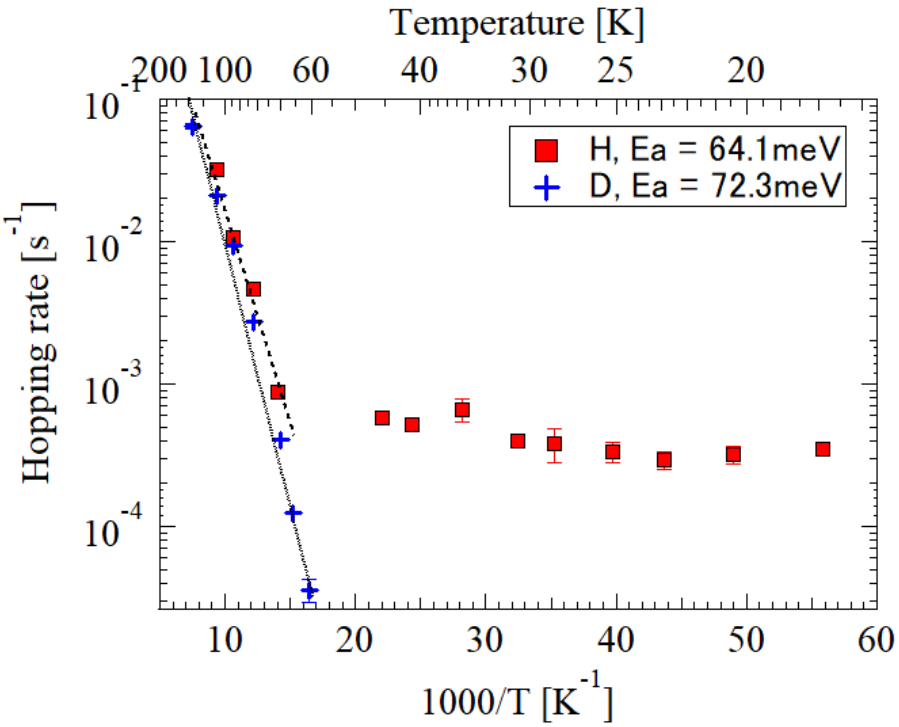

Figure 4.44: Hydrogen hopping rates at high temperature in the 10-nm-thick Pd film on a glass substrate after the hydrogen ion implantation.

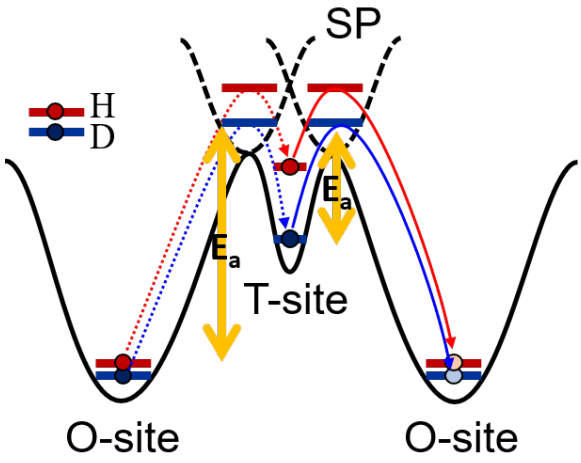

Figure 4.45: Schematic picture of H(D) thermal hopping including zero-point energies and potentials at O, T and saddle point in Pd.

Chapter 5

Resistance minimum in palladium hydrides

Absorbed and/or adsorbed hydrogen atoms possibly modulate physical properties of host materials as a cation or anion and also as a scattering impurity. In this section, the electronic transport, namely the electronic properties, of Pd hydrides is investigated. To elucidate the size and/or surface effects on hydrogen absorption and electronic properties, thickness dependence was evaluated by performing electrical resistance measurements for 50, 5 and 2-nm-thick Pd films. A resistance minimum phenomenon was observed after hydrogen absorption in all samples. A resistance minimum was also observed in the 2-nm-thick Pd film even before the hydrogenation. The origins of these phenomena are discussed in terms of the Kondo effect and the Anderson localization.

5.1 Samples

Three kinds of Pd films with thicknesses of 50, 5 and 2 nm were deposited by magnetron sputtering at room temperature. Crystallinity of the films was characterized by XRD with CuKα ($\lambda = 1.5418nm$).The two-dimensional XRD pattern and its corresponding θ-2θ diffraction pattern for a 50-nm-thick Pd film on the $SrTiO_3$(100) substrate are given in Figures 4.3 and 4.4 in section 4.2, which confirmed that the deposited Pd film is polycrystalline. The average grain size derived from the Pd(111) ring is 42.3 nm from Scherrer's equation with the Scherrer constant of 0.9.

Figure 5.1 shows θ-2θ XRD patterns for the 5-nm-thick Pd film on a glass substrate and the glass substrate without Pd films. The difference of the XRD pattern of the glass substrate from the XRD pattern of Pd(5nm)/glass is also displayed. The diffraction peaks of Pd(111) and (200) were observed, indicating that the deposited 5-nm-thick Pd film is polycrystalline. The average grain size is derived to 10.4 nm from the width of Pd(111) peak.

The θ-2θ XRD patterns for the 2-nm-thick Pd film on glass substrate and a glass substrate are shown in Figure 5.2. The difference of the XRD pattern of glass substrate from the XRD pattern of Pd(2nm)/glass substrate is also shown. The diffraction peak which is considered to correspond to Pd(111) was observed though it is weak. The growth of Pd crystals was confirmed.

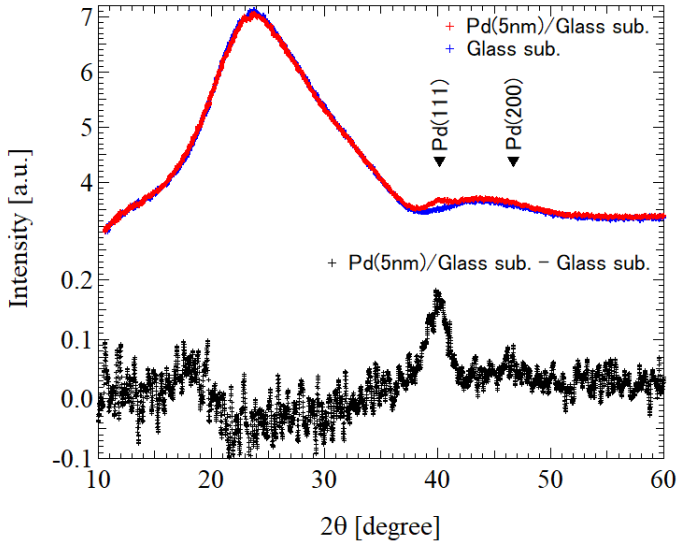

Figure 5.1: θ-2θ XRD patterns for the 5-nm-thick Pd film on glass substrate and a glass substrate. Difference of them is also shown.

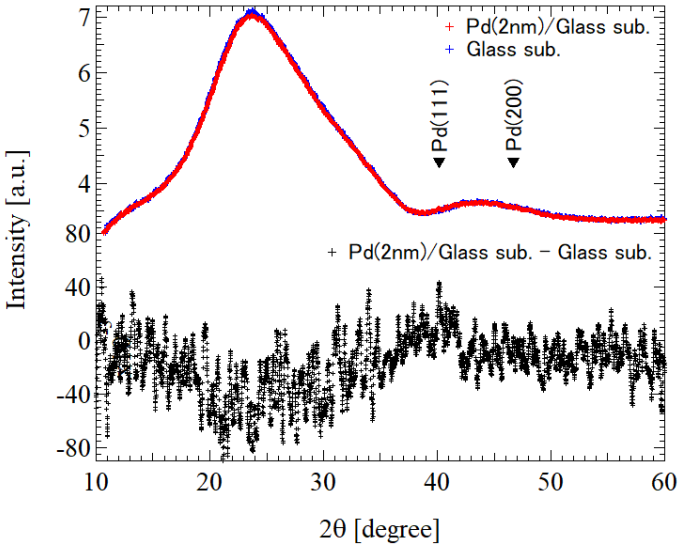

Figure 5.2: θ-2θ XRD patterns for the 2-nm-thick Pd film on glass substrate and a glass substrate. Difference of them is also shown.

5.2 Results and discussion

5.2.1 50-nm-thick palladium hydrides

5.2.1.1 Hydrogenation by H_2 gas exposure

Hydrogenation of 50-nm-thick Pd films was performed by the H_2 gas exposure at 200 K as mentioned in section 4.2 about hydrogen diffusion of the 50 K anomaly. The result of the simultaneous measurement of resistance and TDS, and the relationship between the gas pressure and concentration are given in Figure 4.6 and Figure 4.8 in section 4.2, respectively. Formation of α, (α+β) and β phases of PdH_x depending on the gas pressure is confirmed.

5.2.1.2 Temperature dependence of resistance

Figure 5.3 shows the temperature dependence of the resistance at low temperature during cooling for various $x's$. As can been seen, the pure Pd demonstrated that the resistance linearly depends on temperature toward the residual resistance at low temperature, which is a typical temperature dependence of normal metals. As hydrogen concentration x increased, the resistance increased and a hump in the resistance appeared around 70 K corresponding to the 50 K anomaly as clearly shown by $-dR/dT$ in Figure 5.4, where the change in $-dR/dT$ observed around 110 K regardless of the samples might be related to the structural phase transition in the $SrTiO_3$ substrate. Looking at the lower temperature region, a resistance minimum was observed around 20 K for PdH_x with $x \geq 0.23$, whose onset concentration corresponds to the onset of the (α+β) phases as compared to the diagram in Figure 4.8. The temperature of the resistance minimum increased with increasing x. This phenomenon has not been observed in previous studies.

Figure 5.5 shows the resistance of $PdH_{0.56}$ during cooling with various rates from -0.02 to -2 K/s. The hump of the 50 K anomaly was suppressed with rapid cooling, which is consistent with the fact that the 50 K anomaly is associated with the hydrogen diffusion. Thinking in the same way, if the resistance minimum observed around 20 K were related to a phase transition, the temperature and intensity of the phenomenon would depend on the cooling rate. As can been seen in figure 5.5, however, the resistance minimum phenomenon is almost independent of the cooling rate. This denies that the resistance minimum phenomenon is caused by a phase transition induced by hydrogen diffusion in PdH_x.

Similarly, the resistance minimum was also observed for the PdD_x. The onset deuterium concentration almost corresponds to the onset of the (α+β) phases as PdH_x.

5.2.1.3 Analysis in terms of the Kondo effect

We discuss the origin of the resistance minimum phenomenon observed in PdH_x around 20 K. Speaking of a phenomenon of resistance minimum, a resistance minimum in metals with dilute magnetic impurities such as Fe and Mn is famous. This has been theoretically clarified as the Kondo effect, which describes the scattering of conduction electrons due to magnetic impurities. As mentioned in section 2.2, the temperature-dependent resistance ($R(T)$) of transition metals in the presence of magnetic impurities is expressed as

$$R(T) = R_0 + R_1 T^2 + R_2 T^5 - cR_3 \ln T, \tag{5.1}$$

where c is the concentration of magnetic impurities [46, 47, 50]. The first term is the residual resistance, and the second and third terms represent the contributions of the electron-electron inter-

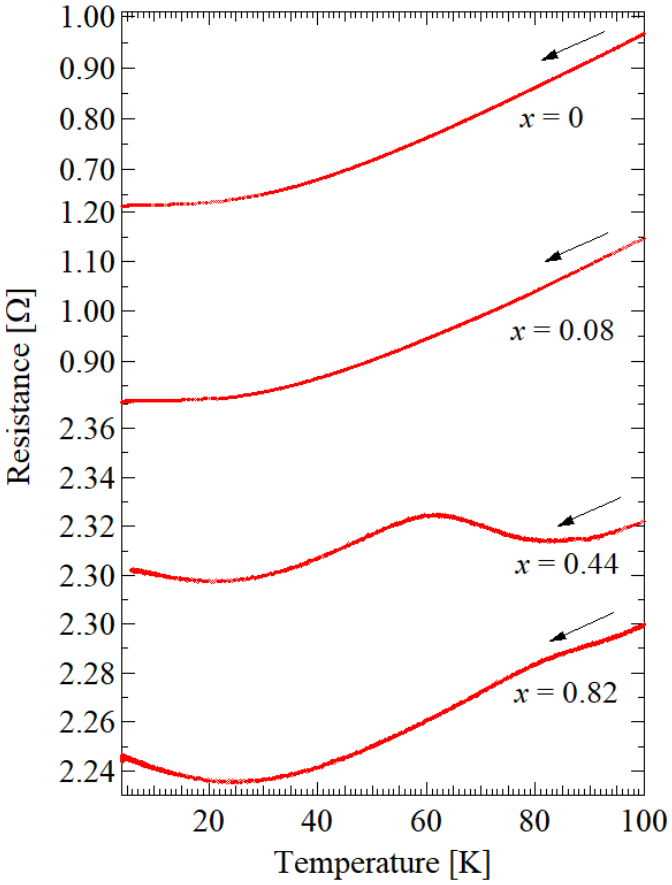

Figure 5.3: The temperature dependence of the resistance of the 50-nm-thick PdH_x film with various $x's$ around 100 K.

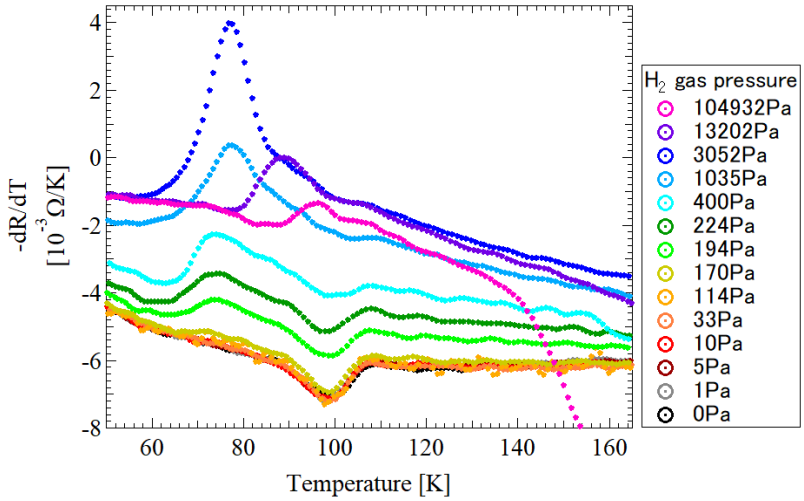

Figure 5.4: The temperature differential of the resistance in heating of the 50-nm-thick PdH_x film hydrogenated by the gas exposure with various pressures at 200 K.

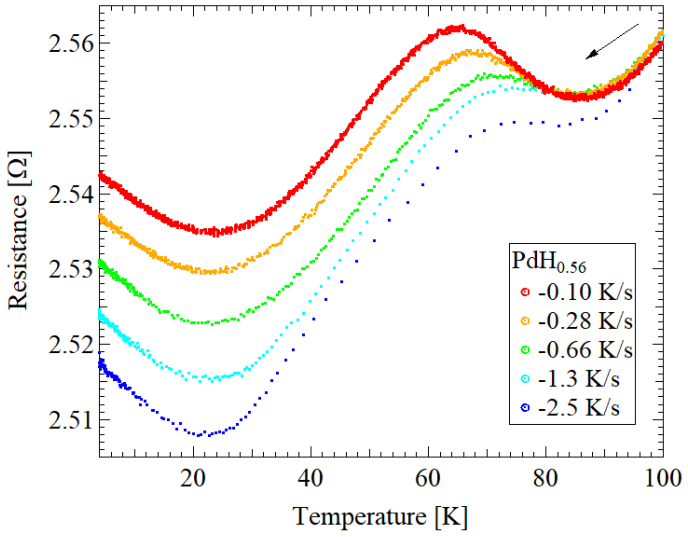

Figure 5.5: The resistance of the 50-nm-thick $PdH_{0.56}$ in cooling with various rates from -0.1 to -2.5 K/s.

action and the electron-phonon interaction, respectively. The last term of $\ln T$ dependence comes from the s-d exchange interaction representing the Kondo effect.

Figure 5.6 shows the temperature dependence of the resistance for PdH_x below 50 K. The resistance logarithmically depends on temperature below the temperature at which the resistance minimum was observed (T_{min}) , and the contributions of the term with $\ln T$, which is represented by a linear slope in Figure 5.6, gets larger as the hydrogen concentration x is larger. Fit results for the resistance by Eq. 5.1 using fit parameters of R_0, R_1, R_2 and $R_3^{'}(= cR_3)$ are also shown by dotted lines in Figure 5.6. The experimental data of temperature-dependent resistance were well approximated for all the specimens with various $x's$.

Figure 5.7 shows a relationship between the fit parameter $R_3^{'}$ and the hydrogen concentration x. $R_3^{'}$ depends on x linearly as expected by the Kondo effect. By replacing the impurity concentration c by an effective concentration of $x - x_0$, $R_3^{'}$ is rewritten as

$$R_3^{'} = R_3(x - x_0). \tag{5.2}$$

Concentration dependence of $R_3^{'}$ was well approximated by Eq. 5.2 as shown by the solid line in Figure 5.7, where x_0 was derived to be 0.15. This concentration value is consistent with the onset concentration of the (α+β) phase as confirmed in Figure 4.8, implying that the β phase is related to this resistance minimum phenomenon.

The relationship between the hydrogen concentration x and the resistance minimum temperature T_{min} shown in Figure 5.8 clearly demonstrated that T_{min} increases as x increases. From the Eq. 5.1, the concentration dependence of T_{min} is obtained by solving the equation of $\frac{dR}{dT} = 0$ as

$$T_{min} = \left(\frac{cR_3}{2R_1}\right)^{\frac{1}{2}} = ac^{\frac{1}{2}}, \tag{5.3}$$

where R_2 and R_3 are assumed to be independent of temperature and a is a constant. In this descrip-

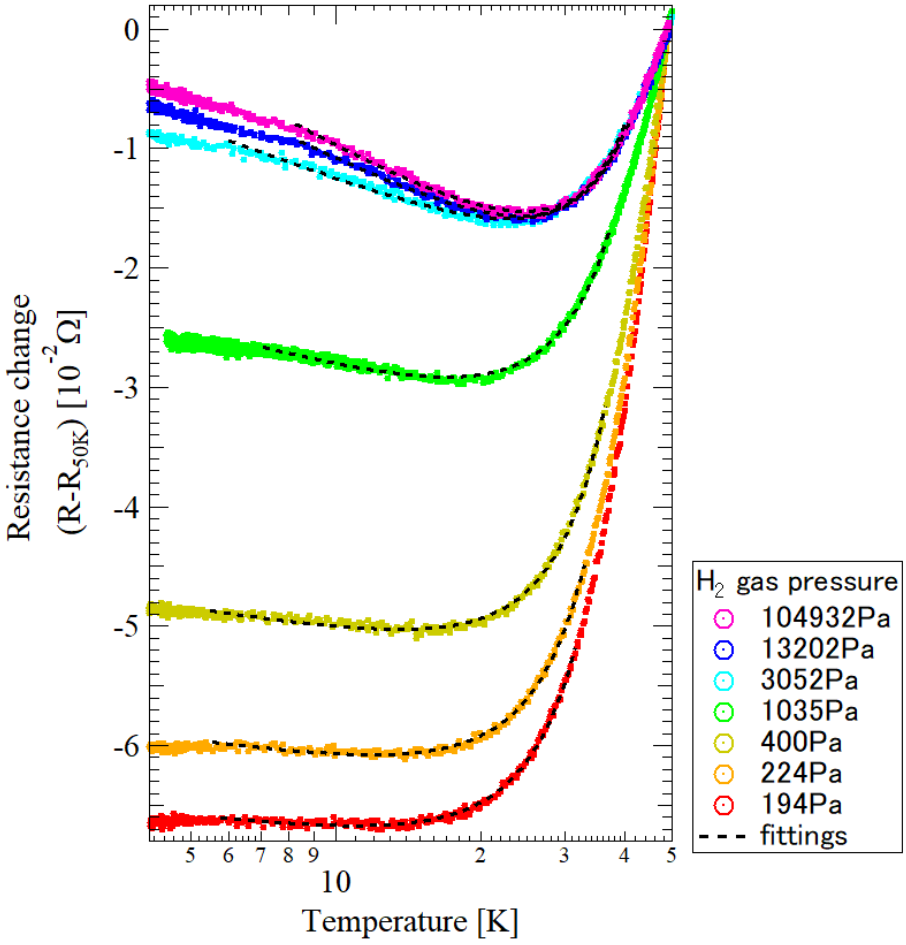

Figure 5.6: The temperature dependence of the resistance referred to that at 50 K of the 50-nm-thick Pd_x film with various $x's$ formed by hydrogen gas exposure at 200 K. Dashed lines represent the fit results by Eq. 5.1. The relationship between the dosing gas pressure and the concentration is given in Figure 4.8.

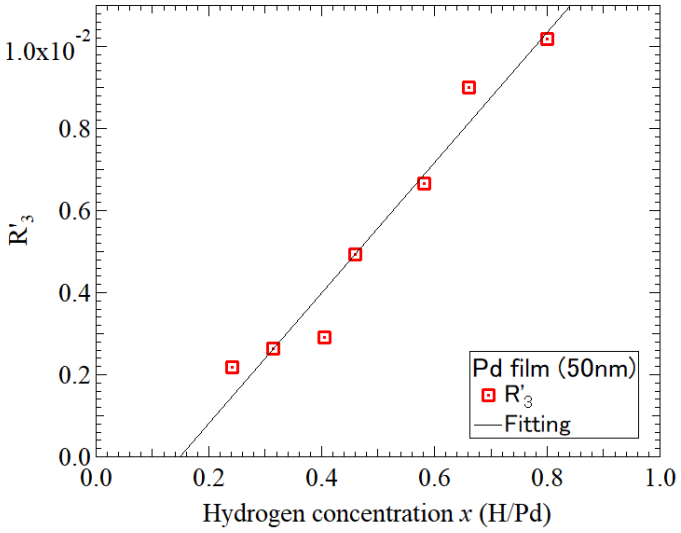

Figure 5.7: The concentration dependence of $R_3^{'}$ in the fit result using the Eq. 5.1 for the resistance of the 50-nm-thick PdH_x.

tion, the term of R_2T^5 is ignored since it is small as compared to R_1T^2 below 30 K in Eq. 5.1. As shown in Figure 5.8, the concentration dependence of T_{min} was well approximated by Eq. 5.3 with a fitting parameter of a using an effective concentration of $x - x_0$. x_0 was derived to be 0.13. Furthermore, the temperature dependence of the resistance for PdH_x in Figure 5.6 revealed that the resistance of PdH_x with high x tends to saturate at lower temperature region. This behavior is similar to the typical temperature-dependent resistance of the Kondo effect at lower temperature. T_{min} for PdD_x is shown in Figure 5.8. The resistance minimum temperature for PdD_x is similar to that for PdH_x.

As discussed so far, the Kondo effect is consistent to explain the resistance minimum phenomenon observed in PdH_x in the present study, and we propose the Kondo effect as a candidate to induce the resistance minimum by hydrogen absorption in Pd. In order to attribute this phenomenon to the Kondo effect, two points should be clarified. One is the origin of the localized spin. In general, localized spins are needed for the Kondo effect to appear because the Kondo effect represents the screening of the localized spin by conduction electrons. In metals, the 1s orbital of hydrogen is hybridized with the orbitals of metals and the localized spin in the 1s orbital is expected to vanish. Therefore it is hard to conceive that the hydrogen atom itself works as a magnetic impurity. The other point is the hydrogen concentration. Compared to the concentration of magnetic impurities of 1 % order or less in previous studies [51, 50] showing the resistance minimum by the Kondo effect, the hydrogen concentration in the present experiment is over one order larger. We speculate that a cluster-like structure of Pd and hydrogen atoms plays as a magnetic impurity for the Kondo effect as one possibility. Another possibility is related to a dynamical two-level system (TLS). In a TLS where atom or group of atoms moves between two different positions and has two levels close in energy, conduction electrons can be scattered by these centers [120, 121]. The TLS interacting with conduction electrons is described by the non-magnetic or orbital Kondo model, where the role of impurity spin is take over the internal degree of freedom of the TLS, namely the two positions of the fluctuator corresponds to the spin up and down of a magnetic impurity. We speculate that the resistance minimum in PdH_x observed in the present experiment originates from the TLS by hy-

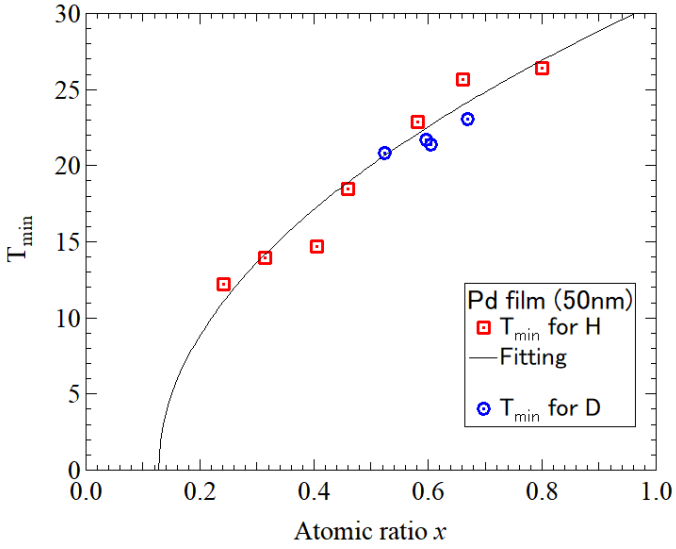

Figure 5.8: The concentration dependence of the minimum resistance temperature observed in the 50-nm-thick Pd film. A solid line represents the fit result by Eq. 5.3 for T_{min} of PdH_x.

drogen tunneling. The small isotope effect in T_{min} is consistent to the result of hydrogen(deuteron) diffusion in section 4.2 showing that the isotope effect in the hydrogen and deuterium hopping rates between the O sites is small below 50 K. Though the origin of the resistance minimum in PdH_x is still not clear, the temperature and concentration dependence on the resistance in the present study demonstrated that absorbed hydrogen can induce the Kondo-like effect in resistance of metals.

5.2.2 5-nm-thick palladium hydrides

5.2.2.1 Hydrogenation by H_2 gas exposure

Hydrogenation was performed by the H_2 gas exposure at 200 K, subsequent cooling and pumping in the same way as the 50-nm-thick sample. Some cycles of H_2 gas exposure and pumping were performed at 380 K to promote the hydrogenation and dehydrogenation of the Pd sample before the experiments.

Results of simultaneous measurements of resistance and TDS of mass 2 with a heating rate of 0.4 K/s are shown in Figure 5.9. The result of pure Pd shows a typical temperature dependence in resistance before the hydrogenation. After the hydrogenation, at first a hydrogen desorption peak was observed around 250 K. Its desorption amount got increased as the exposure gas pressure increased, and at the same temperature, the increased resistance by the hydrogen gas exposure returned to the original value of Pd, showing the formation of 5-nm-thick Pd hydrides by the hydrogen gas exposure and the recovery to Pd by heating. As the exposure gas pressure was larger than ~100 Pa, growth of an additional desorption peak and its corresponding decrease in resistance were observed around 200 K. Figure 5.10 shows the relationship between the desorption amount and the pressure. The desorption amount are overestimated for high pressure since the TDS peaks for the samples exposed to the hydrogen gas were buried in a background noise as can been seen in Figure 5.9 (c). A top axis of x in Figure 5.10 is estimated from the TDS peak area by assuming $x = 0.82$ at 0.1 MPa. Figure 5.11 shows relationship between the desorption amount and

the resistance change at 120 K. The plateau around 100 Pa in Figure 5.10 and 5.11 indicates the formation of α, (α+β) and β phases. As compared to the TDS in Figure 5.9 (c), the desorption at ~250 K and at ~200 K correspond to the α phase and the β phase, respectively. These hydrogen absorption/desorption properties of the 5-nm-thick Pd film are similar to those of the 50-nm-thick Pd film in section 4.2. Damage on the Pd lattice by the hydrogen absorption and desorption is negligible considering the recovery of the resistance by heating.

.

The hydrogen absorption property, however, is partially different between the two samples with thicknesses of 5 and 50 nm. As shown in Figure 5.10, the gas pressure to form the partial β phase for the 5-nm-thick Pd film is lower and the plateau representing the (α+β) phase is inclined as compared to the 50-nm-thick film. This behavior is similar to the hydrogen absorption property of Pd nanoparticles [73], indicating the size and/or surface effects on hydrogen absorption property even for flat 5-nm-thick film. The electronic property is also different. The increase in resistance by the formation of the β phase in the 5-nm-thick film is larger as represented by the large humps around 200 K in Figure 5.9 (b), and the resistance was not saturated even after the hydrogen gas exposure with 0.1 MPa. Therefore, the hydrogen absorption/desorption and electronic properties of the 5-nm-thick Pd film have some different points, which are considered to be related to the size and/or surface effects.

5.2.2.2 Temperature dependence of resistance

Figures 5.12 and 5.13 show the resistance and its temperature differential ($-dR/dT$) in heating for the 5-nm-thick PdH_x film, respectively. A resistance anomaly was observed around 80 K after the hydrogenation, whose onset concentration coincides with the formation of the β phase. This anomaly corresponds to the 50 K anomaly, though its intensity is weaker and its temperature is higher as compared to those of the 50-nm-thick PdH_x. Furthermore, resistance minimum was observed around 10 K as shown in Figure 5.14.

5.2.2.3 Analysis in terms of the Kondo effect

Fit results using Eq. 5.1 with fit parameters of R_0, R_1, R_2 and $R_3^{'}$ are shown by dotted lines in Figure 5.14. As can been seen, the experimental data of the resistance for the specimens with various $x's$ were well expressed by Eq. 5.1, suggesting that this resistance anomaly can be explained by the Kondo effect.

The hydrogen concentration dependence of the fit parameter $R_3^{'}$ is shown in Figure 5.15, where a liner fit for small $x's$ is represented by a solid line, revealing that $R_3^{'}$ increases as the hydrogen concentration increases for small $x's$. For high $x's$, in contrast, slightly $R_3^{'}$ decreases unlike the results of the 50-nm-thick PdH_x. These results demonstrated that the Kondo effect is suppressed for large $x's$. Figure 5.16 shows the concentration dependence of the resistance minimum temperature (T_{min}) and its fit result for small $x's$ by Eq. Eq. 5.3. In accordance with $R_3^{'}$, T_{min} increases up to to 12 K. The saturated temperature of T_{min} in the 5-nm-PdH_x is smaller than T_{min} = 25 K of the 50-nm-PdH_x at $x = 0.82$. Furthermore, Figures 5.15 and 5.16 show $R_3^{'}$ and T_{min} increase from $x = 0$, i.e. x_0 is 0. This is considered to be related to the hydrogen absorption property of the 5-nm-thick PdH_x, where the plateau representing the (α+β) phase is inclined and β phase tend to be formed as discussed above.

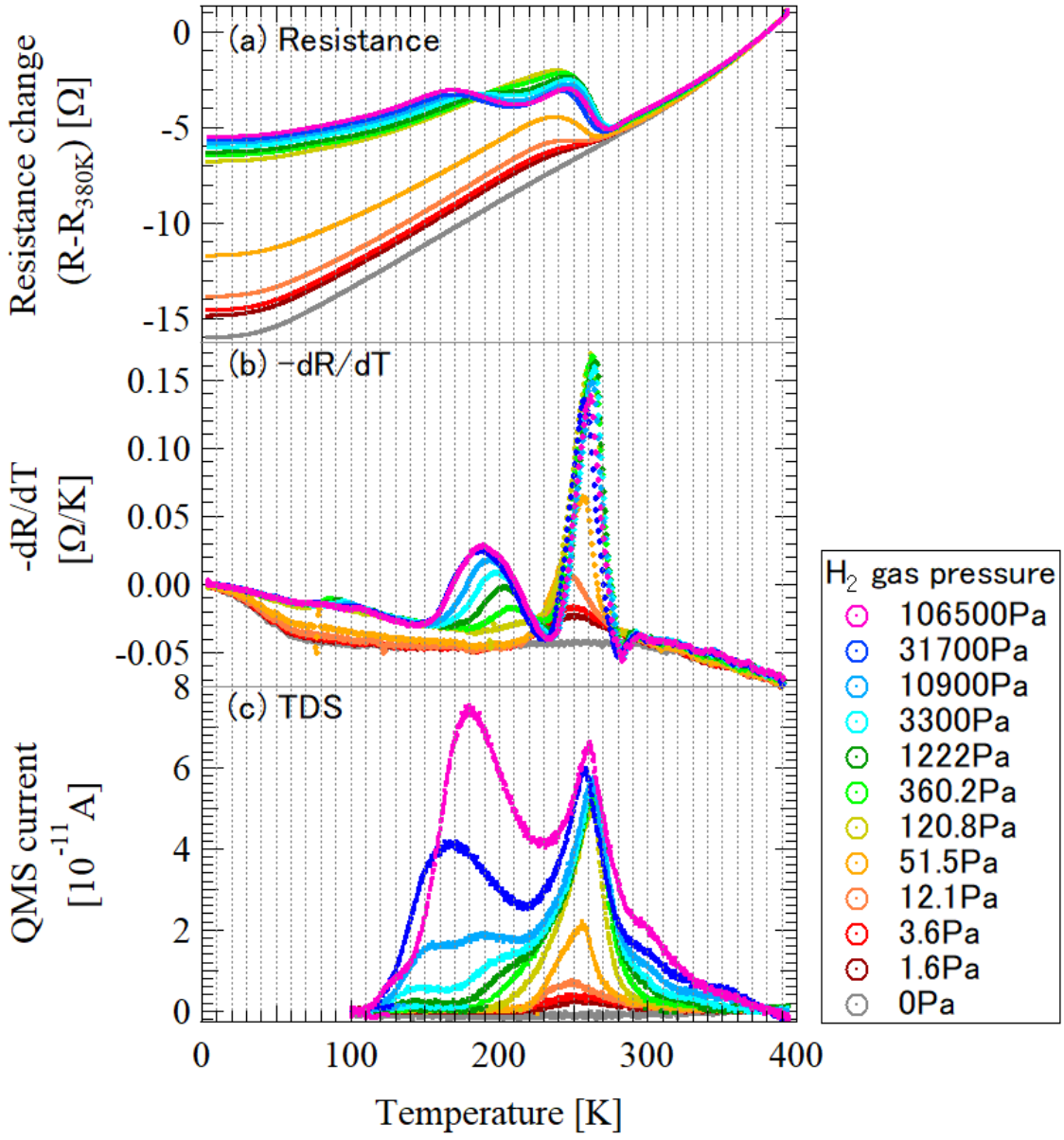

Figure 5.9: The result of simultaneous measurement of resistance and TDS for the 5-nm-thick Pd film after hydrogen gas exposure with various pressures at 200K. (a) resistance referred to that at 380 K (R_{380K} = ~60 Ω), (b) temperature deferential of the resistance and (c) TDS.

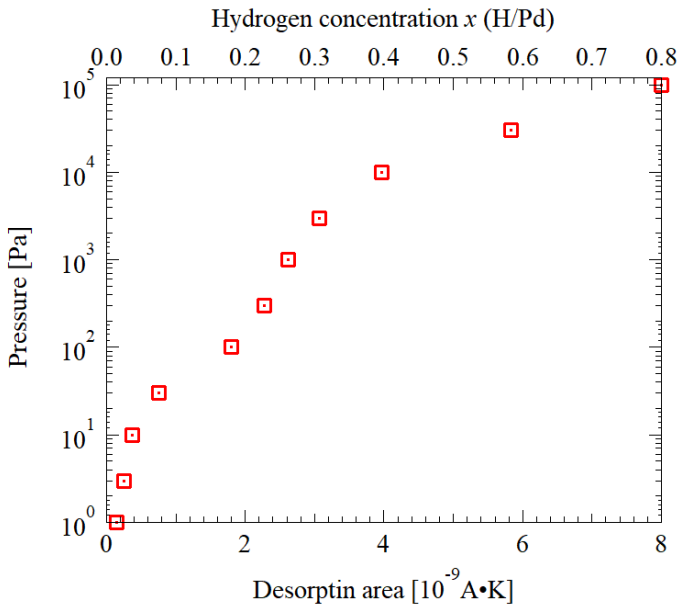

Figure 5.10: Relationship between the H_2 dosing gas pressure at 200 K and the desorption amount of mass 2 in TDS for the 5-nm-thick Pd film. Hydrogen concentration is derived by assuming $x = 0.82$ at 0.1 MPa.

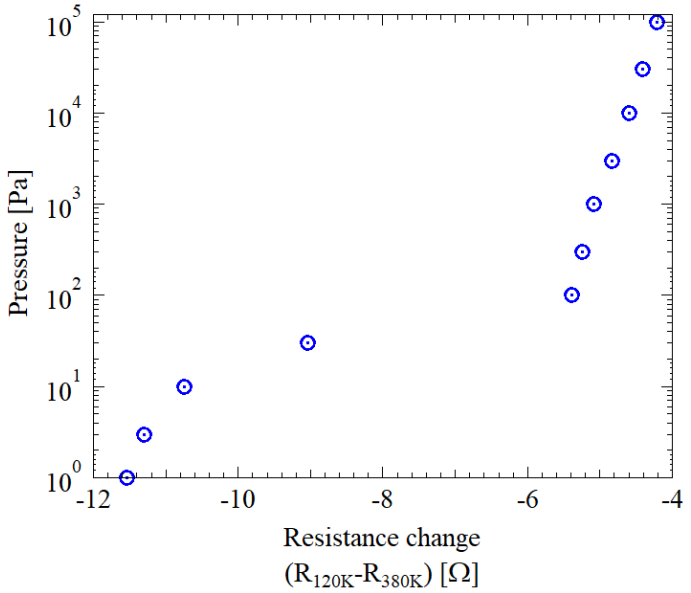

Figure 5.11: Relationship between the H_2 dosing gas pressure at 200 K and the resistance change of the 5-nm-thick Pd film at 120 K referred to that at 380 K.

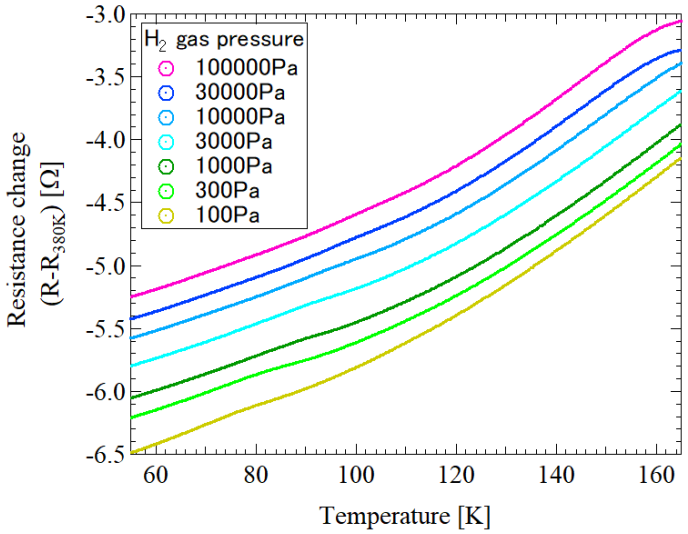

Figure 5.12: The temperature dependence of the resistance of the 5-nm-thick PdH_x film with various $x's$ around 100 K. The resistance is displayed referred to that of 380 K.

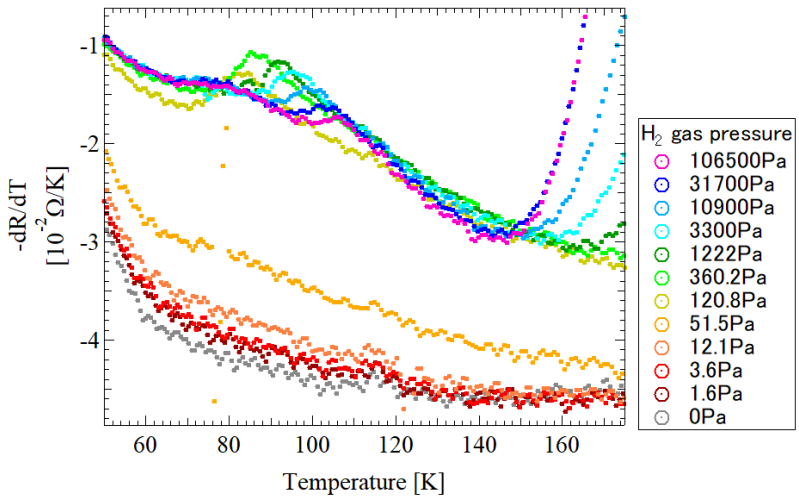

Figure 5.13: The temperature differential of the resistance of the 5-nm-thick PdH_x film in heating.

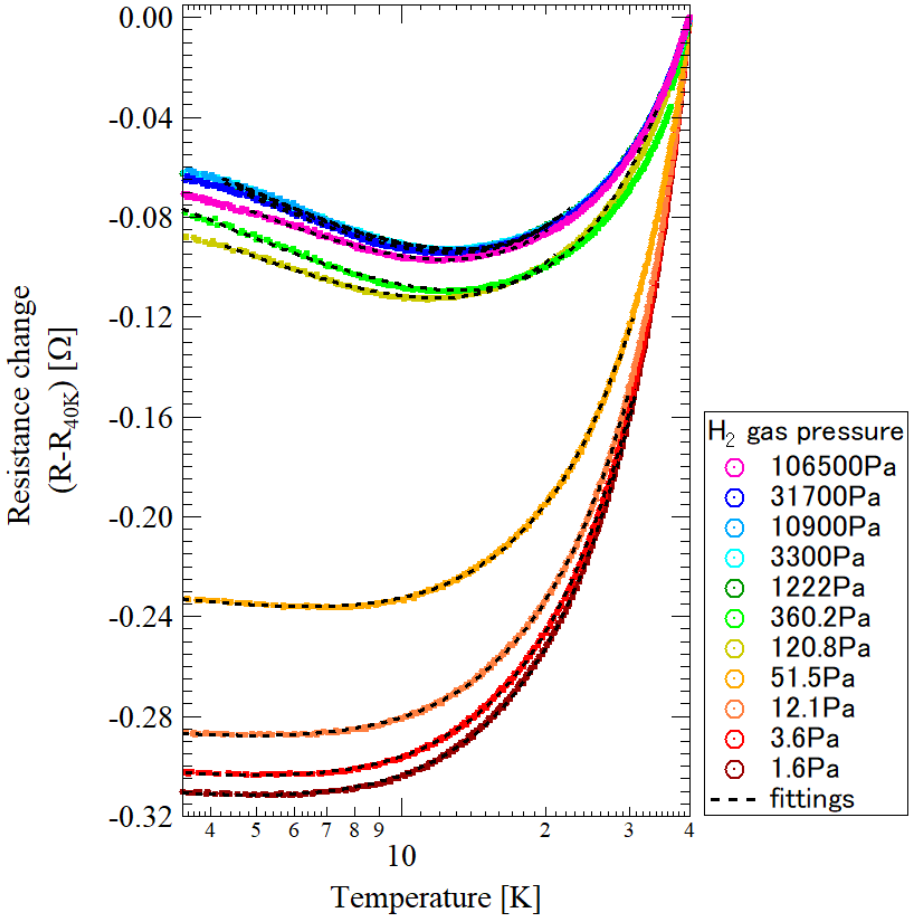

Figure 5.14: The temperature dependence of the resistance of the 5-nm-thick Pd_x film with various $x's$. Dashed lines represent the fit results by Eq. 5.1.

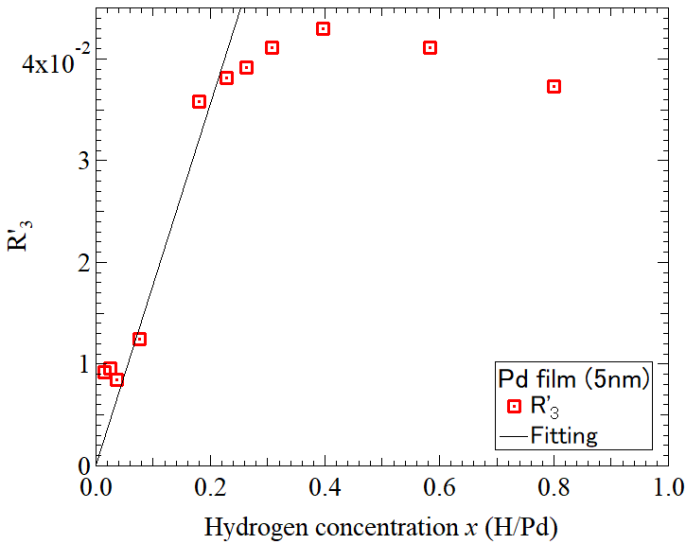

Figure 5.15: The concentration dependence of $R_3^{'}$ in the fit result using the Eq. 5.1 for the resistance of the 5-nm-thick PdH_x.

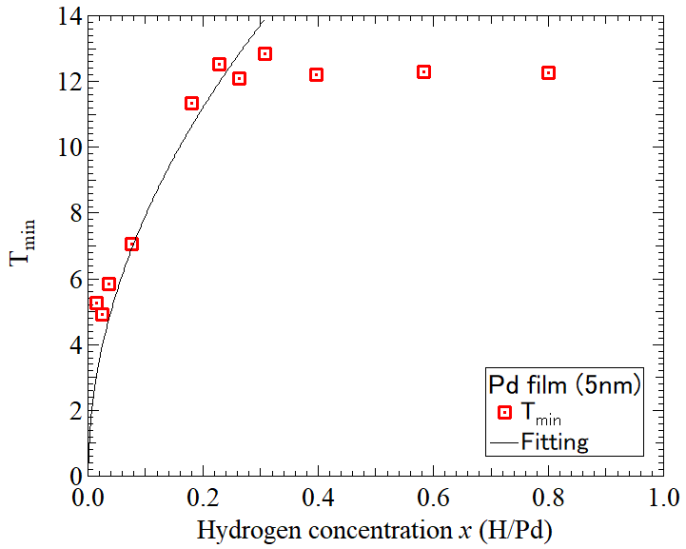

Figure 5.16: The concentration dependence of the minimum resistance temperature observed in the 5-nm-thick Pd film.

5.2.3 2-nm-thick palladium hydrides

5.2.3.1 Hydrogenation by H_2 gas exposure

Hydrogenation of the 2-nm-thick Pd films was performed by the H_2 gas exposure at 200 K, subsequent cooling and pumping in the same way as the 50-nm-thick sample. Some cycles of H_2 gas exposure and pumping were performed at 380 K to promote the hydrogenation and dehydrogenation of the Pd sample before the experiments.

Figure 5.17 shows results of simultaneous measurements of resistance and TDS of mass 2 with a heating rate of 0.4 K/s performed for the 2-nm-thick Pd film. Figure 5.18 is a logarithmic display of the TDS results. After the hydrogenation, a hydrogen desorption peak was observed around 230 K, and got increased as the gas pressure increased. Accordingly, the increased resistance by the hydrogen gas exposure returned to the original value of Pd, which means that the 2-nm-thick Pd film is hydrogenated by gas exposure and recovered to Pd by heating. Additional hydrogen desorption peaks were observed below 200 K for the specimens exposed to the gas with higher pressures. The TDS peaks from the samples exposed to high pressure gases were buried in a background noise. As compared to the 5- and 50-nm-Pd films, the resistance change corresponding to the additional desorption below 200 K is relatively larger as can been in Figure 5.17 (b). The relationship between the desorption amount and the pressure are shown in Figure 5.19, where the top axis is estimated from the TDS peak area by assuming $x = 0.82$ at 0.1 MPa. It should be mentioned that the amount of desorption is overestimated to some extent for the hydrogen gas exposure with high pressures. The relationship between the desorption amount and the resistance difference between 120 K and 380 K is shown in Figure 5.20. These relationships revealed that the 2-nm-Pd hydrides are unique and apparently different from those of 5- and 50-nm-Pd hydrides. There is not a plateau corresponding to the (α+β), indicating that distinct phases of α, (α+β) and β phases are no longer present in the 2-nm-thick PdH_x. Damage on the Pd lattice by the hydrogen absorption and desorption is negligible as confirmed by the recovery of the resistance by heating.

5.2.3.2 Temperature dependence of resistance of 2-nm-thick Pd

Figure 5.21 shows the temperature dependence of the resistance of the 2-nm-thick Pd film before the hydrogenation. The resistance linearly depends on temperature above 100 K, which is a typical behavior of normal metals. On the other hand, a minimum in resistance was observed around 30 K.

5.2.3.3 Analysis in terms the Anderson localization

Since this resistance minimum was observed before the hydrogenation, it is not a phenomenon related to the Kondo effect induced by hydrogen absorption which we have discussed so far in the thicker Pd films. Figure 5.22 shows the the temperature-dependent resistance at low temperature of the 2 nm Pd in a logarithmic scale, which revealed that the resistance logarithmically depends on temperature at low temperature as shown by a dotted line. According to the Scaling theory, the resistance in a two-dimensional system with a disordered potential depends on temperature as -ln T at low temperature, which is called the Anderson localization [52, 54].

Here, solving Schrödinger equation of a particle with mass m in an one-dimensional infinite potential well with a thickness of d, the energy eigenvalues (E_n) are given as

$$E_n = \frac{([n+1]\pi\hbar)^2}{2md^2} \qquad (n = 0, 1, 2, ...), \tag{5.4}$$

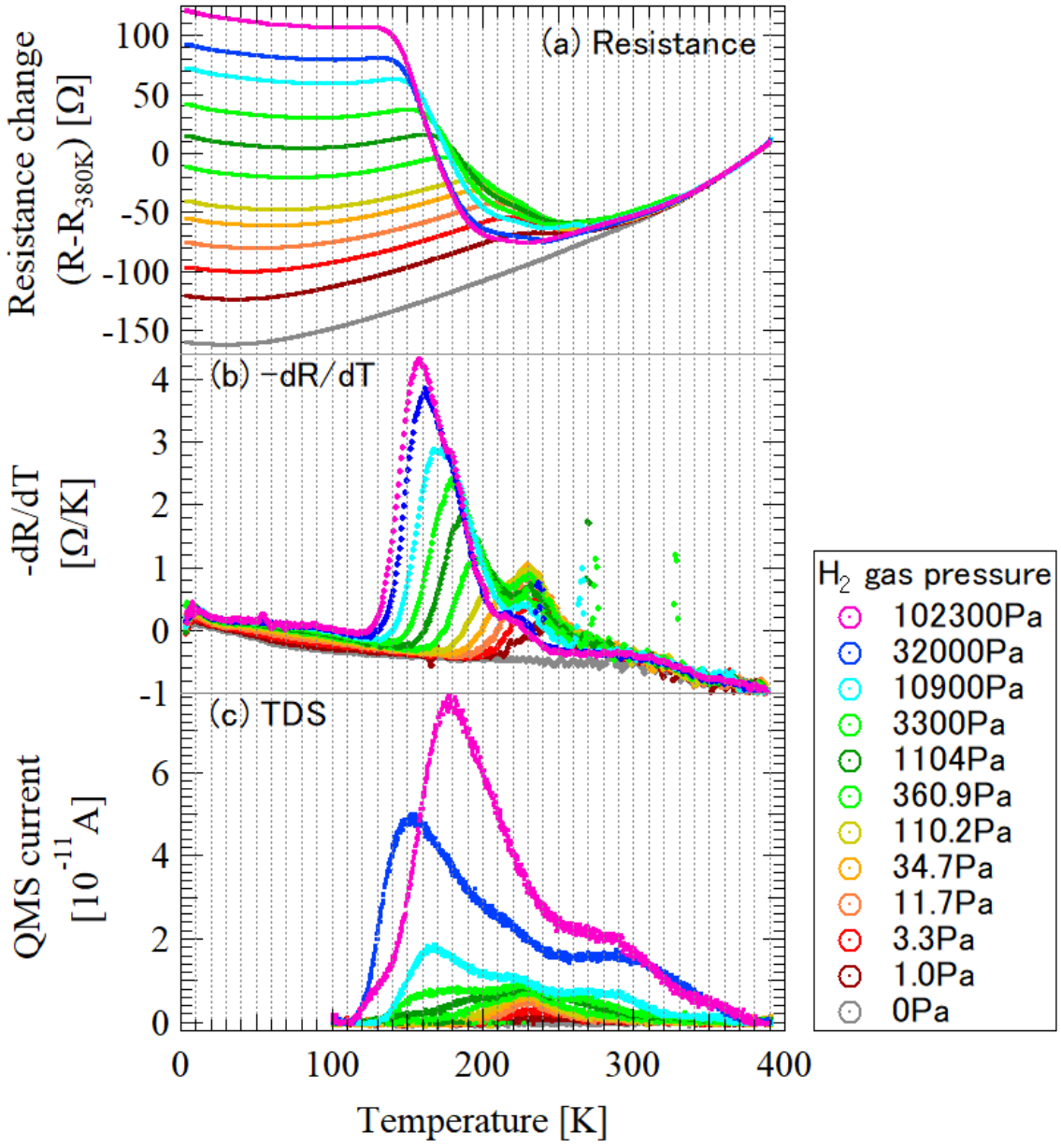

Figure 5.17: The result of simultaneous measurement of resistance and TDS for the 2-nm-thick Pd film after hydrogen gas exposure with various pressures at 200K. (a) resistance referred to that at 380 K (R_{380K} = ~2170 Ω), (b) temperature deferential of the resistance and (c) TDS.

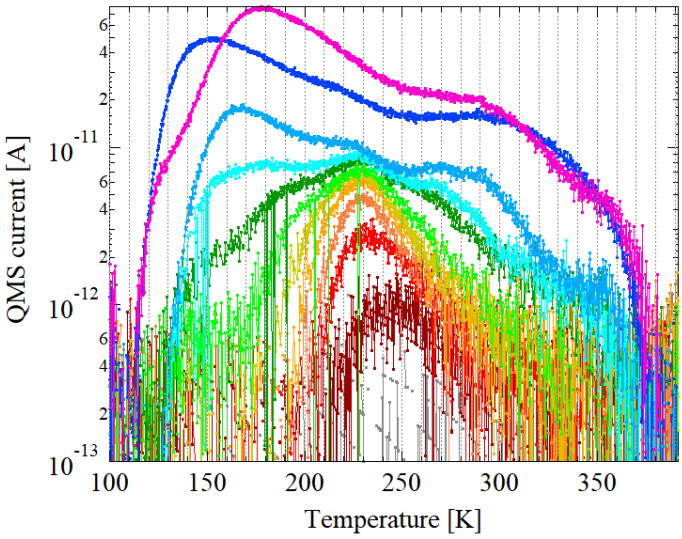

Figure 5.18: Logarithmic display of the TDS in Figure 5.17.

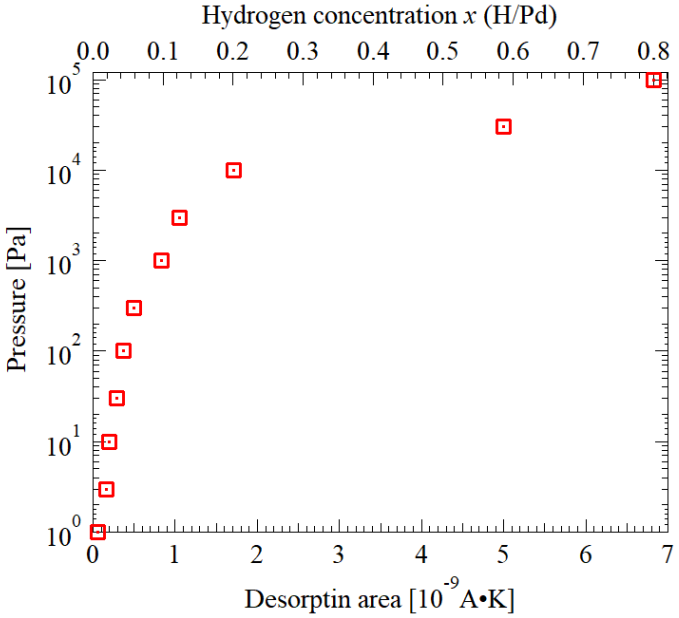

Figure 5.19: Relationship between the H_2 dosing gas pressure at 200 K and the desorption amount of mass 2 in TDS for the 2-nm-thick Pd film. Hydrogen concentration is derived by assuming $x = 0.82$ at 0.1 MPa.

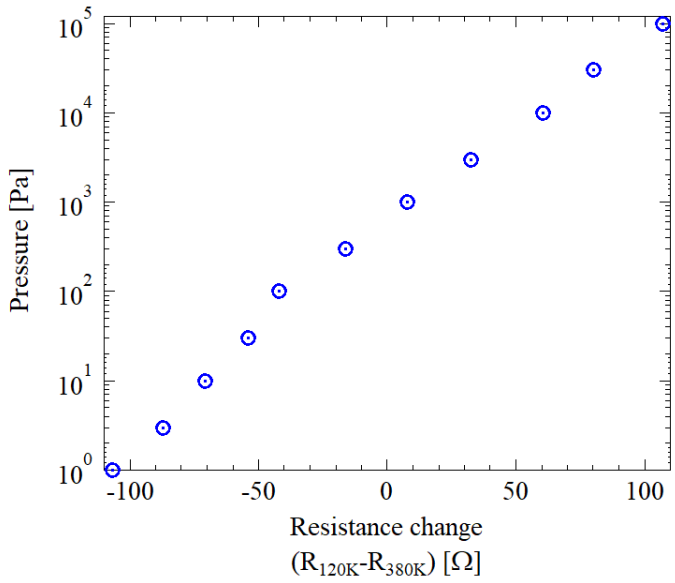

Figure 5.20: Relationship between the H_2 dosing gas pressure at 200 K and the resistance change of the 2-nm-thick Pd film at 120 K referred to that at 380 K.

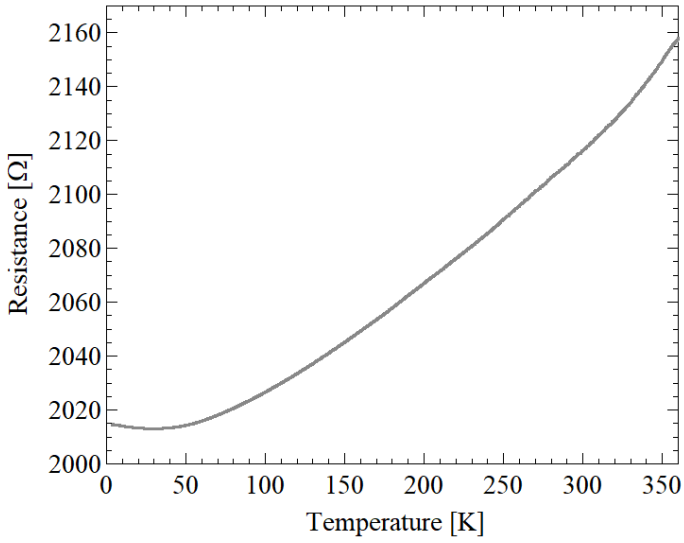

Figure 5.21: The temperature dependence of the resistance of the 2-nm-thick Pd film before the hydrogenation.

where $\hbar$ is the reduced Planck constant. Since the energy difference of $E_1 - E_0$ is derived to be $\sim$ 0.3 eV in case of $d = 2$ nm, it is reasonable to regard the specimen as a two-dimensional system.

Figure 5.23 shows thickness dependence of the resistivities at 300 K observed for the 2, 5, 10 and 50-nm-thick Pd films. The resistivity of the 50-nm-thick specimen is 10.2 μΩ·cm, which is in good agreement with $\rho_0 = 11.2$ μΩ·cm in thick Pd films with a thickness above 25 nm [122]. Fuchs and Sondheimer (FS) considered the size effect on the electrical resistivity ρ taking into account isotropic scattering and surface scattering, and described ρ of a thin film with a thickness d as

$$\rho = \rho_0 \left(1 + \frac{C}{d}\right), \tag{5.5}$$

where ρ_0 is the resistivity of the bulk material and C is a constant determined by the specularity and the electron mean free path [123, 124, 125]. In this description, it is assumed that the structure and the defect density in the film are the same as those in the bulk material. The fit result using Eq. 5.5 is shown by a solid line in figure 5.23. The experimental data was well approximated except for the resistivity of the 2 nm film, which deviated from the fitting. This deviation is considered to be attributed to electron scattering by lattice defects such as grainboundaries, which is ignored in the FS description. In fact, it is experimentally known that the defect density is larger in very thin films [126, 122, 127]. Hence, it is conceivable that the 2-nm-Pd film in the present study is disordered to some extent.

Therefore, it is reasonable to conclude that the logarithmic temperature dependence of resistance and its consequent phenomenon of resistance minimum observed in the 2-nm-thick Pd below 30 K is attributed to the Anderson localization related to the low dimensionality of the electron system and the randomness of the potential.

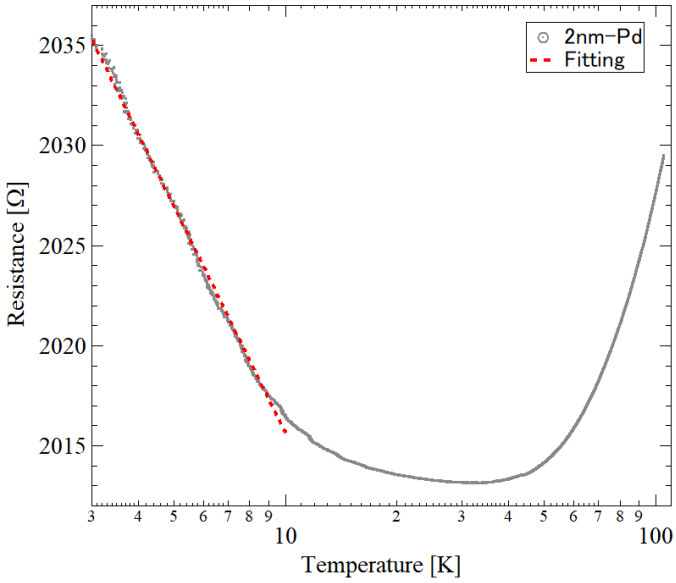

Figure 5.22: The temperature dependence of the resistance of the 2-nm-thick Pd film at low temperature before the hydrogenation. A logarithmic fitting is represented by a dashed line. Difference in Figures 5.21 and 5.22 comes from whether the radiation shield is used or not. The shield was used in this resistance measurement.

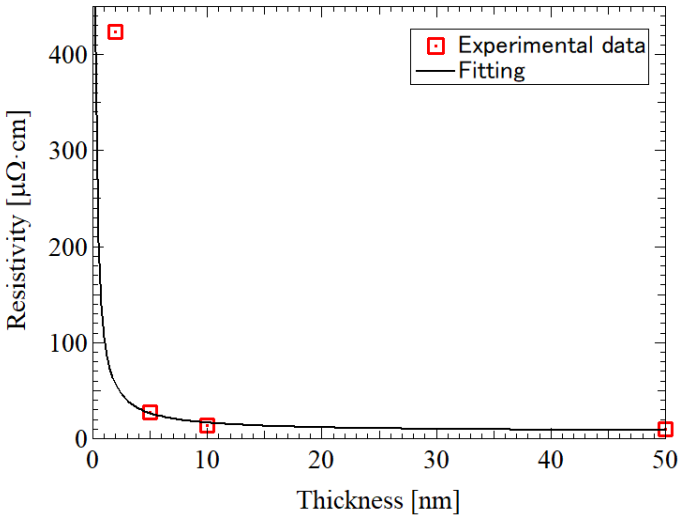

Figure 5.23: Resistivity of the Pd films at 300 K according to the film thickness. The fit by the FS description is represented by a solid line.

5.2.3.4 Temperature dependence of resistance

Figure 5.24 shows the temperature differential of the resistance ($-dR/dT$) of the 2-nm-thick PdH_x in heating. An apparent anomaly in resistance was not observed between 50 and 100 K, which means that 2-nm-thick PdH_x specimen dose not show the 50 K anomaly. As compared to the thicker films with thicknesses of 5 and 50 nm and a bulk, such a electronic transport in the 2-nm-thick PdH_x film is remarkably unique as well as its hydrogen absorption property.

Figure 5.25 shows the temperature dependence of the resistance at low temperature for the 2-nm-thick PdH_x with various $x's$. In addition to the -ln T term of the Anderson localization at low temperature, another -ln T term in resistance appeared as the specimen was hydrogenated. Moreover, this result revealed that these two -ln T terms in the temperature-dependent resistance can coexist.

5.2.3.5 Analysy in terms of the Kondo effect and the Anderson localization

The fit results of the temperature dependence of the resistance above 10 K by the equation (a) $R(T) = R_0 + R_1T^2 + R_2T^5 - R_3' \ln T$ with fit parameters of R_0, R_1, R_2 and R_3' are shown as a dotted lines in Figure 5.25. The regions below 10 K were fitted by (b) $R(T) = R_4 - R_5 \ln T$ with fit parameters of R_4 and R_5 as shown by dashed-dotted lines. One can recognize that the experimental data were well approximated by the two equations in each temperature region. Based on the results so far, the term of $-R_3' \ln T$ probably corresponds to the Kondo effect induced by hydrogen absorption and the $-R_5 \ln T$ term corresponds to the Anderson localization. These results indicate that the Kondo effect remains in a two-dimensional system, and the Anderson localization coexists with the Kondo effect.

Figure 5.26 shows the hydrogen concentration dependence of the R_3' due to the Kondo effect, showing that R_3' increases linearly by increasing the concentration for small x'. This tendency is similar to the cases of the 5 and 50-nm-thick specimens. In contrast, T_{min} increases toward 100K and it is significantly higher than those of the 5 or 50 nm films as shown in Figure 5.27.

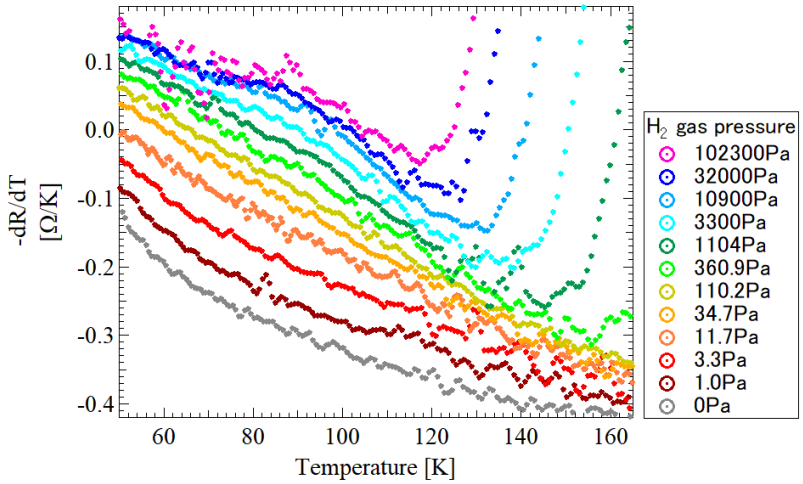

Figure 5.24: The temperature differential of the resistance of the 2-nm-thick PdH_x film in heating.

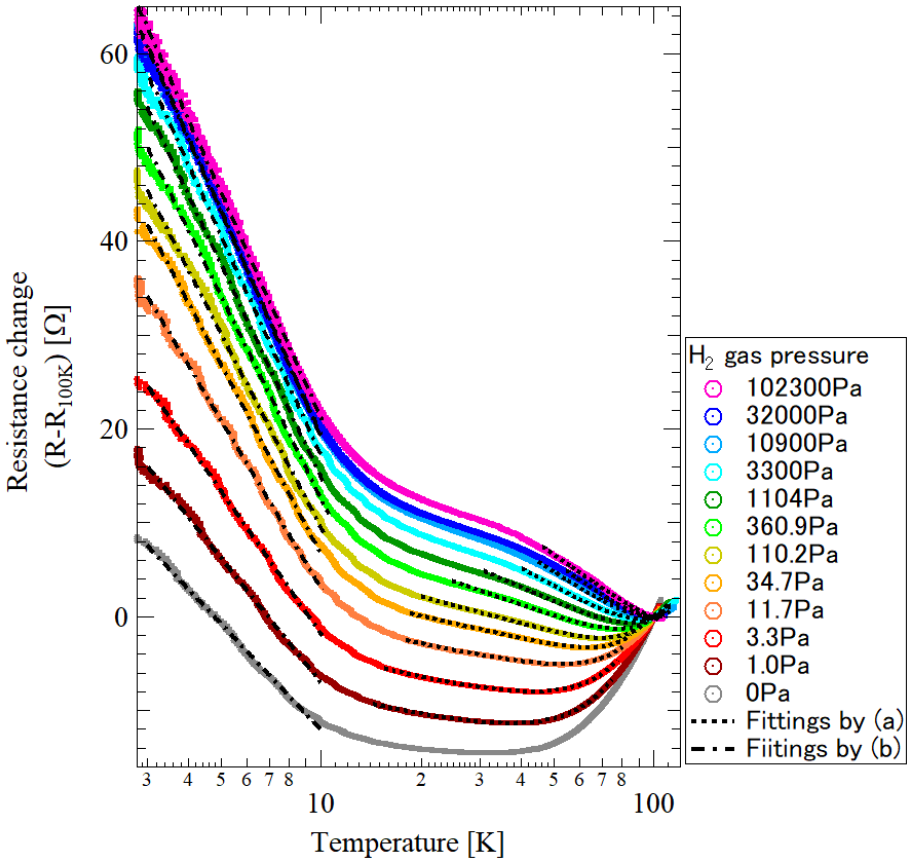

Figure 5.25: The temperature dependence of the resistance of the 2-nm-thick Pd_x film with various $x's$. Dashed lines and dashed-dotted lines represent the fit results by Eq. (a) $R(T) = R_0 + R_1T^2 + R_2T^5 - R_3^{'} \ln T$ and (b) $R(T) = R_4 - R_5 \ln T$, respectively.

The concentration dependence of the R_5 representing the Anderson localization is shown in Figure 5.28, where the difference of $R_5 - R_3^{'}$ is also shown. The difference increases as x gets larger for small $x's$, which experimentally implies that the Anderson localization is enhanced in the system with the Kondo effect. Theoretically, the interaction of electrons with randomness in terms of the Kondo effect have been discussed, and it is expected that the electrical conductivity in a disordered system with magnetic impurities decreases more rapidly as the temperature decreases thorough the interplay between the Anderson localization and the Kondo effect in the weakly localized regime [128]. Our result is consistent with this prediction.

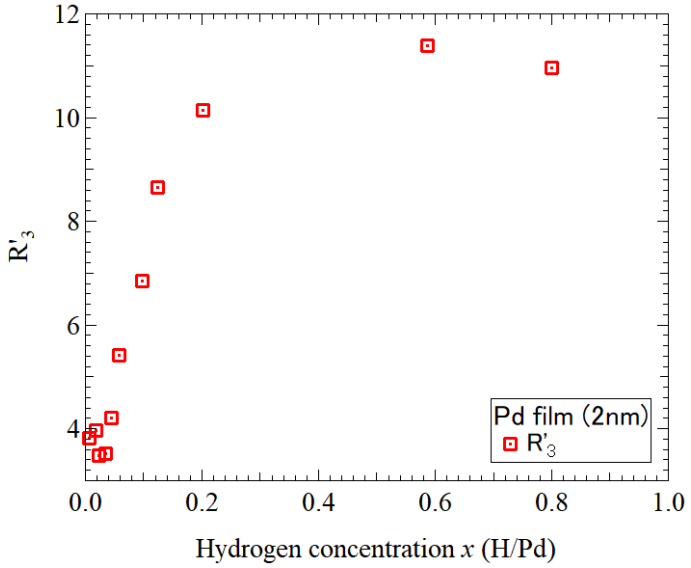

Figure 5.26: The concentration dependence of $R_3^{'}$ in the fit result using the Eq. (a) for the resistance of the 2-nm-thick Pd_x.

5.2.4 Size and surface effects on the Kondo effect

Finally, we discuss the thickness dependence of the Kondo effect. Concentration dependence of T_{min} observed in PdH_x with thicknesses of 2, 5 and 50 nm is summarized in Figure 5.29. The observed T_{min} is in the order of the 2, 50 and 5 nm films.

Here we take into account the size effect. In general, the contribution of the Kondo effect is expected to be modulated and depend on the film thickness when the film thickness is smaller than the length for conduction electrons to screen out the localized spin, which is called the Kondo length. Its Kondo screening cloud is restricted to quasi two dimensions. Previous experimental studies revealed that the contributions of the Kondo effect, represented by the slopes of the logarithmic part in resistance of Au films with Fe impurities and Cu films with Fe impurities shown in Figure 5.30 and 5.31, decreases as the thickness is reduced [129, 130]. The present results showing that T_{min} and the contribution of the logarithmic part in the 5-nm-PdH_x induced by hydrogen absorption are smaller than those in the 50-nm-thick PdH_x, which are consistent with the previous studies. However, this size effect is inconsistent with the significantly high T_{min} in the 2-nm-thick film.

In contrast, the surface effect might be crucial for the Kondo effect in such an ultrathin film.

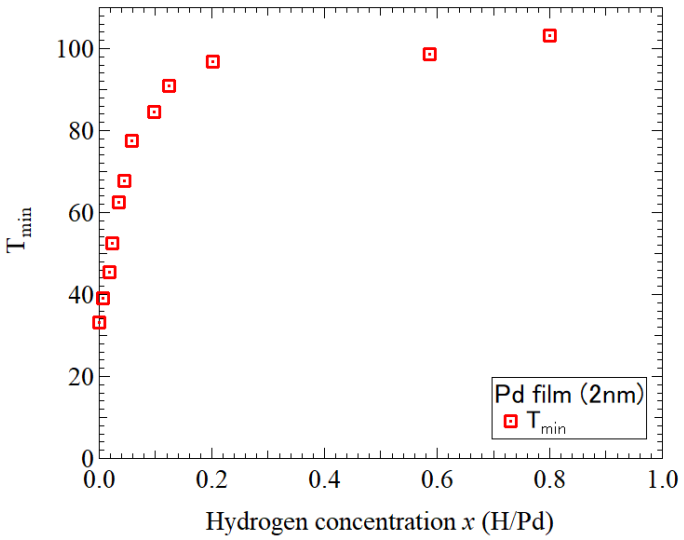

Figure 5.27: The concentration dependence of the minimum resistance temperature observed in the 2-nm-thick Pd film.

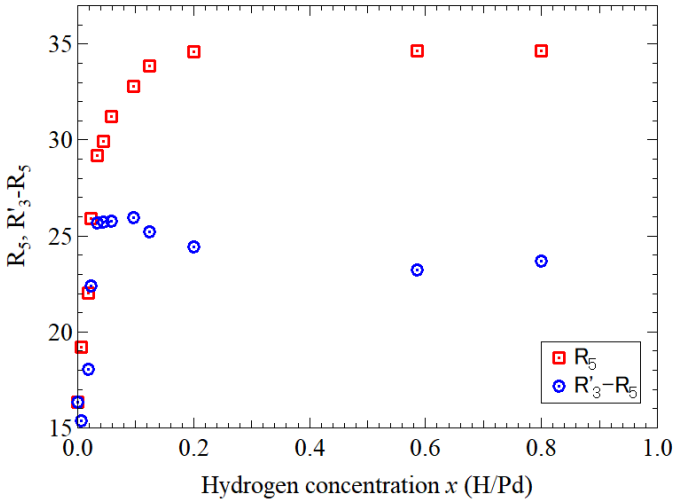

Figure 5.28: The concentration dependence of R_5 and difference of $R_5 - R_3^{'}$ in the fit result using equations (a) and (b) for the resistance of the 2-nm-thick Pd_x.

The characteristic electronic structure near the surface might modulate the Kondo temperature and the contribution of Kondo effect in resistance. Crépieux calculated the Kondo temperature of a film with a magnetic impurities in a specific plane (indexed γ) by means of a variational method using a tight-binding model [131]. Figure 5.32 shows the calculation result of the Kondo temperature, divided by the value for bulk, of a film with 20 layers as a function of the γ-plane position. This indicate that the Kondo temperature can be largely modulated near the surface. The C_{Film} coefficient giving the magnitude of the logarithmic contribution of the Kondo effect in resistance according to film thickness n for a film with homogeneously distributed impurities was also calculated as shown in Figure 5.33. This calculation clearly indicates that the contribution of the Kondo effect in resistance can be significantly modulated in ultrathin films with layers below 10. Hence, the high T_{min} observed in the 2-nm-thick PdH_x might be associated with the electronic states near the surface. Furthermore, the characteristic structure of the 2-nm-thick Pd hydrides in which α, (α+β) and β phases are not distinguishable, might also affect the Kondo effect. In fact, the electronic property of the 2-nm-thick PdH_x is unique as represented by the disappearance of the 50 K anomaly. We speculate that the significant high T_{min} in the 2 nm Pd hydrides is the consequence of the surface effect including the electronic states and the hydrogen states.

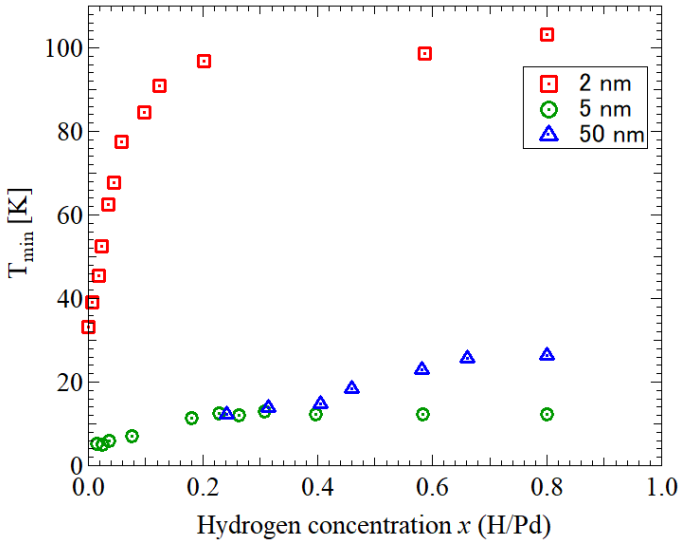

Figure 5.29: The thickness dependence of the minimum resistance temperature observed in the 2, 5 and 50-nm-thick PdH_x.

5.2.5 Conclusion

A appearance of a resistance minimum phenomenon induced by the hydrogen absorption was observed at low temperature in the Pd nanofilms. Analysis of the temperature and the hydrogen concentration dependence of the resistance revealed that the resistance minimum by hydrogen absorption can be explained by the scheme of the Kondo effect. Furthermore, a resistance minimum was also observed in the 2-nm-thick Pd film even without the hydrogenation, which is attributed to the Anderson localization. We experimentally showed that the Anderson localization might be enhanced by the Kondo effect. The variation in the resistance minimum temperature depending on the film thickness demonstrated the size effect related to the Kondo screening cloud and the surface

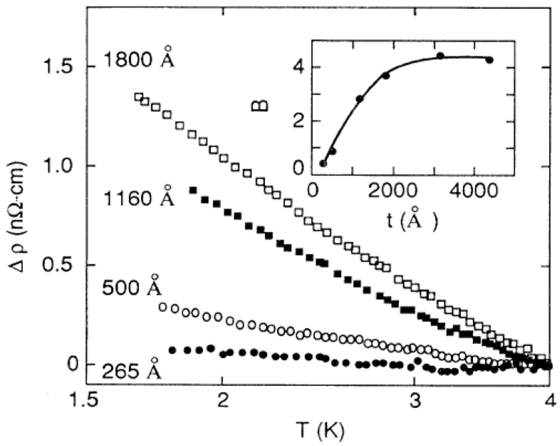

Figure 5.30: The thickness dependence of the temperature-dependent resistance in 0.003 % Fe in Au films [129].

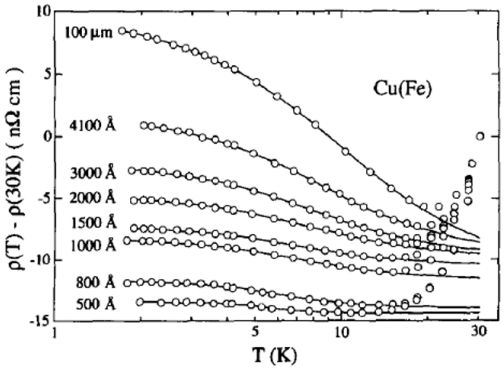

Figure 5.31: The thickness dependence of the temperature-dependent resistance in 0.013 % Fe in Cu films [130].

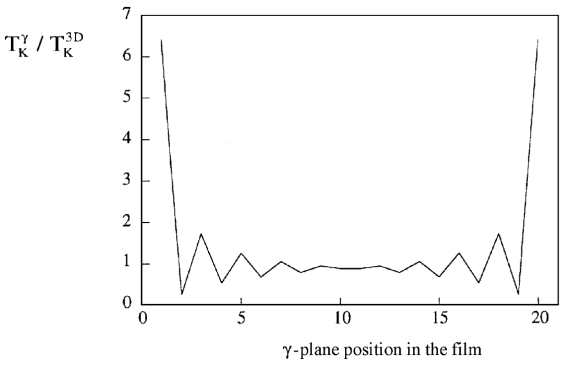

Figure 5.32: Calculated Kondo temperature, divided by the value for a bulk, of a film with 20 layers as a function of the γ-plane position [131].

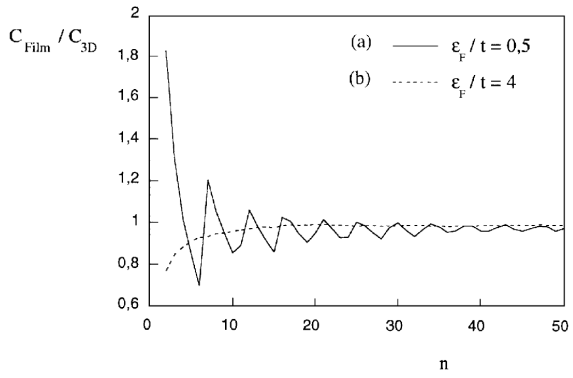

Figure 5.33: Calculated C_{Film} coefficient, divided by the value for a bulk, of a film according to film thickness n [131].

effect associated with the electronic and hydrogen states on the Kondo effect.

Chapter 6

Structure and dynamics of palladium hydrides

Analysis of the hydrogen lattice location and hydrogen vibration mode is necessary to clarify the electronic state and hydrogen diffusion in metals. We developed a channeling NRA apparatus with a depth resolution to analyze the hydrogen sites, and investigated the structure of the metastable Pd hydrides formed by hydrogen ion implantation. Inelastic neutron scattering was performed for PdH_x nanofilms to elucidate the hydrogen vibration mode near a two-dimensional surface of Pd.

6.1 Channeling NRA

Electronic states of metal hydrides are possibly different depending on where hydrogen atoms are located in metals. In particular, the near-surface region has a possibility for specific hydrogen absorption, which might be crucial for surface electronic states and is also important as an inevitable pass of hydrogen absorption and desorption. However, conventional methods such as neutron scattering or nuclear magnetic resonance do not distinguish the hydrogen atoms near surfaces from those in bulks. A quantitative method to determine the hydrogen lattice location with a depth resolution is highly needed. In this thesis, we developed the apparatus for simultaneous measurement of resonance NRA and Rutherford backscattering spectroscopy, which is called the channeling NRA and makes it possible to determine the hydrogen sites with a depth resolution of nm order taking advantage of the ion channeling technique and the resonant nuclear reaction.

6.1.1 Principle

6.1.1.1 Rutherford backscattering spectroscopy

Fast accelerated ions with an energy of MeV order are elastically scattered by Coulomb interaction of nuclei, which is called Rutherford scattering [132]. When an incident ion with mass M_1 and a kinetic energy E_0 is scattered in the direction of θ with an energy E_1 by a target atom at rest with mass M_2, as schematically shown in Figure 6.1, the following equation must be satisfied by the

conservation of energy and momentum:

$$E_1 = \left(\frac{M_1 \cos\theta + \sqrt{M_2^2 - M_1^2 \sin^2\theta}}{M_1 + M_2} \right)^2 E_0, \tag{6.1}$$

where the coefficient term is called the kinematic factor. The mass of the target atom (M_2) is determined by analyzing the energies of scattered ions (E_1) at a certain angle. Rutherford backscattering spectroscopy (RBS) is a method to determine the mass and the the crystal structure of the target by the analysis of energy and intensity of the backscattered ions.

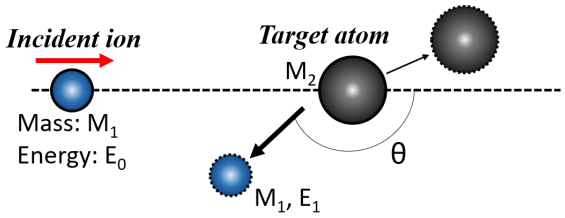

Figure 6.1: Schematic illustration of RBS.

6.1.1.2 Ion channeling

When accelerated positive ions are injected to a monocrystalline material within a small angle of θ_c against the host crystalline axes, positively charged ions can not get close enough to the lattice nuclei due to the shadowing and the repulsion between the ions and nuclei, which makes the probability of close-encounter events with a large angle Rutherford scattering small. As a result, the injected ions undergo events with a small angle Rutherford scattering and they travel longer distances through the channels surrounded by the lattice rows as schematically shown in Figure 6.2 [133]. This phenomenon is called the ion channeling. Figure 6.3 schematically shows the typical RBS yield reflecting the close-encounter event probability as a function of the incident beam angle with respect to a certain crystalline axis. The amount of backscattered ions decreases and the flux through the channels increases under the ion channeling condition as compared to a random incidence. When positive ions with an atomic number Z_1 and an incident energy E_1 are injected to a monocrystalline material with an atomic number Z_2, the critical angle (θ_c), or the FWHM, is approximately expressed as [133]

$$\theta_c = \left(\frac{Z_1 Z_2 e^2}{2\pi\epsilon_0 E_1 d} \right)^{\frac{1}{2}}, \tag{6.2}$$

where e and ϵ_0 represent the elementary charge and the permittivity of vacuum, respectively. d is the average distance between atoms in the rows. In case of a Pd target and $^{15}N^{2+}$ ion incidence with an energy of 6.385 MeV around the <100> axis, θ_c is derived to be 1.58 °. One can know whether the system is under the ion channeling condition or not from the change of RBS counts by sweeping the incident angle. When the channel the ions are passing though is a plane, it is called the plane channeling, and when the channel is an axis, it is called the axis channeling.

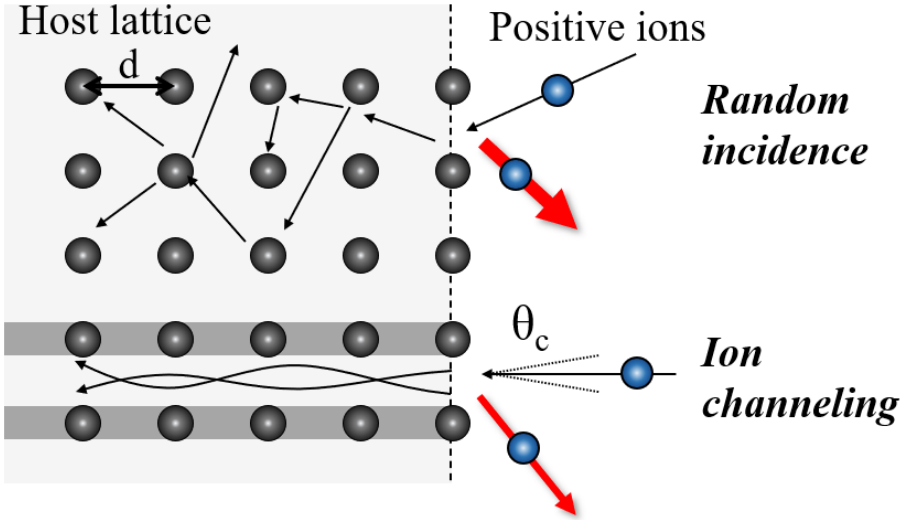

Figure 6.2: Schematic illustration of ion channeling.

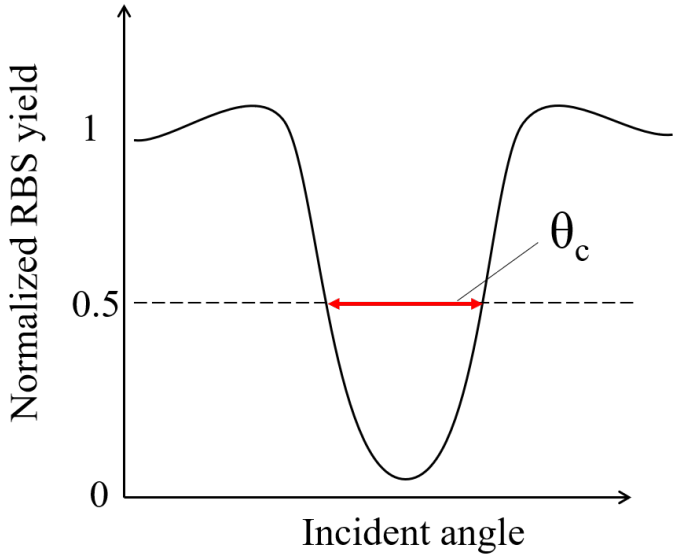

Figure 6.3: Schematic illustration of RBS yield according to the angle between the incident beam and a certain crystalline axis.

6.1.1.3 Channeling NRA

Under the ion channeling condition, nuclear reaction between the injected $^{15}N^{2+}$ ions and the hydrogen atoms hidden behind the host lattice in materials does not occur. In contrast, the hydrogen atoms in the channels react with the incident $^{15}N^{2+}$. Thus, the simultaneous measurement of RBS and NRA with sweeping the angle of ^{15}N ions makes it possible to determine the hydrogen sites in materials. The information of the ion channeling is obtained by RBS and the hydrogen atoms are detected by NRA, as schematically shown in Figure 6.4. Furthermore, one can comprehensively evaluate the lattice location of hydrogen by means of multiple axis channelings such as <100>, <110> and <111> because NRA does not restrict the incident angle of the beam. We would like to emphasize that the depth distribution is also obtained by scanning the energy of $^{15}N^{2+}$ ions thanks to the resonant reaction of $^{1}H(^{15}N, \alpha\gamma)^{12}C$. The conventional channeling NRA has not depth resolution due to using the non-resonant reaction of $D(^{3}He,p)\alpha$ [134, 135, 19]. Quantitative determination of hydrogen sites with a depth resolution of nm level is only possible for the channeling NRA with the resonant reaction of $^{1}H(^{15}N$. In particular, this is necessary to investigate the hydrogen property beneath a subsurface.

Figure 6.5 shows expected typical data of the simultaneous measurement of RBS and NRA around the incident angle <100> for fcc metal targets. The dip in the RBS yield represents the ion channeling. Since hydrogen atoms in the O site are hidden behind the host lattice, it is expected that the NRA yield has a dip as well as the RBS yield. On the other hand, if the hydrogen atoms are in T sites, which are in the <100> axis and the {100} plane channels, the NRA yield is expected to increase under the channeling condition. If hydrogen atoms are located at off-centered positions deviating from the center of O or T sites, there is a splitting in the NRA dip in principle as illustrated in Figure 6.6 [134]. Considering the critical angle is less than a few degrees, the apparatus with accurate rotation mechanism with an angle resolution of ~0.1° is necessary to realize the channeling NRA.

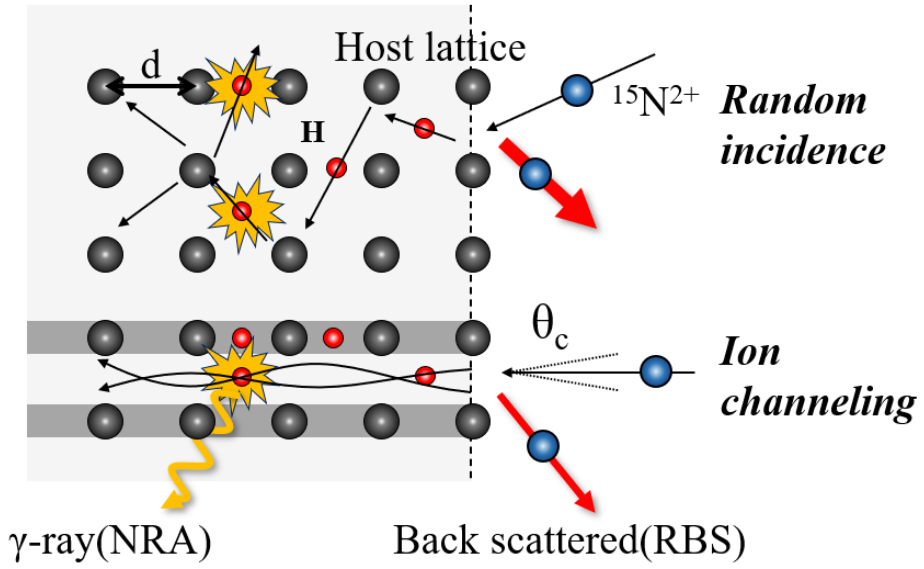

Figure 6.4: Schematic picture of channeling NRA with $^{1}H(^{15}N, \alpha\gamma)^{12}C$. θ_c and d represent the critical angle and the average distance between host atoms in the rows, respectively. The information of the ion channeling is obtained by RBS, and the hydrogen is detected by NRA.

6.1.2 Development of channeling NRA

To realize the channeling NRA, a three-axis rotation mechanism capable to precisely control the direction of the sample correctly and arbitrarily is needed. We designed and developed the manipulator with a three-axis rotation mechanism and transfer mechanism in each of the three axial directions with θ, ω and ϕ as schematically illustrated in Figure 6.7. The rotation angle is controlled by the number of pulses imputed into a motor through the LabVIEW control program. Figure 6.9 shows the sample stage we developed with a two-rotational-axis of ω and ϕ. The stainless steel shaft fixed with the sample holder is held by two ball-bearings on one side for the rotation of ϕ. Distortion by the thermal contraction in the rotational mechanism must be avoided to perform the experiment at high and low temperature as well as in situ sample preparation. Thus, we thermally separated the sample holder by a ceramic heater from the sample stage with the rotation mechanism. The temperature change is limited in the sample holder, as the sample holder is cooled by bundled Cu wires connected to the cold end of a GM refrigerator down to 50 K, and is heated up to 600 K by the ceramic heater. The temperature of the sample is measured by a thermocouple.

γ-ray and backscattered ions are measured by a BGO scintillator and a Si semiconductor detector. The whole apparatus is shown in Figure 6.8. The apparatus is equipped with two BGO scintillators at the both sides and a SSD in front. Two slits of 2 mm square at a distance of 1 m are introduced in front of a sample in the beam line, which ensures the angle spread of $^{15}N^{2+}$ ions within 0.12 °. The amount of implanted $^{15}N^{2+}$ ions is counted by the Cu wire between the slits and the sample, with which the RBS and NRA yields are normalized. The rotation of θ angle is operated by the rotation of the manipulator. Since the experiment is performed in the ultra-high vacuum chamber with a base pressure below 3×10^{-6} Pa, possible influence of ice condensation on the sample surface can be neglected. In situ sample preparations such as the surface cleaning by annealing and gas exposures and the hydrogenation by hydrogen gas exposure and hydrogen ion implantation are possible.

6.1.3 Sample

The channeling NRA requires a monocrystalline specimen in good quality. A bulk of Pd(100) single crystal was used in the present experiment. The hydrogenation was performed by the hydrogen ion implantation with an energy of 2 keV and an incident angle of 45 °. Figure 6.10 and Figure 6.11 show the hydrogen depth distributions obtained by NRA at 50 K with a random incidence and calculated by TRIM. The depth profiles are consistent between them, showing that the hydrogenation of the specimen was confirmed.

6.1.4 Results and discussion

6.1.4.1 Two-dimensional RBS mapping

Figure 6.12 shows the raw RBS spectra for Pd(100) obtained at 50 K by $^{15}N^{2+}$ beams with an energy of 6.42 MeV for the angles corresponding to the random and <100> incidences, where the horizontal axis corresponds to the energy of the backscattered ions. The rising edge of the signals around the 400th channel represents the Rutherford back scattering near the surface. The yield of the backscattered ions is substantially reduced for the <100> incidence due to the ion channeling effect. By sweeping the two angles of θ and ϕ and summing up the RBS counts in the ROI around the 400th channel illustrated in Figure 6.12, two-dimensional RBS mapping was obtained as shown in Figure 6.13, where a dotted line represents a line scan angle of the channeling NRA as mentioned

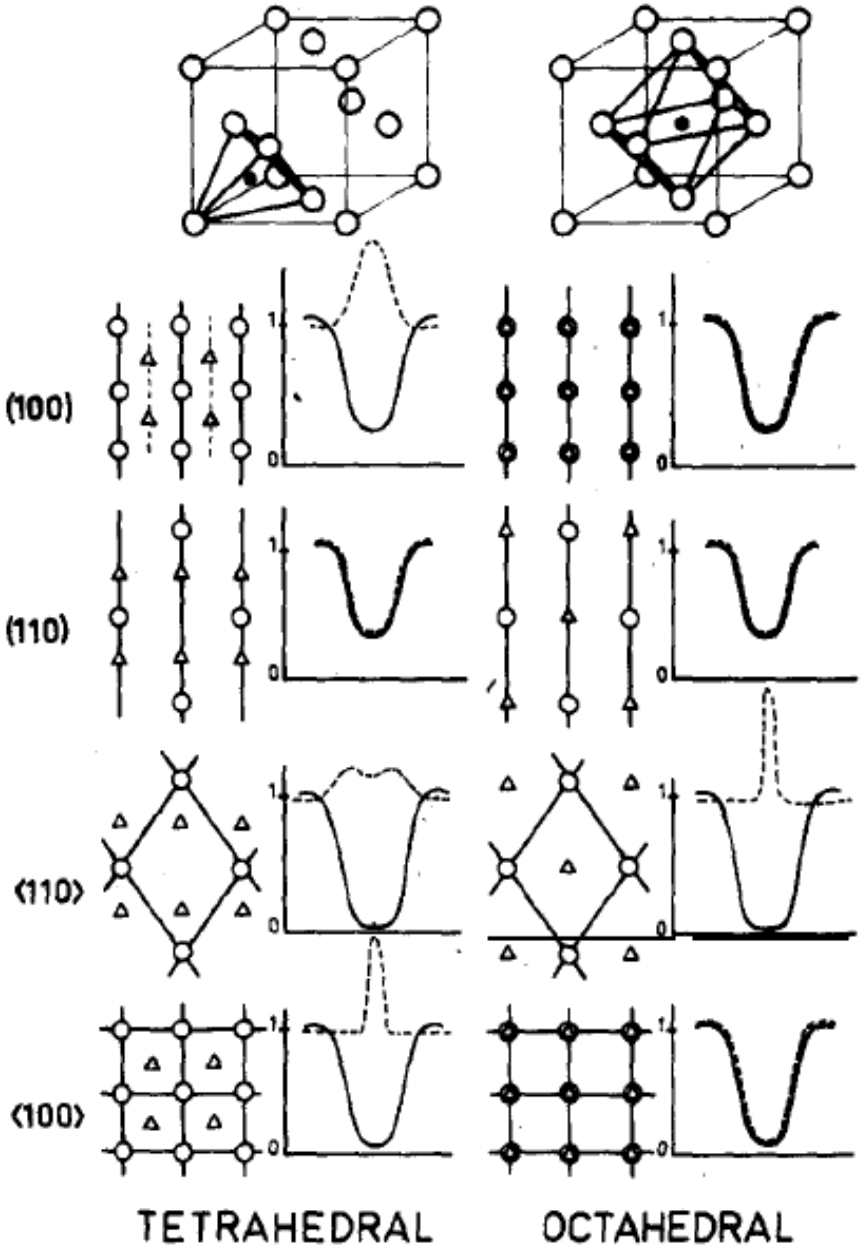

Figure 6.5: Relative position of T and O sites in fcc metals and expected curves of corresponding RBS and NRA yields. Solid and dotted lines represent RBS and NRA yields, respectively. <> and {} denote axis and plane channeling, respectively.

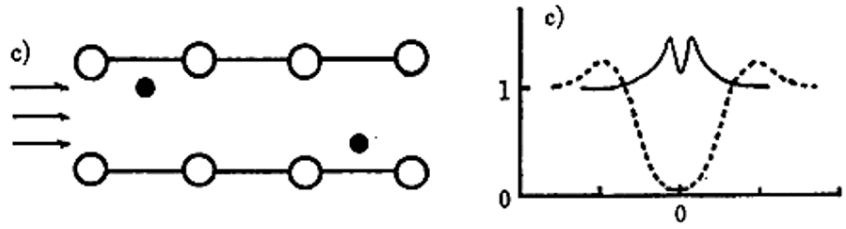

Figure 6.6: Expected data of channeling NRA when hydrogen atoms are located at off-centered positions [136].

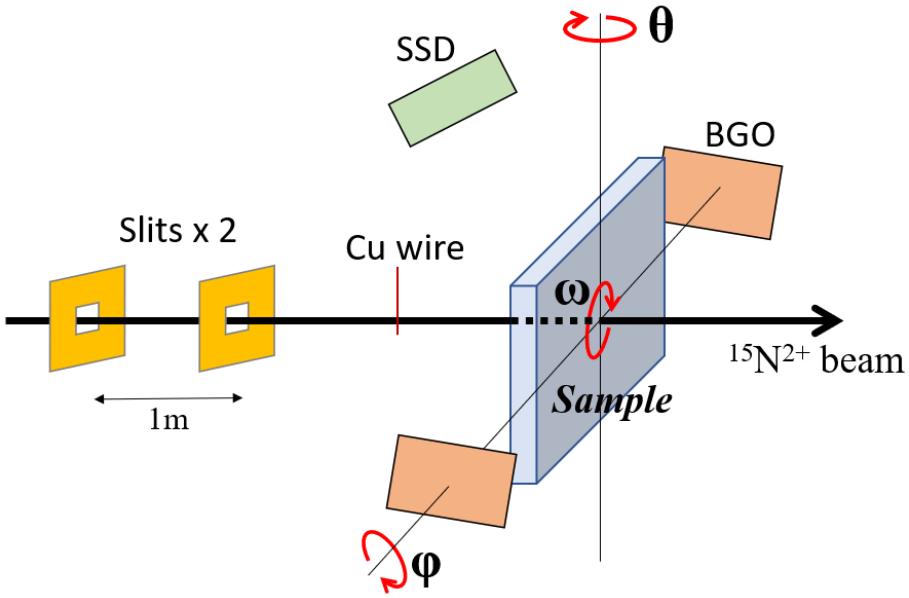

Figure 6.7: Schematic illustration of the channeling NRA apparatus.

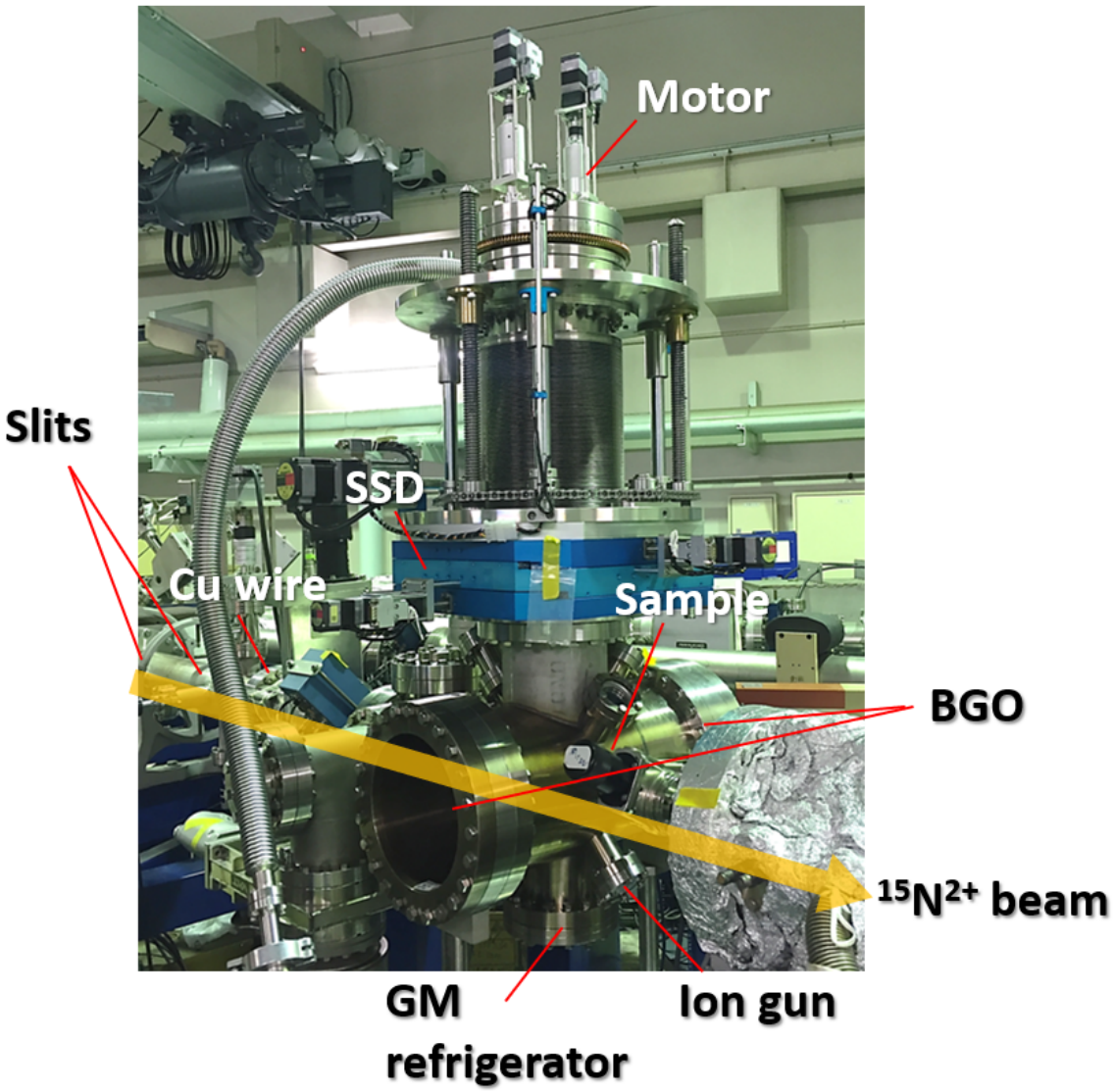

Figure 6.8: Channeling NRA apparatus developed in MALT. The rotation of θ is operated by rotating the manipulator.

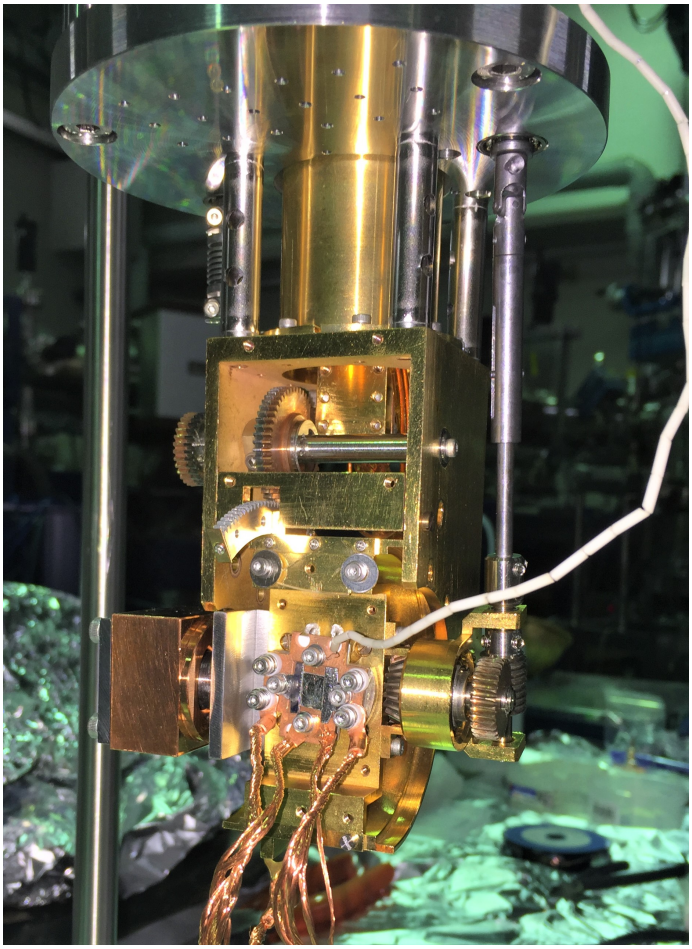

Figure 6.9: Sample stage with the two-axis rotation mechanism of ω and ψ.

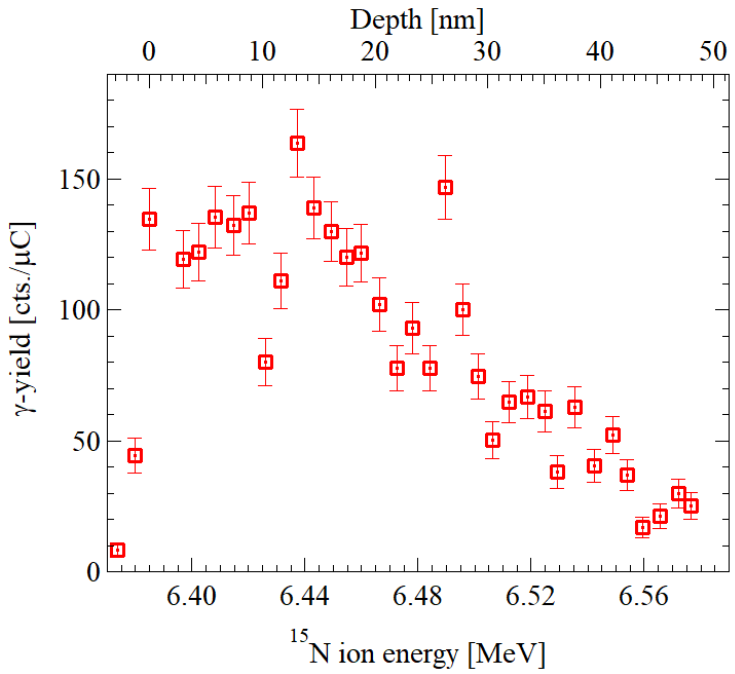

Figure 6.10: Hydrogen depth distribution obtained by NRA of the random incidence at 50 K for the Pd(100) bulk after the hydrogen ion implantation with an energy of 2 keV and at an incident angle of 45 °.

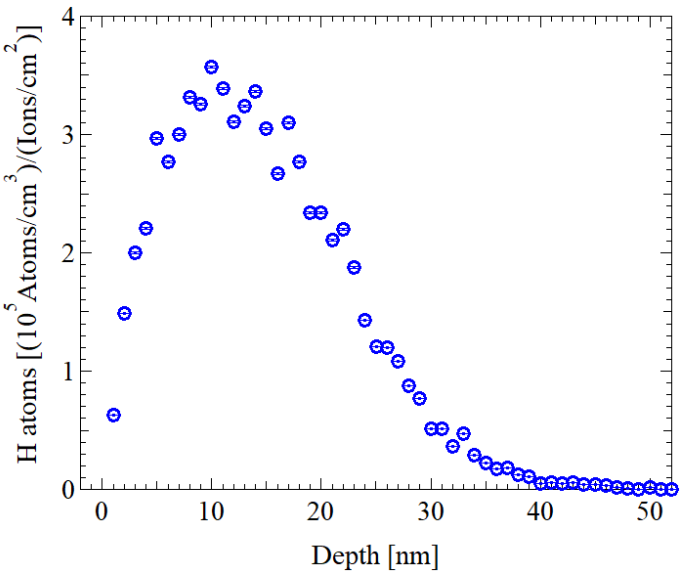

Figure 6.11: Hydrogen depth distribution calculated by TRIM for hydrogen ion implantation with an energy of 2 keV and at an incident angle of 45 °.

later. The <100> axis channeling as well as the {100} and {110} plane channelings are confirmed. Figure 6.14 show the line profiles along the angle θ at $\phi = 0, 1, 2$ and 3 °. The decrease in the RBS yield is the largest for the <100> axis channeling, and that for {110} plane channeling is larger as compared to the {100} the plane channeling. This is because the inter planar distance for the {110} planes (2.7505 Å) is longer than that for the {100} planes (1.9449 Å). The half width for the <100> axis channeling is derived to be ∼2.2 °, which is in agreement with the theoretical prediction of $\theta_c = 1.58°$.

6.1.4.2 Site determination by channeling NRA

After the hydrogenation by the hydrogen ion implantation with an energy of 2 keV and an incident angle of 45 °, the channeling NRA along the line represented by a dotted line in Figure 6.13 was performed for the specimen at 50 K and an incident energy of 6.420 MeV, which corresponds to the probing depth of 9 nm, as shown in Figure 6.15. The hydrogen composition ratio (H/Pd) is derived to be ∼0.2 from the NRA yield of the random incidence. As can been seen, the NRA yield was reduced in accordance with the <100> axis channeling confirmed by the reduction of the RBS yield, implying at least a part of the implanted hydrogen atoms are located at the O sites. Figure 6.16 shows the the channeling NRA result at 50 K and an incident energy of 6.47 MeV corresponding to the probing depth of 21 nm. Apparent differences at 9 nm and 21 nm in the RBS and NRA yields are not recognized, which indicates that the hydrogen lattice location deeper than 9 nm from the surface is the same. Figure 6.17 shows the result of the channeling NRA at 50 K and an incident energy of 6.420 MeV for the specimen after the subsequent heating up to 80 K. As compared to the result before the heating in Figure 6.15, the NRA yield around the axis of <100> was reduced. These results experimentally revealed that the hydrogen atoms implanted at 50 K are initially located in the T sites partially as well as in the O sites, and the hydrogen atoms move from the T to O sites by heating up to 80 K. Assuming that all hydrogen atoms are in O sites after the heating, it is revealed that 30 percent of the implanted hydrogen were initially located at T sites after the implantation at 50 K.

This is consistent with the result about hydrogen diffusion evaluated by the resistance relaxation for the PdH_x formed by the hydrogen ion implantation in section 4.3 showing the thermal diffusion from a metastable site to the stable sites above 60 K. It is also revealed that the electronic property characteristic to the PdH_x formed by the hydrogen implantation, which does not show the 50 K anomaly as revealed in secion 5.2.3, is related to the T site occupation. It should be mentioned that the humps in the NRA yield at ∼±1 ° in Figure 6.17 might be related to the hydrogen atoms around Pd vacancies. The TRIM calculation in Figure 6.18 expects Pd vacancies to be formed by the hydrogen implantation and DFT calculation shows Pd vacancy stabilizes the off-centered positions surrounding the vacancy [137].

In contrast, the present result is inconsistent with previous studies analyzing the lattice location of deuterium implanted at 25 K and an energy of 10 keV in a Pd(100) single crystal by channeling NRA with a non-resonant reaction of $D(^3He,p)\alpha$ and showing that implanted deuterium ions are initially located in O sites and move to T site above 80 K [19]. The same tendency was also obtained by heating at 85 K for the PdD_x formed by the deuterium implantation at 25 K with an energy of 15 keV [138]. We speculate that the difference between our result and the previous studies is related to the concentration of Pd vacancies with respect to H(D) atoms. Figure 6.18 and 6.19 show the depth distributions of hydrogen(deuterium) atoms and Pd vacancies calculated by TRIM for hydrogen implantation with an energy of 2 keV at an incident angle of 45 ° and for deuterium implantation with an energy of 10 keV at a normal incidence, respectively. While the ratio of Pd vacancies to

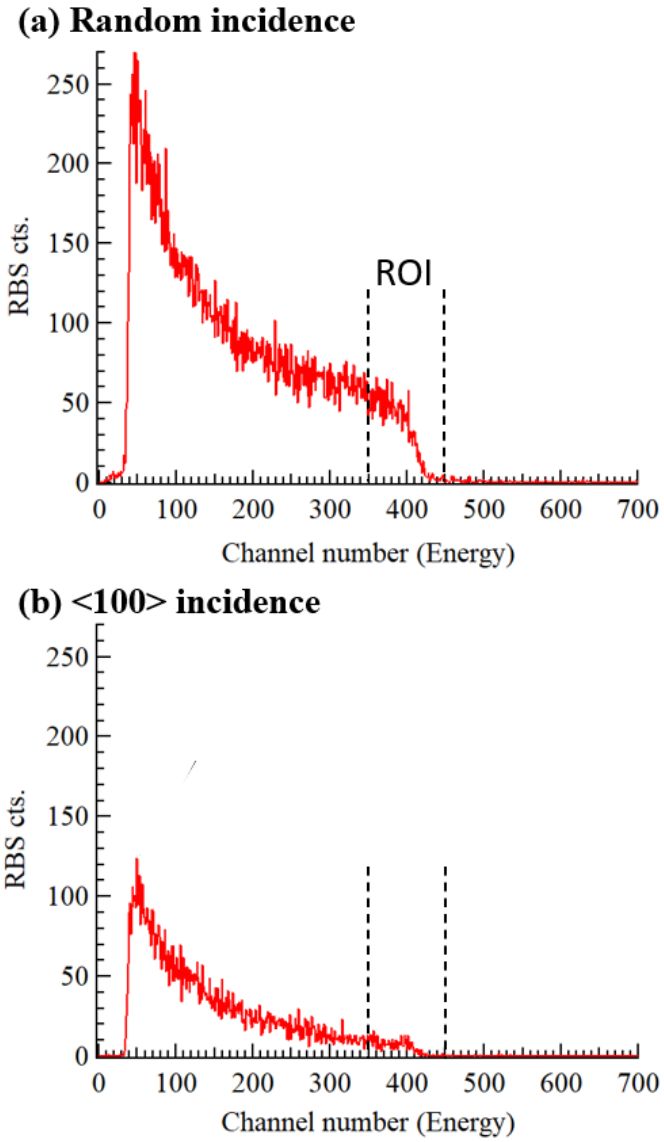

Figure 6.12: Raw RBS spectra for Pd(100) obtained at 50 K by $^{15}N^{2+}$ beams with an energy of 6.420 MeV for the incident angles corresponding to (a) the random and (b) the <100> axis, respectively.

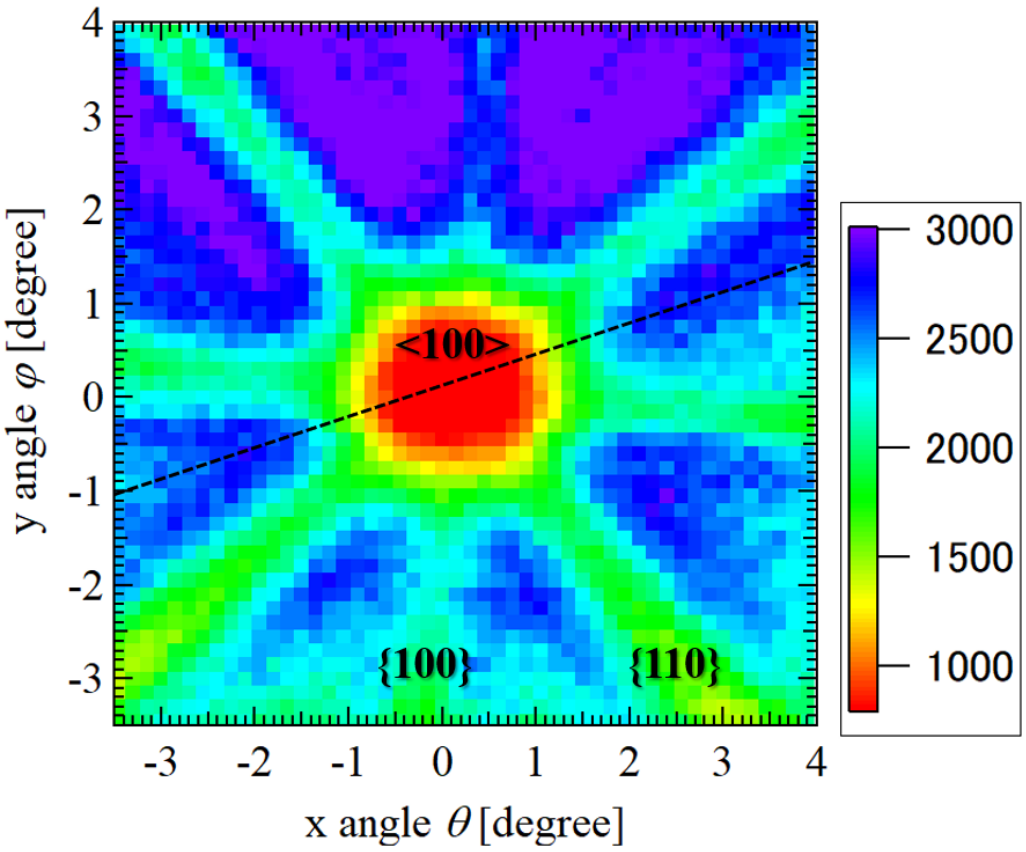

Figure 6.13: Two-dimensional RBS mapping at 50 K derived from the RBS spectra by $^{15}N^{2+}$ beam with an energy of 6.420 MeV according to the two angles θ and ϕ. The dotted line represents a scanning line of channeling NRA in Figures 6.15, 6.16 and 6.17.

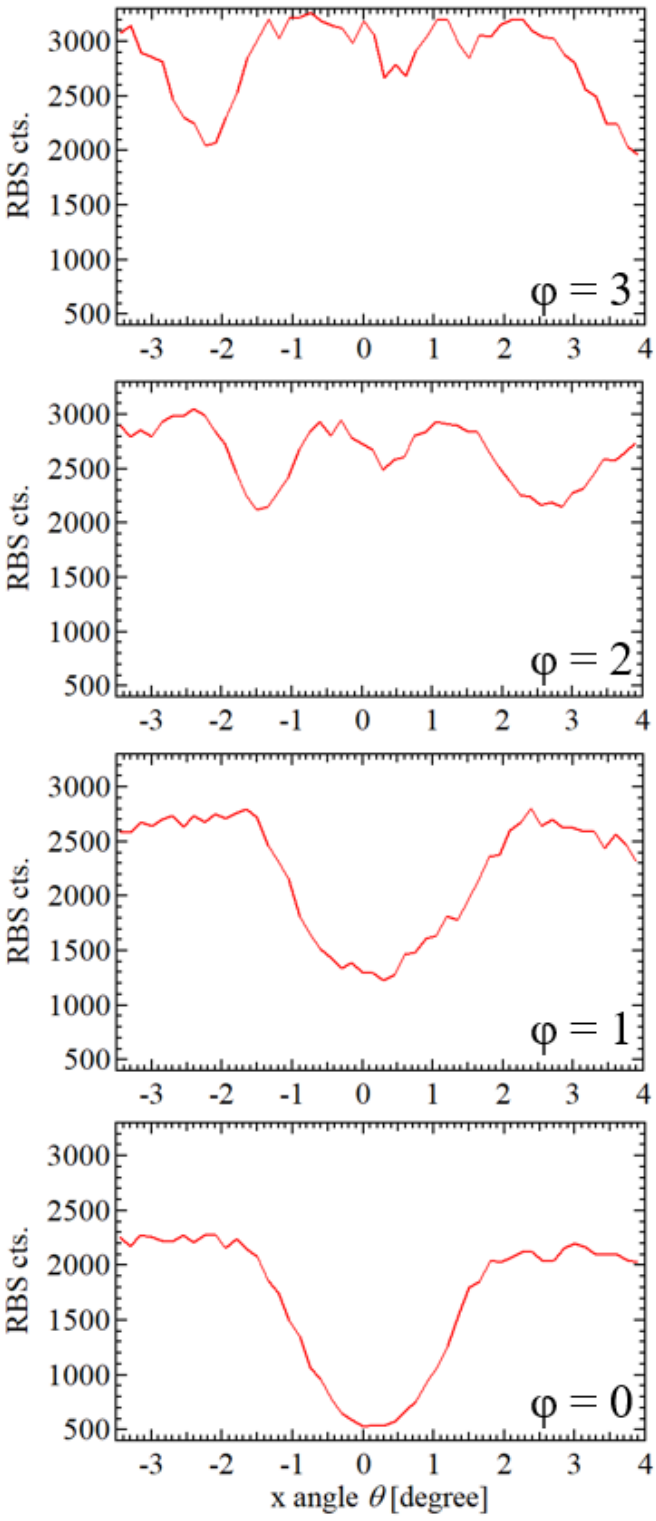

Figure 6.14: Line profiles in the two-dimensional RBS mapping along the angle θ at $\phi = 0, 1, 2$ and 3 °.

hydrogen(deuterium) atoms is derived to be 7.6×10^{-9} for the hydrogen implantation, that is derived to be 1.6×10^{-7} for the deuterium implantation, which means that the number of Pd vacancies per one hydrogen(deuterium) is 20 times larger in case of the deuterium implantation. These results implied that the lattice location of hydrogen in metal hydrides can be affected and controlled by lattice vacancies, leading to the control of physical properties of (metastable) metal hydrides.

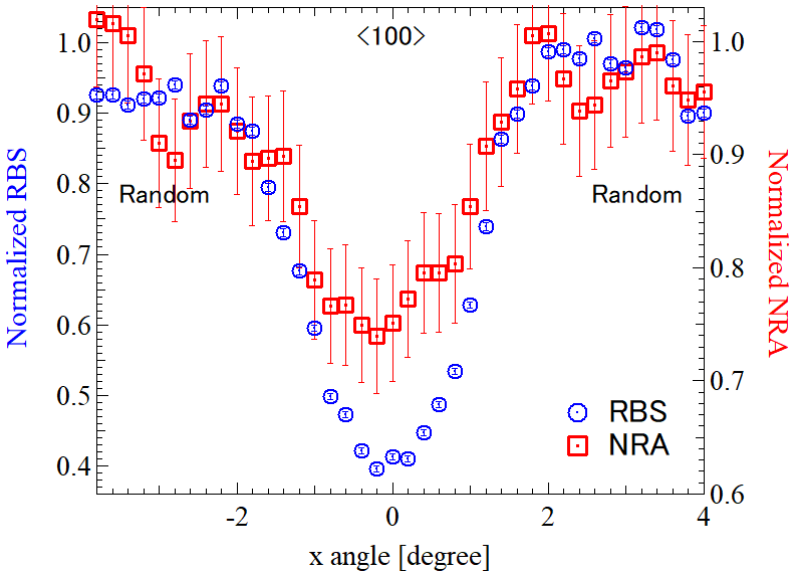

Figure 6.15: RBS and NRA yields simultaneously obtained by $^{15}N^{2+}$ ions with an incident energy of 6.420 MeV at 50 K according to the incident angle around the <100> axis for the Pd(100) bulk hydrogenated by the hydrogen ion implantation at 50 K. The hydrogen composition ratio is derived to be ~0.2.

6.1.5 Conclusion

The apparatus for the simultaneous measurement of RBS and NRA was developed. Performing the channeling NRA for the Pd(100) bulk hydrogenated by the hydrogen ion implantation at 50 K with an energy of 2 keV, it was revealed that a part of the implanted hydrogen atoms are located in T site at 50 K and they move to O sites by heating up to 80 K. The channeling NRA with the resonant reaction $^{1}H(^{15}N, \alpha\gamma)^{12}C$ is a versatile method which makes it possible to determine the hydrogen lattice location with a depth resolution of nm order in materials.

6.2 Inelastic neutron scattering

Surface effects including lattice relaxation and charge transfer have a possibility to realize a metastable T site occupation of hydrogen in Pd. It was revealed from a neutron diffraction study that some of D atoms are accommodated at the T site near the surface of PdD_x nanoparticles, which is also supported by a theoretical calculation including the lattice relaxation and charge transfer. However, nanoparticles have two competing effects; while the dangling-bond nature tends to expand the subsurface lattice, the surface tension induces compressive strain. To understand the hydrogen absorption property and electrical property at a subsurface region, we need to distinguish these effects.

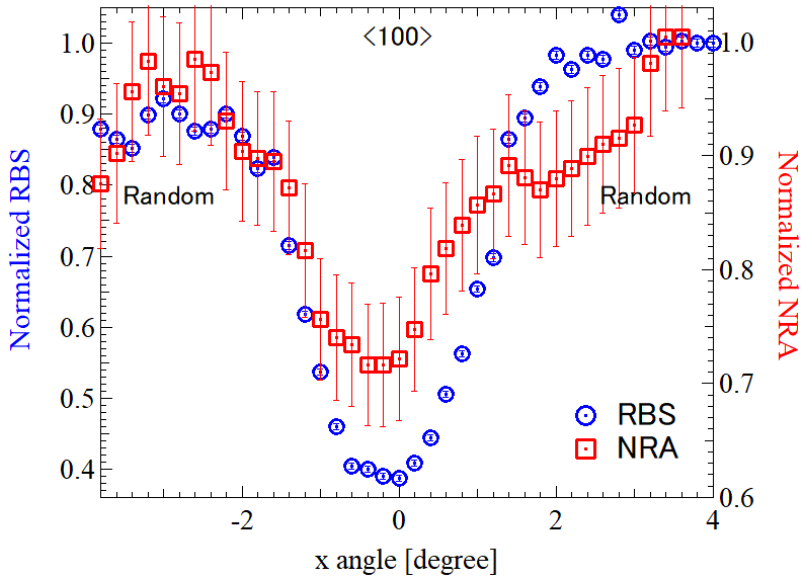

Figure 6.16: RBS and NRA yields simultaneously obtained by $^{15}N^{2+}$ ions with an incident energy of 6.467 MeV at 50 K according to the incident angle around the <100> axis for the specimen of $PdH_{0.2}$.

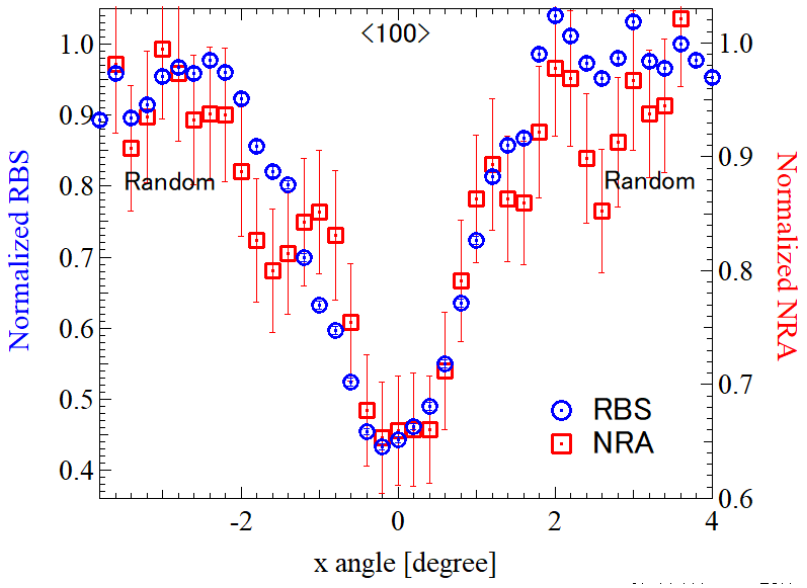

Figure 6.17: RBS and NRA yields simultaneously obtained by $^{15}N^{2+}$ ions with an incident energy of 6.420 MeV at 50 K according to the incident angle around the <100> axis for the specimen of $PdH_{0.2}$ after the subsequent heating up to 80 K.

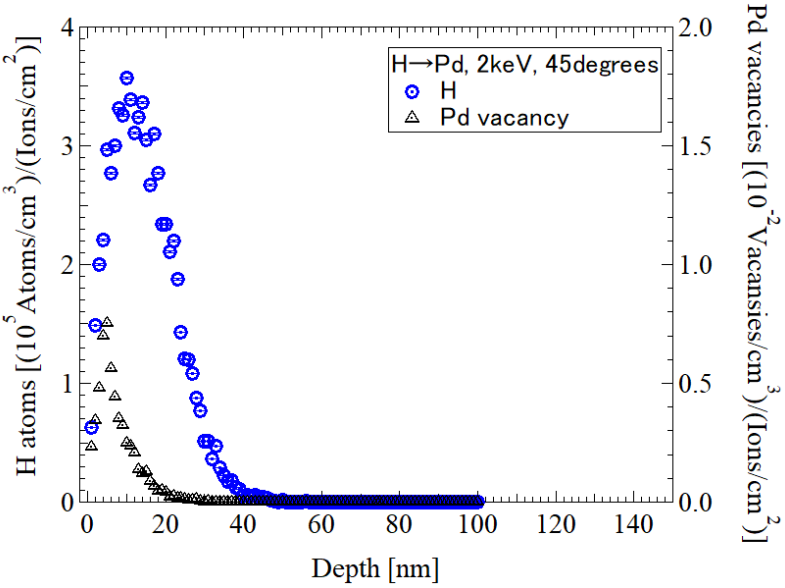

Figure 6.18: Depth distributions of hydrogen atoms and Pd vacancies calculated by TRIM for hydrogen implantation with a energy of 2 keV at a incident angle of 45 °.

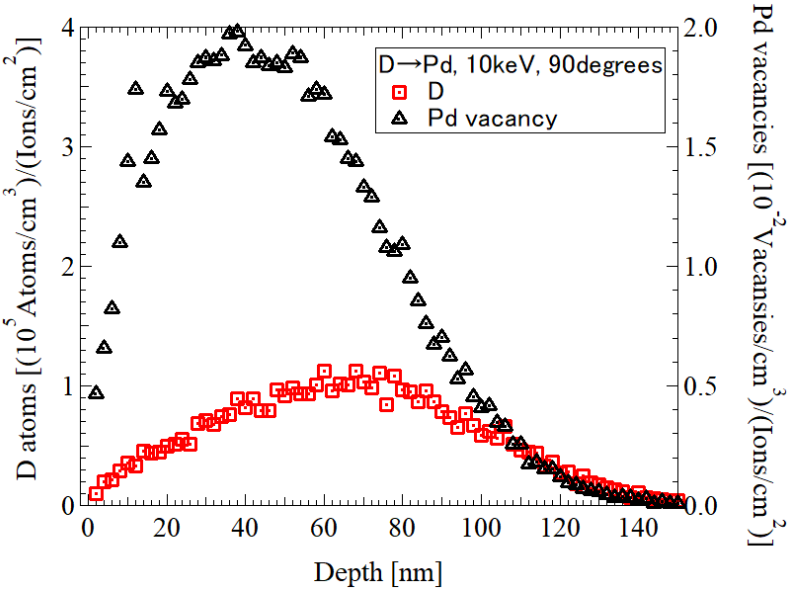

Figure 6.19: Depth distributions of deuterium atoms and Pd vacancies calculated by TRIM for deuterium implantation with a energy of 10 keV at a normal incidence, respectively.

Compared with nanoparticles, only the surface dangling-bond effect can be examined for ultrathin films, where the ratio of the flat subsurface region to the total volume is enough large. There has been no convincing studies about hydrogen vibrational states near a clean two-dimensional surface. INS experiments have not been performed for nanofilms so far. That is because a problem of signal strength is predestined to observe the hydrogen vibration spectra by inelastic neutron scattering INS. In this experiment, we investigated H vibration spectra in Pd nanofilms by means of INS at BL-01 in J-PARC taking advantage of the high flux and the effective detection. Vibration spectra are profitable information to to clarify the hydrogen state since they reflect the position of hydrogen atoms and local structural distortion around hydrogen atoms.

6.2.1 Sample

An Al film with a thickness between 10 to 12 μm was adopted as a substrate because the neutron scattering cross section for Al is small compared with other elements as shown by Table 3.1. The specimens used in the present experiment are Pd films with a thickness of 8 nm deposited on both sides of a substrate by magnetron sputtering at room temperature. Figure 6.20 shows two-dimensional XRD patterns with an x-ray wavelength of 1.5418 Å of CuKα for an Al substrate with and without Pd a 8-nm-thick Pd film. The θ-2θ scans of them are displayed in Figure 6.21 by integrating the two-dimensional patterns. The diffraction spots of Al(111) and (200) and the Debye-Scherrer rings corresponding to them are seen for the Al substrate. For the Pd(8nm)/Al, the diffraction peaks of Pd(111) and (200) in addition to Al(200) and the Debye-Scherrer rings corresponding to them can been seen, showing that the deposited Pd film is polycrystalline. Scherrer's equation with the Scherrer constant of 0.9 gives an average grain size of 12.4 nm as obtained from the Pd(111) peak.

45 films with a diameter of 96 mm of Pd(8nm)/Al/Pd(8nm) were fabricated, and the total amount of deposited Pd is 65 mg. The specimens were rolled and mounted in a cylindrical sample cell made of Al with a diameter of 19 mm and a thickness of 0.25 mm, which is connected to the gas delivery system as shown in Figures 6.22 and 6.23.

6.2.2 Results and discussion

In this experiment, the sample was hydrogenated in situ by hydrogen gas exposure of 200 Pa and 0.1 MPa at 200 K after the degassing at 373 K in vacuum below 10^{-3} Pa. From the amount of the absorbed gas and change of the intensity of neutron inelastic scattering, the hydrogen atomic ratio x was estimated to be 0.19 and 0.73, respectively. INS was performed at 10 K in vacuum before and after the hydrogenations. The measuring time was 24, 55 and 24 h for the sample with x of 0, 0.19 and 0.73, respectively. The spectrum was acquired for incident energies (E_i) of 101, 168 and 332 meV.

Figures 6.24 show contour maps of the dynamical structure factor $S(Q,\omega)$ (Q-E map) for the sample before the hydrogenation obtained with E_i = 101, 168 and 332 meV. $S(Q,\omega)$ is a normalized scattering intensity described as $S(Q,\omega) = \frac{I(Q,\omega}{N<b>^2}$, where I, N and $< b >$ represent the observed scattering intensity, the number of atoms and an average scattering length per one atom, respectively. The S observed at $Q > 7\text{Å}^{-1}$ is large. These features correspond to the Al and Pd phonons. Figure 6.25 shows Q-E maps for $PdH_{0.73}$ with E_i = 101, 168 and 332 meV at 10 K. The scattering contribution from the Pd films, Al substrates, Al sample cell and instrumental background was subtracted in the data for PdH_x by using the data before the hydrogenation. The orange curve represents the recoil trajectory of $E = \frac{\hbar^2 Q^2}{2m}$, where m is mass of a proton.

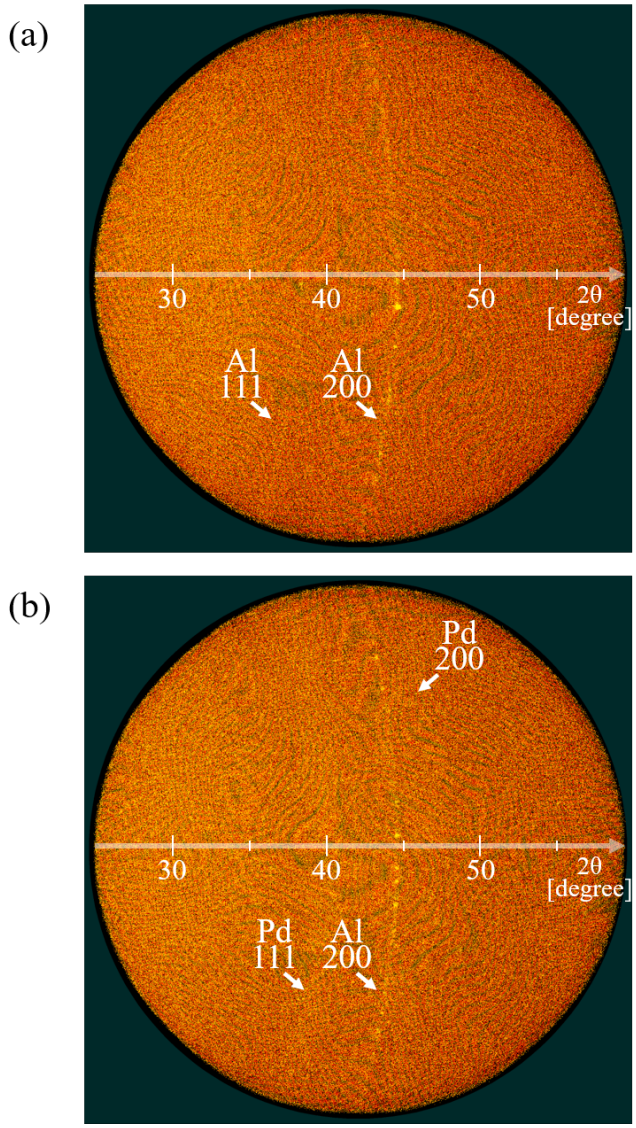

Figure 6.20: Two-dimensional XRD profiles of (a) a Al substrate and (b) a Pd(8nm)/Al film.

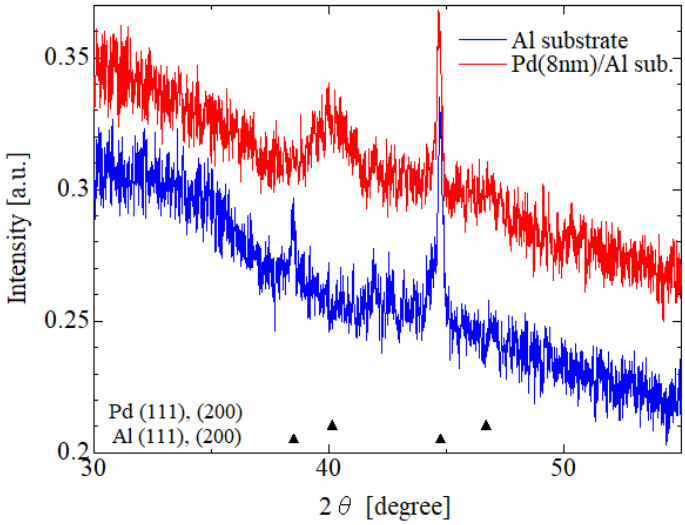

Figure 6.21: θ-2θ XRD patterns for an Al substrate with and without Pd a 8-nm-thick Pd film.

Figure 6.22: Rolled specimens of 8(nm)/Al/Pd(8nm) used in the INS experiment.

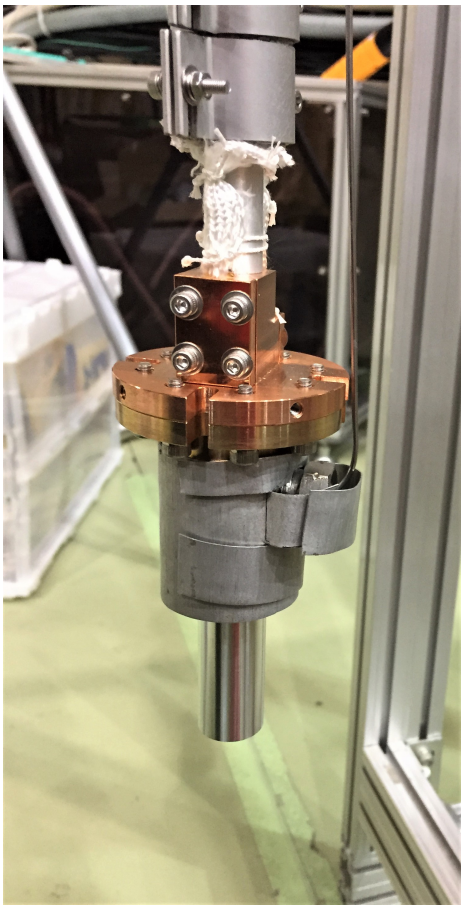

Figure 6.23: A cylindrical cell made of Al in which the rolled specimens are mounted.

INS spectra are obtained by collecting the data along the recoil trajectory to avoid the contribution from the phonons of Pd Al and Pd. Figures 6.26, 6.27 and 6.28 show the INS spectra for the $PdH_{0.19}$ and $PdH_{0.73}$ nanofilms. The spectra clearly exhibited peaks around 60 and 135 meV for both $PdH_{0.19}$ and $PdH_{0.73}$. These values correspond to the first and second H vibration modes in the O site [15, 30, 111, 112, 113], which means that the hydrogen atoms are located in the O site similarly to PdH_x bulk. The first and second vibration energies in $PdH_{0.73}$ were shifted by 3 and 5 meV to the lower energy as compared to $PdH_{0.19}$, respectively. It is conceivable that the energy shift originates from the lattice expansion by hydrogen absorption. This result is consistent with the result of hydrogen diffusion showing that the diffusion rate depends on the hydrogen concentration reflecting the energy levels in section 4.2. Compared with hydrogen vibrations in Pd_x bulks and nanoparticles, the vibration spectra below 100 meV in the nanofilms in the present experiment are similar to those in nanoparticles, as can be seen in Figure 6.26, 6.27 and 6.28. In contrast, looking at a high energy region, no additional peaks above 160 meV were observed within our experimental accuracy for $PdH_{0.73}$ unlike PdH_x nanoparticles, which have hydrogen atoms partially in T site. These results indicate that hydrogen is located only in the O site near the two-dimensional surface similarly to that in bulk, but its vibration spectrum of O site is similar to that in nanoparticles. It is revealed that the vibrational state of hydrogen near the surface is unique and has both characteristics of bulk and nanoparticle.

6.2.3 Conclusion

The spectra of the hydrogen vibration near the flat surface in Pd were successfully obtained by INS. The This is the first observation of the hydrogen vibration near a two-dimensional surface. The energy spectra corresponding to the first and second hydrogen vibration modes in O site were observed. It is revealed that the vibrational state of hydrogen near the flat surface is unique and has both characteristics of bulk and nanoparticle.

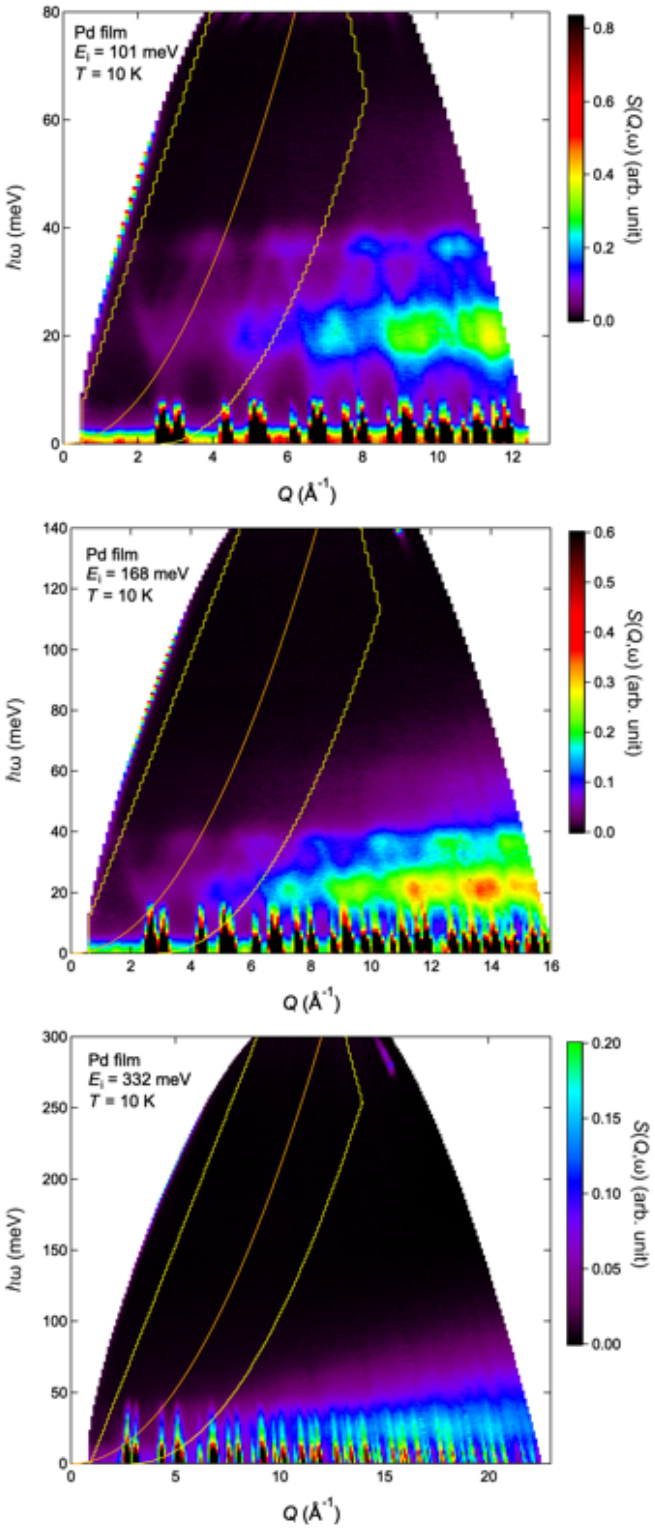

Figure 6.24: Dynamical structure factors $S(Q, \omega)$ as functions of energy $\hbar\omega$ and momentum transfer Q for 8-nm-thick Pd films on Al substrates before the hydrogenation obtained with E_i = 101, 168 and 332 meV.

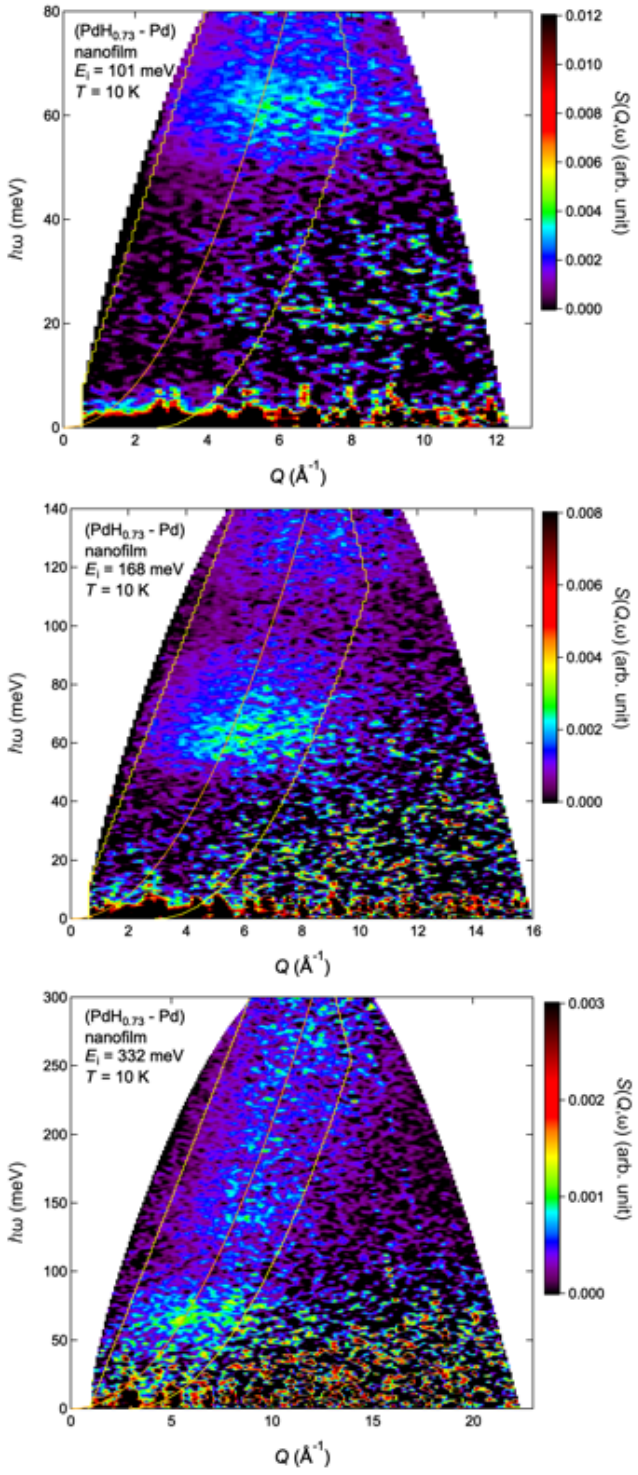

Figure 6.25: Dynamical structure factors $S(Q, \omega)$ as functions of energy $\hbar\omega$ and momentum transfer Q for 8-nm-thick $PdH_{0.73}$ films on Al substrates obtained with E_i = 101, 168 and 332 meV. The scattering contribution from the Pd films, Al substrates, Al sample cell and instrumental background was subtracted by using the data before the hydrogenation in Figure 6.24.

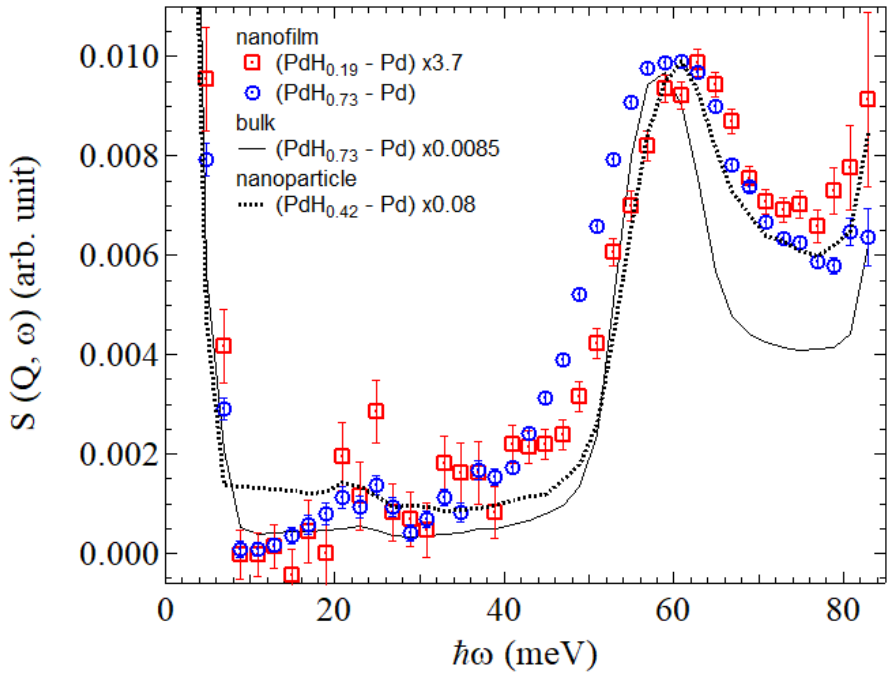

Figure 6.26: INS spectra along the recoil trajectory at 10 K for the $PdH_{0.19}$ and $PdH_{0.73}$ nanofilms with E_i = 101 meV. The spectra for $PdH_{0.73}$ bulks and $PdH_{0.42}$ nanoparticles are also shown [15].

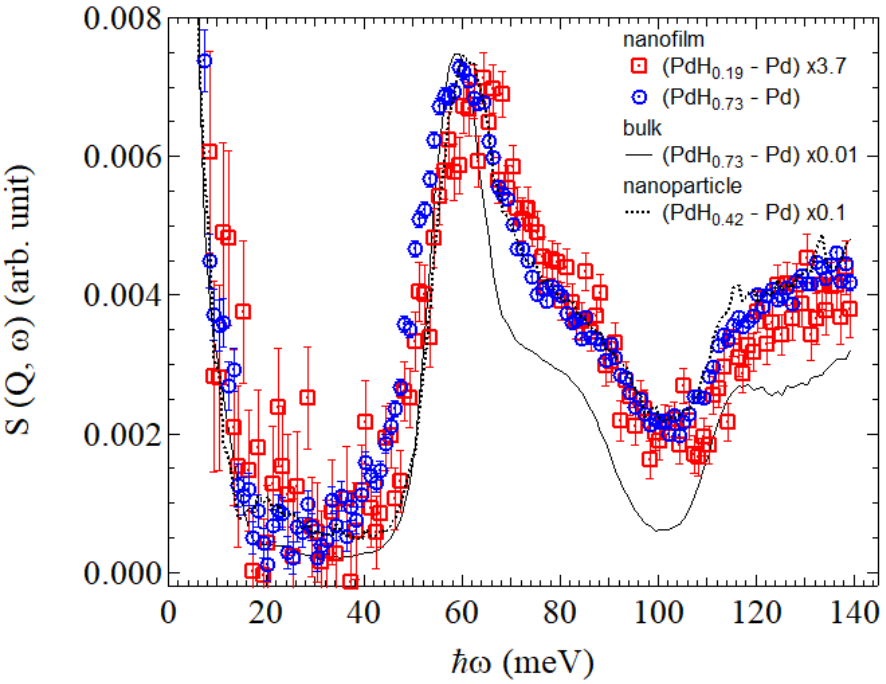

Figure 6.27: INS spectra along the recoil trajectory at 10 K for the $PdH_{0.19}$ and $PdH_{0.73}$ nanofilms with E_i = 168 meV. The spectra for $PdH_{0.73}$ bulks and $PdH_{0.42}$ nanoparticles are also shown [15].

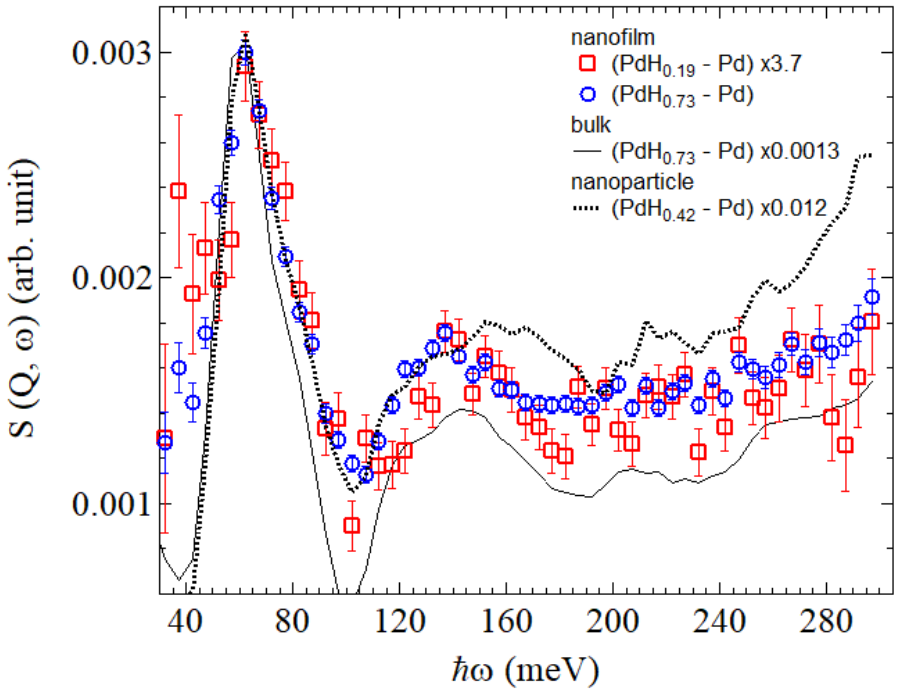

Figure 6.28: INS spectra along the recoil trajectory at 10 K for the $PdH_{0.19}$ and $PdH_{0.73}$ nanofilms with E_i = 332 meV. The spectra for $PdH_{0.73}$ bulks and $PdH_{0.42}$ nanoparticles are also shown [15].

Chapter 7

Summary

The present thesis investigated the hydrogen diffusion and the electronic transport in Pd. We also investigated the structure and dynamics of Pd hydrides. Knowledge obtained in this thesis is as follows:

1. The hydrogen diffusion between O sites was observed by measuring the resistance change induced by the relaxation from metastable states associated with the 50 K anomaly formed by rapid cooling, and it is revealed that the hydrogen hopping mechanism changes from over-barrier hopping to tunneling from the second vibrationally excited state in the O site to the T site below ~100 K, and subsequently to tunneling between the ground states in the O sites below ~50 K in PdH_x with small x. The tunneling from the excited state enhancing the hydrogen diffusion at the intermediate temperature between 50 and 100 K reflects the potential shape of Pd. Furthermore, the effect of energy matching on quantum tunneling was explicitly observed as the hydrogen concentration dependence and the isotope effect.

2. We also successfully observed the hydrogen diffusion from T to O sites from the relaxation formed by the hydrogen implantation at low temperature. The analysis of the temperate dependence of the hopping rate revealed that hydrogen diffuses thermally above 50 K, via phonon-assisted tunneling between 20 to 50 K, and via tunneling below 20 K. Increase in the hoping rate due to the non-adiabatic effect of hydrogen was observed below 20 K, and the electron-particle coupling constant K was derived to be 0.41. The difference of the activation energies above 50 K between hydrogen and deuterium revealed that potential curvature is larger at the T site than that at the saddle point between the T and O sites.

3. The resistance minimum was observed in Pd films after the hydrogenation. The temperature and concentration dependence was explained by the Kondo effect. In case of the ultrathin film, the behaviors of the Anderson localization due to the randomness in the two-dimensional potential and the Kondo effect induced by the hydrogen absorption coexist. Thickness dependence implied that the size effect suppresses and the surface effect enhances the Kondo effect.

4. The channeling NRA apparatus which determines the hydrogen lattice location in crystals with a depth resolution of nm level was developed and performed for the Pd(100) single crystal hydrogenated by the hydrogen ion implantation at 50 K. It was revealed that a part of the implanted hydrogen atoms are located in T site at 50 K and they move to O sites by heating up to 80 K.

5. The spectra of the hydrogen vibration near the flat surface in Pd were successfully obtained by INS, which showed that the vibrational state of hydrogen in O site beneath the two-dimensional surface is unique and has both characteristics of bulks and nanoparticles.

Acknowledgments

I would like to express my sincere gratitude to Prof. Fukutani for his comments, suggestions and encouragements. Without his guidance and persistent help, this paper thesis would not have been possible. A special gratitude I give to Prof. Wilde for his daily comments and supports. I greatly appreciate the efforts of Prof. Yamamuro and Dr. Kofu through the collaborative work of INS. I wish to thank assistant Prof. Sekiba for his continuous supports on channeling NRA. I would like to express my gratitude to Prof. Hitosugi and assistant Prof. Shimizu for the sample fabrication. Special thanks go to assistant Prof. Ogura and Mr. Kawauchi for their kind instructions with experimental apparatuses. I am also deeply grateful to Dr. Kato for his helpful advice and DFT calculations. I would like to show my appreciation to Prof. Fukai for his fruitful comments about metal hydrides and encouragements. I also express my gratitude to Prof. Makoshi for his incisive comments about resistance anomalies. I thank Prof. Okano, Prof. Kawamura and Prof. Munakata for their constructive comments in seminars. Kind supports by Dr. Ueta, Dr. Ohno, Dr. Asakawa and Dr. Nagatsuka are thankfully acknowledged.

I also would like to show my special gratitude to my parents Hirohiko and Chiyomi and my brother Ryosuke for their moral support. I could not have accomplished the present work without them.

January 2021

Reference

[1] A. Y. J. Kondo: in*Fermi Surface Effects*, ed. J. Kondo and A. Yoshimori (Springer Berlin Heidelberg, Berlin, Heidelberg, 1988), Vol. 77 of *Springer Series in Solid-State Sciences*.

[2] J. Kondo: Physica B+C **126** (1984) 377.

[3] K. Yamada, A. Sakurai, S. Miyazima, and H. S. Hwang: Progress of Theoretical Physics **75** (1986) 1030.

[4] S. Fujii: Journal of the Physical Society of Japan **46** (1979) 1833.

[5] V. G. Storchak and N. V. Prokof'ev: Reviews of Modern Physics **70** (1998) 929.

[6] S. C. Wang and R. Gomer: The Journal of Chemical Physics **83** (1985) 4193.

[7] A. Lee, X. D. Zhu, L. Deng, and U. Linke: Physical Review B **46** (1992) 15472.

[8] L. J. Lauhon and W. Ho: Physical Review Letters **85** (2000) 4566.

[9] C. Z. Zheng, C. K. Yeung, M. M. T. Loy, and X. Xiao: Physical Review Letters **97** (2006) 166101.

[10] M. D'Angelo, R. Yukawa, K. Ozawa, S. Yamamoto, T. Hirahara, S. Hasegawa, M. G. Silly, F. Sirotti, and I. Matsuda: Physical Review Letters **108** (2012) 1.

[11] J. Shi, Y. Zhou, and S. Ramanathan: Nature Communications **5** (2014) 1.

[12] T. Skoskiewicz: Physica Status Solidi (a) **11** (1972) K123.

[13] A. León, E. A. Velásquez, F. J. Torres, J. Mejía-López, and P. Vargas: Journal of Magnetism and Magnetic Materials **498** (2020).

[14] S. Sakuragi, T. Sakai, S. Urata, S. Aihara, A. Shinto, H. Kageshima, M. Sawada, H. Namatame, M. Taniguchi, and T. Sato: Physical Review B - Condensed Matter and Materials Physics **90** (2014) 1.

[15] M. Kofu, N. Hashimoto, H. Akiba, H. Kobayashi, H. Kitagawa, K. Iida, M. Nakamura, and O. Yamamuro: Physical Review B **96** (2017) 054304.

[16] T. Ishimoto and M. Koyama: Journal of Chemical Physics **148** (2018).

[17] S. Ohno, M. Wilde, K. Mukai, J. Yoshinobu, and K. Fukutani: Journal of Physical Chemistry C **120** (2016) 11481.

[18] N. Fukumuro, Y. Fukai, H. Sugimoto, Y. Ishii, H. Saitoh, and S. Yae: Journal of Alloys and Compounds **825** (2020) 153830.

[19] J. P. Bugeat and E. Ligeon: Physics Letters A **71** (1979) 93.

[20] S. M. Myers, P. M. Richards, D. M. Follstaedt, and J. E. Schirber: Physical Review B **43** (1991) 9503.

[21] P. Tripodi, M. C. H. McKubre, F. L. Tanzella, P. A. Honnor, D. Di Gioacchino, F. Celani, and V. Violante: Physics Letters, Section A: General, Atomic and Solid State Physics **276** (2000) 122.

[22] R. Nakayama, M. Maesato, T. Yamamoto, H. Kageyama, T. Terashima, and H. Kitagawa: Chemical Communications **54** (2018) 12439.

[23] M. P. Pitt and E. M. A. Gray: Europhysics Letters **64** (2003) 344.

[24] 宮澤徹也, 間瀬一彦, 飛嶋健佑, and 菊地貴司: 真空・表面科学合同講演会要旨 (2016) 9.

[25] Y. Fukai and H. Sugimoto: Advances in Physics **34** (1985) 263.

[26] T. Skośkiewicz and B. Baranowski: Physica Status Solidi (b) **30** (1968) K33.

[27] B. Stritzker and W. Buckel: Zeitschrift Physik **257** (1972) 1.

[28] 深井有, 田中一英, and 田中裕久: 水素と金属 (1998).

[29] G. Sicking: Berichte der Bunsengesellschaft für physikalische Chemie **76** (1972) 790.

[30] X. Ke and G. J. Kramer: Physical Review B **66** (2002) 184304.

[31] C. P. Flynn and A. M. Stoneham: Physical Review B **1** (1970) 3966.

[32] H. Teichler and A. Seeger: Physics Letters A **82** (1981) 91.

[33] Y. Fukai: *The Metal-Hydrogen System Basic Bulk Properties* (Springer, Berlin, 2005) 2 ed.

[34] T. Holstein: Annals of Physics **8** (1959) 343.

[35] D. Emin, M. I. Baskes, and W. D. Wilson: Physical Review Letters **42** (1979) 791.

[36] T. Regelmann, L. Schimmele, and A. Seeger: Philosophical Magazine B **72** (1995) 209.

[37] K. Yamada: Progress of Theoretical Physics **72** (1984) 195.

[38] J. Kondo: 物性研究 **43** (1984) 50.

[39] P. W. Anderson: Physical Review Letters **18** (1967) 1049.

[40] R. Kadono, J. Imazato, T. Matsuzaki, K. Nishiyama, K. Nagamine, T. Yamazaki, D. Richter, and J.-M. Welter: Physical Review B **39** (1989) 23.

[41] G. M. Luke, J. H. Brewer, S. R. Kreitzman, D. R. Noakes, M. Celio, R. Kadono, and E. J. Ansaldo: Hyperfine Interactions **64** (1990) 721.

[42] G. M. Luke, J. H. Brewer, S. R. Kreitzman, D. R. Noakes, M. Celio, R. Kadono, and E. J. Ansaldo: Physical Review B **43** (1991) 3284.

[43] O. Hartmann, E. Karlsson, E. Wäckelgrd, R. Wäppling, D. Richter, R. Hempelmann, and T. O. Niinikoski: Physical Review B **37** (1988) 4425.

[44] E. Karlsson, R. Wäppling, S. W. Lidström, O. Hartmann, R. Kadono, R. F. Kiefl, R. Hempelmann, and D. Richter: Physical Review B **52** (1995) 6417.

[45] Y. Fukai: Japanese Journal of Applied Physics **23** (1984) L596.

[46] W. G. Baber: Proceedings of the Royal Society of London. Series A - Mathematical and Physical Sciences **158** (1937) 383.

[47] J. Appel: Philosophical Magazine **8** (1963) 1071.

[48] W. J. D. Haas, J. D. Boer, and G. V. D. Berg: Physica **34** (1934) 1115.

[49] 山田耕作: **電子相関** (2000).

[50] J. Kondo: Progress of Theoretical Physics **32** (1964) 37.

[51] F. D. . M. J. P. Franck and D. L. . Martin: Proceedings of the Royal Society of London. Series A. Mathematical and Physical Sciences **263** (1961) 494.

[52] P. W. Anderson: Physical Review **109** (1958) 1492.

[53] 高. 長岡洋介, 安藤恒也: **局在・量子ホール効果・密度波** (2000).

[54] E. Abrahams, P. W. Anderson, D. C. Licciardello, and T. V. Ramakrishnan: Physical Review Letters **42** (1979) 673.

[55] S. ichi Kobayashi, F. Komori, Y. Ootuka, and W. Sasaki. In T Dependence of Resistivity in Two-Dimensionally Coupled Fine Particles of Cu, 1980.

[56] F. Hubbard Horn, W. T. Ziegler, F. Hubbard Horn, and W. T. Ziegler: Journal of the American Chemical Society **69** (1947) 2762.

[57] N. W. Ashcroft: Physical Review Letters **21** (1968) 1748.

[58] N. W. Ashcroft: Physical Review Letters **92** (2004) 1.

[59] A. P. Drozdov, M. I. Eremets, I. A. Troyan, V. Ksenofontov, and S. I. Shylin: Nature **525** (2015) 73.

[60] M. Einaga, M. Sakata, T. Ishikawa, K. Shimizu, M. I. Eremets, A. P. Drozdov, I. A. Troyan, N. Hirao, and Y. Ohishi: Nature Physics **12** (2016) 835.

[61] E. Snider, N. Dasenbrock-Gammon, R. McBride, M. Debessai, H. Vindana, K. Vencatasamy, K. V. Lawler, A. Salamat, and R. P. Dias: Nature **586** (2020) 373.

[62] J. N. Huiberts, R. Griessen, R. J. Wijngaarden, M. Kremers, and C. Van Haesendonck: Physical Review Letters **79** (1997) 3724.

[63] B. Baranowski and J. Szymaszek: physica status solidi (b) **20** (1967) K37.

[64] J. N. Daou and P. Vajda: Physical Review B **45** (1992) 10907.

[65] R. Eder, H. Pen, and G. Sawatzky: Physical Review B - Condensed Matter and Materials Physics **56** (1997) 10115.

[66] T. Shinohara, T. Sato, and T. Taniyama: Phys. Rev. Lett. **91** (2003) 1.

[67] M. Traum and N. Smith: Physical Review B **9** (1974) 1353.

[68] H. Okuyama, W. Siga, N. Takagi, M. Nishijima, and T. Aruga: Surface Science **401** (1998) 344.

[69] J. E. Worsham, M. K. Wilkinson, and C. G. Shull: Journal of Physics and Chemistry of Solids **3** (1957) 303.

[70] G. Nelin: Physica Status Solidi (B) **45** (1971) 527.

[71] H. Frieske and E. Wicke: Berichte der Bunsengesellschaft für physikalische Chemie **77** (1973) 48.

[72] H. Kimizuka, S. Ogata, and M. Shiga: Physical Review B **100** (2019) 024104.

[73] M. Yamauchi, R. Ikeda, H. Kitagawa, and M. Takata: The Journal of Physical Chemistry C **112** (2008) 3294.

[74] J. Völkl, G. Wollenweber, K.-H. Klatt, and G. Alefeld: Zeitschrift für Naturforschung A **26** (1971) 922.

[75] R. Arons, H. Bohn, and H. Lütgemier: Solid State Communications **14** (1974) 1203.

[76] C. Elsässer, M. Fähnle, K. M. Ho, and C. T. Chan: Physica B: Physics of Condensed Matter **172** (1991) 217.

[77] H. Kimizuka, S. Ogata, and M. Shiga: Physical Review B **97** (2018) 014102.

[78] G. R. Stewart: Review of Scientific Instruments **54** (1983) 1.

[79] T. B. Flanagan and F. A. Lewis: Transactions of the Faraday Society **55** (1959) 1400.

[80] Y. Sakamoto, K. Takai, I. Takashima, and M. Imada: Journal of Physics: Condensed Matter **8** (1996) 3399.

[81] R. Fletcher, N. S. Ho, and F. D. Manchester: Journal of Physics C: Solid State Physics **3** (1970) S59.

[82] T. B. Flanagan and W. A. Oates: Annual Review of Materials Science **21** (1991) 269.

[83] P. Mitacek and J. G. Aston: Journal of the American Chemical Society **85** (1963) 137.

[84] S. Zepeda and F. D. Manchester: Journal of Low Temperature Physics **4** (1971) 127.

[85] N. S. Ho and F. D. Manchester: The Journal of Chemical Physics **51** (1969) 5437.

[86] I. S. Anderson, D. K. Ross, and C. J. Carlile: Journal of Physics C: Solid State Physics **11** (1978) L381.

[87] D. Ross, M. McKergow, D. Witchell, and J. Kjems: Journal of the Less Common Metals **172-174** (1991) 169.

[88] H. Akiba, H. Kobayashi, H. Kitagawa, M. Kofu, and O. Yamamuro: Physical Review B **92** (2015) 064202.

[89] J. K. Jacobs and F. D. Manchester: Journal of Physics F: Metal Physics **7** (1977) 23.

[90] P. Vajda, J. P. Burger, J. N. Daou, and A. Lucasson: Physical Review B **33** (1986) 2286.

[91] K. Yamakawa: Journal of Physics Condensed Matter **11** (1999) 8681.

[92] D. S. Maclachlan, R. Mailfert, and J. P. Burger: **17** (1975) 281.

[93] D. S. McLachlan, T. B. Doyle, and J. P. Burger: Journal of Low Temperature Physics **26** (1977) 589.

[94] R. J. Miller and C. B. Satterthwaite: Phys. Rev. Lett. **34** (1975) 144.

[95] H. M. Syed, T. J. Gould, C. J. Webb, and E. M. Gray: arXiv:1608.01774 (2016) 1.

[96] P. A. Redhead: Vacuum **12** (1962) 203.

[97] A. M. de Jong and J. W. Niemantsverdriet: Surface Science **233** (1990) 355.

[98] 杉本敏樹: 博士論文 東京大学大学院 (2010).

[99] Y. Hirohata, S. Fujimoto, T. Hino, and T. Yamashita: Journal of Vacuum Science & Technology A: Vacuum, Surfaces, and Films **11** (1993) 2637.

[100] G. Carter, P. Bailey, D. G. Armour, and R. Collins: Vacuum **32** (1982) 233.

[101] M. Wilde and K. Fukutani: Surface Science Reports **69** (2014) 196.

[102] F. Ajzenberg-Selove. Energy levels of light nuclei A = 11-12, 1990.

[103] G. Amsel and B. Maurel: Nuclear Instruments and Methods In Physics Research **218** (1983) 183.

[104] Y. Fukai and N. Ōkuma: Physical Review Letters **73** (1994) 1640.

[105] Y. Fukai, Y. Ishii, Y. Goto, and K. Watanabe: Journal of Alloys and Compounds **313** (2000) 121.

[106] M. Krystian, D. Setman, B. Mingler, G. Krexner, and M. J. Zehetbauer: Scripta Materialia **62** (2010) 49.

[107] R. Kajimoto, M. Nakamura, Y. Inamura, F. Mizuno, K. Nakajima, S. Ohira-Kawamura, T. Yokoo, T. Nakatani, R. Maruyama, K. Soyama, K. Shibata, K. Suzuya, S. Sato, K. Aizawa, M. Arai, S. Wakimoto, M. Ishikado, S. I. Shamoto, M. Fujita, H. Hiraka, K. Ohoyama, K. Yamada, and C. H. Lee: Journal of the Physical Society of Japan **80** (2011).

[108] K. Nakajima and R. Kajimoto: Hamon **25** (2015) 39.

[109] Y. Inagaki, S. Wen, Y. Kawasaki, H. Takata, Y. Furukawa, and T. Kawae: Journal of the Physical Society of Japan **87** (2018) 123701.

[110] B. M. Iskakov, K. B. Baigisova, and G. G. Bondarenko: Russian Metallurgy (Metally) **2014** (2014) 246.

[111] M. Kemali, J. E. Totolici, D. K. Ross, and I. Morrison: Physical Review Letters **84** (2000) 1531.

[112] C. Elsässer, K. M. Ho, C. T. Chan, and M. Fähnle: Physical Review B **44** (1991) 10377.

[113] J. J. Rush, J. M. Rowe, and D. Richter: Zeitschrift für Physik B Condensed Matter **55** (1984) 283.

[114] W. Fang, J. O. Richardson, J. Chen, X.-Z. Li, and A. Michaelides: Physical Review Letters **119** (2017) 126001.

[115] PHASE: National Institute of Material Science, See https://azuma.nims.go.jp/software/phase for download. .

[116] J. P. Perdew, K. Burke, and M. Ernzerhof: Physical Review Letters **77** (1996) 3865.

[117] P. E. Blöchl: Physical Review B **50** (1994) 17953.

[118] T. Ozawa, R. Shimizu, S. Ogura, T. Hitosugi, and K. Fukutani: Vacuum and Surface Science **62** (2019) 492.

[119] T. Regelmann and L. Schimmele: Journal of Alloys and Compounds **231** (1995) 208.

[120] A. Zawadowski: Physical Review Letters **45** (1980) 211.

[121] J. von Delft, A. Ludwig, and V. Ambegaokar: Annals of Physics **273** (1999) 175.

[122] S. Shivaprasad, L. Udachan, and M. Angadi: Physics Letters A **78** (1980) 187.

[123] K. Fuchs: Mathematical Proceedings of the Cambridge Philosophical Society **34** (1938) 100.

[124] E. H. Sondheimer: *The mean free path of electrons in metals* (1952), Vol. 1, pp. 1–42.

[125] E. Schmiedl, P. Wissmann, and H. U. Finzel: Zeitschrift fur Naturforschung - Section A Journal of Physical Sciences **63** (2008) 739.

[126] P. Wissmann: Thin Solid Films **6** (1970) 67.

[127] B. Stolecki, A. Borodziuk-Kulpa, and C. Wesołowska: Thin Solid Films **116** (1984) 317.

[128] S. Suga, H. Kasai, and A. Okiji. Kondo Effect on Conductivity in Weakly Localized Regime, 1987.

[129] G. Chen and N. Giordano: Physica B: Physics of Condensed Matter **165-166** (1990) 455.

[130] G. Apostolopoulos and C. Papastaikoudis: Solid State Communications **99** (1996) 277.

[131] A. Crépieux and C. Lacroix: Physica B: Condensed Matter **259-261** (1999) 204.

[132] E. Rutherford: Philosophical Magazine **92** (1911) 379.

[133] L. C. Feldman, M. Hill, and J. W. Mayer: Materials Analysis by Ion Channeling (1982).

[134] J. P. Bugeat, A. C. Chami, and E. Ligeon: Physics Letters A **58** (1976) 127.

[135] H. D. Carstanjen, J. Dünstl, G. Löbl, and R. Sizmann: Physica Status Solidi (a) **45** (1978) 529.

[136] 山口貞衛 and 小沢国夫: Nihon Kessho Gakkaishi **20** (1978) 199.

[137] H. H. Pham and T. Cagin: arXiv:1506.00302 (2015).

[138] E. Ligeon, R. Danielou, J. Fontenille, and R. Eymery: Journal of Applied Physics **59** (1986) 108.